Computational studies of the relation between bond strength and QTAIM properties in molecular actinide compounds

Qian-Rui Huang

A dissertation submitted in partial fulfillment

of the requirements for the degree of

Doctor of Philosophy

of

University College London.

Department of Chemistry

University College London

October 10, 2016

I, Qian-Rui Huang, confirm that the work presented in this thesis is my own. Where information has been derived from other sources, I confirm that this has been indicated in the work.

Abstract

In the development of the reprocessing of spent nuclear fuels, liquid extraction with ligands designed to selectively chelate minor actinides (MAs) in the presence of other cations is required. Extractants based on nitrogen donor ligands of the 2,6-bis(triazinyl)-pyridine (BTP) family can show high separation factors for the MAs from lanthanide fission products such as europium, and are also both radiation and low pH tolerant.

In this PhD thesis, density functional theory (DFT) and the quantum theory of atom-in-molecules (QTAIM) are used to investigate the nature of actinide-nitrogen bonding in order to provide enhanced understanding of the selectivity of BTP and related ligands for the MAs. Several different DFT methods are initially benchmarked by calculating ionisation energies and bond dissociation energies of actinide oxides (for which high-level ab initio data are available in the literature). Subsequently, a series of calculations have been performed on some simple actinide complexes with one or three nitrogen-based ligands. QTAIM metrics are used to describe the relative roles of covalency and ionicity in the An-N bonding, and strong correlation is found between bond strength and partial charge difference of the actinide cations on compound formation.

De Sahb *et al.*[1] have proposed that the chemical properties of BTP and other polyazine-based ligands should reflect the contribution of their component single azine donor groups; to probe this, an investigation of the interaction energies of actinide-bisazines, lanthanide-bisazine and complexes of the azine components has been carried out. Strong correlation between the interaction

energies of M-bisazines and the azine ligand components has been found. The interaction energy of a bisazine constructed from two of the same azine groups is shown to be a better indicator to the binding strength of bisazine ligands than the interaction energy of individual azine groups.

Acknowledgements

First and foremost, I would like to thank my supervisor, Prof. Nik Kaltsoyannis, for encouraging my research and for helping me finish this PhD project. I am extremely grateful for all the advice you gave, and for your patience over the past four years.

I would also like to thank Dr. Andrew Kerridge for being my secondary supervisor. Thank you for all the help and the useful suggestions.

Special thanks to Dr. Hazel Cox and Dr. Martijn Zwijnenburg for serving as my viva examiners. Thank you for the enjoyable conversation during the viva exam, and for all your careful and brilliant comments and suggestions.

I would like to thank everyone who help me greatly in these four years although it would be impossible to name you all here. As a famous chinese writer said, "*Since there are too many people that we feel grateful to, lets thank heaven then.*" Thank you everyone.

I will always be grateful to University College London for the Overseas Research Scholarship and for the computing resources.

Last but not least, I would like to thank my family for their unconditional support in everything that I do.

Contents

List of Figures

List of Tables

Chapter 1

Introduction

1.1 The reprocessing of nuclear waste

Nuclear power plants generate electric power via the heat generated by fission of uranium atoms. Unfortunately this process produces highly radioactive waste; due to the strong radioactive toxicity and very long lifetime of the waste, the processing of spent nuclear fuels (SNFs) has attracted more and more research interest. Generally, SNF consists of uranium, the transuranium elements (Np, Pu, Am, Cm) and other fission products, and the long-term radiotoxicity and thermal energy is governed by the transuranium elements. There are three choices to deal with the SNF: (a) geological disposal, either direct disposal of SNF or disposal of post-reprocessing waste; (b) long-term monitoring after stabilisation for surface or near-surface storage; (c) separating the transuranium elements from the nuclear waste and recycling them as fuel. Several partitioning and transmutation strategies are under consideration for the reprocessing of highly radioactive nuclear waste.[2]

The actinides (U, Pa, Np, Pu, Am and Cm) make up $> 96\%$ of SNF; more than 90% of SNF is uranium, and although there is very little mass of the *minor actinides* (MAs), namely, Am and Cm, they are very radiotoxic even in such small amounts. The other fission products, including lanthanides, make up the remainder of the elements in the spent fuel, and are less radiotoxic. The relative radiotoxicity over time of different components in SNF is shown in

Figure 1.1. The majority of the radiotoxicity of SNF is governed by Pu and the MAs, and their associated decay products; in contrast, the radiotoxicity of other components decreases much quicker than the transuranium actinides. Therefore, it is desirable to separate all these elements from SNF for recycling as fuel or for transmutation to less radiotoxic elements, such that the remaining waste will be much less hazardous.

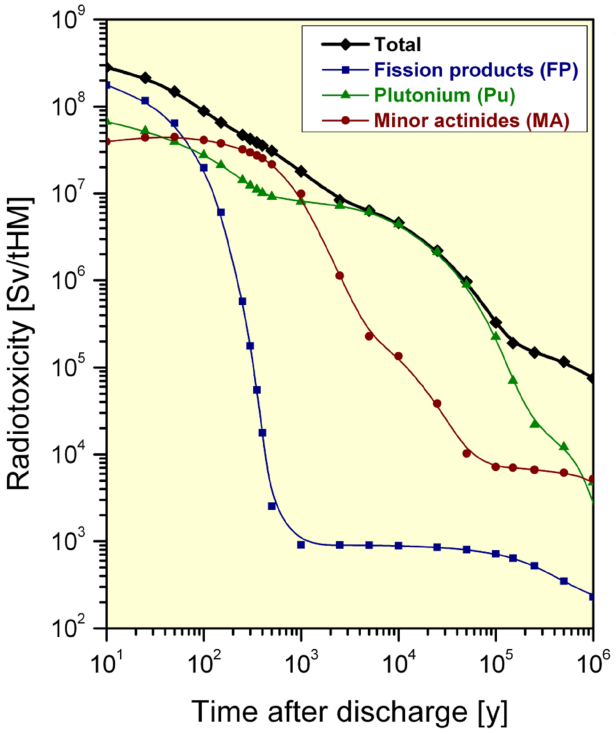

Figure 1.1: Relative radiotoxicity over time of different components in SNF. Reproduced from Andreas Geist's lecture course in the 2014 ThUL school in Actinide Chemistry.

In the first step of the reprocessing of SNF, the PUREX process [3] dissolves SNF in aqueous HNO_3, then removes potentially reuseable U and Pu by solvent extraction. The remaining waste contains MAs, which have long half-lives of several hundred years, and fission products (such as isotopes of Cs, Sr and the lanthanide cations), which have short half-lives (typically less than 100 years). If the MAs could be separated from the post-PUREX nuclear waste, the time for storing the remaining waste could be significantly shortened, and the MAs could also be concentrated to reduce the volume which needs storage

with long term monitoring. Moreover, the MAs could in principle be used in fast-neutron reactors to generate additional power while transmuting to less hazardous elements.

Different techniques for removing MAs from the post-PUREX nuclear wastes have been proposed. One of the possible routes is to employ liquid extraction with ligands designed to selectively chelate MAs in the presence of other cations. Using this method, it is relatively easy to achieve continuous operation and fast mass transfer, and is the only feasible way to remove the MAs from the high-level nuclear waste which already exists around the world. The TRUEX[4] and DIAMEX[5, 6] processes have been proposed to separate MA and fission lanthanides from other fission products. However, actinide and lanthanide cations show similar chemical properties in aqueous solution, which leads to difficult chemical separation. Hence, designing efficient extractants at the molecular level is the most important challenge for the separation of MAs from Ln(III), and many investigations aiming for this target have been carried out.[7, 8, 9, 10, 11, 12, 13, 14, 15, 16, 17, 18] One of the possible routes is the SANEX (Selective ActiNide EXtraction) process,[19] which utilises ligands containing only C, H, O and N atoms to separate MAs from lanthanides, as discussed in Section 1.3 below.

1.2 Similarity and differences between lanthanides and actinides

The major difficulty in the separation of the MAs from lanthanides arises from their chemical similarity; therefore, the key to the design of efficient extractants is the understanding of this chemical behaviour.

The lanthanides exist predominantly in the +3 oxidation state due to their high fourth ionisation energy. The valence orbitals of lanthanides are $6s$, $5d$ and $4f$; when three electrons are removed from the neutral lanthanide atom, the stronger stabilisation of the $4f$ orbital over the $5d$ and $6s$, so that the remaining $4f$ electrons bind even more tightly, leads to the stable +3 oxidation

state for all lanthanides. In contrast, the actinides can form a larger range of oxidation states, especially for the early actinides (Th, Pa, U, Np, Pu), while the later actinides (Cm-Lr) are more like the lanthanides, e.g., dominantly in the +3 state. It is usual to find $5f$ contributions to the bonding of early actinide compounds; for example, uranium usually forms bonds with higher covalency than its lanthanide counterparts.[20] The larger range of oxidation state of the early actinides implies weaker bound valence electrons, indicating that they are more available for chemical bonding. The variation in stable oxidation state across actinides is due to a combination of relativistic effects and the orbital contraction. The relativistic effect makes the $6d$ and $5f$ orbitals larger and more chemically accessible; on the other hand, the orbital contraction makes the $5f$ orbital more core-like in later actinides, so the difficulty of separation from Ln significantly increases for the MAs.

Lanthanides and actinides are hard Lewis acids. Since the $4f$ electrons are core-like and almost unable to overlap with ligand orbitals, lanthanide ions appear like noble gas atoms, except for the +3 nuclear charge, to the ligands. Thus, lanthanide complexes are bonded mainly by electrostatic interactions. On the contrary, the bonding in actinide complexes may have some covalent character since the $5f$ electrons of the actinides are more accessible, especially for the early actinides. This effect is weaker in later actinides, which behave more like the lanthanides to the incoming ligands. In consequence, a major issue in the design of suitable extractant ligands to separate MAs from lanthanides is the extent to which the MAs bond more covalently than their lanthanide analogues, i.e., to what extent does the more covalent bonding in early actinides persist with the MAs?

1.3 The SANEX process and BTP-like ligands

The SANEX (Selective ActiNide EXtraction) process is a post-PUREX process designed to separate the MAs from Ln.[19] After removing the other fission products with the DIAMEX process, only the MAs and lanthanides are ex-

tracted into the aqueous phase; this aqueous phase is then contacted with an organic phase containing the designed SANEX ligand which is capable to separate the MAs from Ln. Currently, some nitrogen-based and sulfur-based ligands show high selectivity for MAs over Ln(III). However, it would be better if the separation process could follow the "CHON" principle; i.e., the reagent used in the process contains only C, H, O and N atoms, so combustion leads to safe gaseous products. Hence, researches on the SANEX process focus on nitrogen-donor MA extractants, which must also tolerate the environment of high radiation and acidity. Many nitrogen-based potential MA extractants have been proposed, but most of them cannot tolerate high acidity and gamma radiation. However, researches have shown 2,6-bis(triazinyl)-pyridines (BTPs) (shown in Figure 1.2(a)) and similar ligands show separation factors for the MAs from europium in excess of 100, and some of them show good resistance to hydrolysis and radiolysis.

The chemistry between the BTP family and trivalent f block cations has therefore been widely studied experimentally. Kolarik et al.[21, 22] find that the BTPs are able to extract Am(III) from Eu(III) in nitric acid solution; the Am(III)/Eu(III) separation factor is typically 100-120; however, the BTPs are unstable to chemical hydrolysis and radiolysis in the environment of nuclear reprocessing. Aiming to avoid the degradation during the extraction process, Hudson et al.[23] replaced the alkyl groups on the triazinyl rings with cyclohexyl rings, and substituted all benzylic positions with methyl groups to avoid chemical attack on that vulnerable position; the resulting compound, 2,6-bis(5,5,8,8-tetramethyl-5,6,7,8-tetrahydro-benzo[1,2,4]triazin-3-yl)pyridine ($CyMe_4$-BTP, shown in Figure 1.2(b)), is resistant to acid hydrolysis. Nevertheless, this molecule binds to Am(III) too tightly, which leads to difficulties in stripping after extraction. To moderate this high extraction efficiency, a second pyridine ring was introduced into these compounds to form 6,6-bis(5,5,8,8-tetramethyl-5,6,7,8-tetrahydro-benzo[1,2,4]triazin-3-yl)[2,2]bipyridine ($CyMe_4$-BTBP, shown in Figure 1.2(c));[24] this molecule

shows both good hydrolytic stability in nitric solution and good resistance to radiolysis,[25] and the stripping is feasible due to moderate binding strength. However, $CyMe_4$-BTBP still suffers from the limited solubility, and the extraction kinetics is still slow for industrial applications. Several years later, Trumm et al. showed that bis-2,6-(5,6,7,8-tetrahydro-5,9,9-trimethyl-5,8-methano-benzo-1,2,4-triazin-3-yl)pyridine (CA-BTP, shown in Figure 1.2(d)) has adequate resistance to hydrolysis and radiolysis, and improved solubility and extraction kinetics;[26] however, CA-BTP precipitates in concentrated nitric acid solution, therefore preventing industrial application in nuclear reprocessing. To improve the extraction thermodynamics and kinetics, a variation of $CyMe_4$-BTBP was proposed by cis-locking the bipyridine bond to a 1,10-phenanthroline structure, which results in $CyMe_4$-BTPhen (shown in Figure 1.2(e)).[27] This molecule shows both higher extracting strength and Am(III)/Eu(III) selectivity, and the extraction kinetics is also better than $CyMe_4$-BTBP. However, the stripping is still inefficient due to the strong binding strength.

The understanding of BTP-like ligands' selectivity on a molecular level is still insufficient to confidently develop reagents or process conditions with higher efficiency. To provide enhanced understanding of the selectivity of BTP and related ligands for the MAs, this thesis investigates the nature of actinide-nitrogen bonding with density functional theory (DFT) and the quantum theory of atom-in-molecules (QTAIM). The QTAIM, which focuses on the properties of the electron density, has only recently been introduced to the $5f$ series, and has been employed to investigate the bonding of actinide compounds such as cyclopentadienyl complexes,[28, 29] binuclear cyclopentadienylthorium complex,[30] uranyl complexes,[31] uranyl-^{Ar}acnac systems (^{Ar}acnac = ArNC(Ph)CHC(Ph)O),[32] thorium and uranium compounds with sulfur and selenium donor ligands,[33, 34] chalcogen-substituted uranyl analogues,[35] small-cavity macrocyclic uranium and thorium complexes,[36] a uranium compound with U-U bond,[37] and thorium oxo and thorium sul-

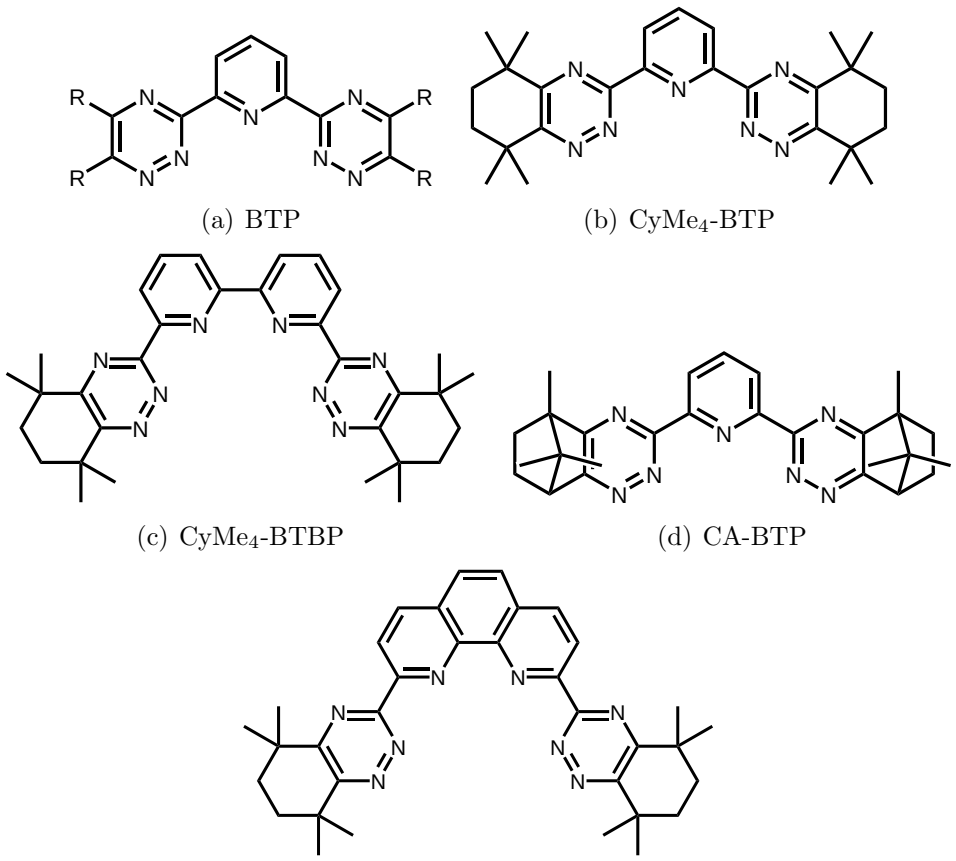

(a) BTP (b) $CyMe_4$-BTP

(c) $CyMe_4$-BTBP (d) CA-BTP

(e) $CyMe_4$-BTPhen

Figure 1.2: Structure of BTP-like ligands.

phide complexes.[38]. QTAIM analysis of caesium uranyl chloride based on experimentally-measured electron density distribution was also carried out.[39, 40] This growing body of QTAIM studies in the actinide series demonstrates the power and use of the method in heavy element chemistry.

In this thesis, I benchmark some different computational methods by calculating ionisation energies and bond dissociation energies of actinide oxides. Subsequently, I perform a series of calculations on some simple actinide complexes with one or three nitrogen-based ligands of relevance to the systems shown in Figure 1.2 to analyse the QTAIM properties of these actinide-nitrogen bonds. Based on these analyses, I find a good relation between the partial charges on the actinide atoms and the calculated bond strengths. It is very desireable to be able to calculate An/Ln-N bond strengths, as they are impor-

tant in determining separation selectivity. If there are any QTAIM parameters that correlate with bond strength, there is potentially a simple way to get bond strengths, which can be very difficult to obtain with standard approaches. This part has been published in Dalton Transactions.[41]

Finally, extending the study of De Sahb *et al.* on La-bisazines,[1] I find strong correlation between the interaction energies of M-bisazine compounds and their azine ligand components for An/Ln-bisazine compounds. I also proposed an indicator to estimate the binding strength of bisazine ligands from the contribution of their single-azine components. Furthermore, the relation between the partial charges on the actinide atoms and the calculated bond strengths are still valid for An-bisazine compounds. I also verify the validity of these findings for M-BTP compounds.

The results of my studies are described in Chapter 4 onwards. Before then, Chapters 2 and 3 set out the theoretical background and computational methodology employed in this work.

Chapter 2

Theoretical Background

2.1 Density functional theory

Following the principles of quantum mechanics, many physical and chemical properties of a molecule can be determined from its electronic structure, that is, the state of its electrons. This includes the energies and the electronic wavefunctions associated with them. Several quantum chemistry methods are available to study the electronic structure of chemical systems. Some of them are accurate but computationally expensive, such as multi-configurational methods and coupled cluster theory; some of them are fast but not so accurate, such as semi-empirical methods. Among these approaches, density functional theory (DFT) is a popular and versatile method, which has good accuracy and relatively low computational cost.

DFT is based on using the electron density instead of the wavefunction to describe the system's energy and other electronic properties. Unlike the wavefunction, the electron density is a physical observable, which can be measured experimentally. Besides, the electron density can be described using only three spatial and one spin variables, but the wavefunction needs $4N$ variables for an N-electron system. Although the concept of using electron density as the only parameter to describe the kinetic energy in a molecule is already in the Thomas-Fermi model, [42, 43] the theoretical basis of DFT is based on the two Hohenberg-Kohn theorems,[44] which are described below.

Typically, the Hamiltonian for a chemical system separates into five parts:

$$\widehat{H} = \widehat{T_n} + \widehat{T_e} + \widehat{V_{nn}} + \widehat{V_{ne}} + \widehat{V_{ee}} \tag{2.1}$$

in which $\widehat{T_n}$ and $\widehat{T_e}$ stand for the kinetic energy of nuclei and electrons, respectively; $\widehat{V_{nn}}$ is the nuclear-nuclear interaction, $\widehat{V_{ne}}$ stands for the nuclear-electron interaction, and $\widehat{V_{ee}}$ is the electron-electron interaction. Applying the Born-Oppenheimer approximation, we can decouple the Hamiltonian into the nuclear and the electronic components, and write down the electronic part of the N-electron Hamiltonian as follows:

$$\widehat{H_e} = \widehat{T_e} + \widehat{V_{ne}} + \widehat{V_{ee}} = -\sum_{i}^{N} \frac{1}{2}\nabla_i^2 + \sum_{i}^{N} v(\vec{r_i}) + \sum_{i<j}^{N} \frac{1}{r_{ij}} \tag{2.2}$$

in which i and j index the electrons, and r_{ij} stands for the distance between electrons i and j. $v(\vec{r_i})$ is the external potential term, which is from the external field due to the positively charged nuclei:

$$v(\vec{r_i}) = -\sum_{A}\sum_{i}^{N} \frac{Z_A}{r_{Ai}} \tag{2.3}$$

where A stands for the nuclei and Z_A stands for their nuclear charge. The key variable in DFT, the electron density $\rho(r)$, is given by:

$$\rho(\vec{r}) = N \int d^3\vec{r_2} \cdots \int d^3\vec{r_N} \Psi^*(\vec{r}, \vec{r_2}, \cdots, \vec{r_N})\Psi(\vec{r}, \vec{r_2}, \cdots, \vec{r_N}) \tag{2.4}$$

This relation can be reversed, that is, the wavefunction Ψ can be viewed as a functional of the electron density, $\Psi[\rho]$. *Hohenberg and Kohn's first theorem* proved the ground state electron density $\rho(r)$ determines the potential $v(\vec{r})$ uniquely. Thus the Hamiltonian can be constructed, and so it determines the wavefunction $\Psi[\rho]$, and hence all the properties of the system. Therefore, we can use the electron density $\rho(r)$ as the fundamental variable of the system,

and treat the electronic energy as a functional of the electron density:

$$E[\rho] = T[\rho] + U[\rho] + \int v(\vec{r})\rho(\vec{r})d^3\vec{r} = F[\rho] + \int v(\vec{r})\rho(\vec{r})d^3\vec{r} \tag{2.5}$$

in which $F[\rho]$ is called *Hohenberg-Kohn functional*; T refers to the kinetic energy, and U refers to the electron-electron interaction energy (from the V_{ee} term in Equation 2.1). The existence of a minimum value of the energy functional is provided by *Hohenberg and Kohn's second theorem*, which is the DFT version of the variation principle, and can be solved without the concept of wavefunction.

The two Hohenberg and Kohn theorems provide the dependency of the electronic energy on the electron density, but not the way to obtain this energy. The Kohn-Sham method is proposed to solve this problem. The Kohn-Sham system is a fictitious system of non-interacting particles, which is chosen to have the same density as the real chemical system, but experiencing an effective local potential $v_{eff}(\vec{r})$. The kinetic energy of such a non-interacting system, $T_s[\rho]$, will be different to the physical one, $T[\rho]$; in addition, since there are no electron-electron interactions, only the classical Coulomb repulsion $J[\rho]$ is considered in the non-interacting system, and not the $U[\rho]$ for the physical system. Hence, we can rewrite $F[\rho]$ as:

$$F[\rho] = T_s[\rho] + J[\rho] + (T[\rho] - T_s[\rho] + U[\rho] - J[\rho]) = T_s[\rho] + J[\rho] + E_{XC}[\rho] \tag{2.6}$$

$E_{XC}[\rho]$ is the exchange-correlation functional, which mimics the difference between non-interacting and interacting particles. Thus, the total energy of the chemical system can be written as:

$$E[\rho] = T_s[\rho] + J[\rho] + E_{XC}[\rho] + \int v(\vec{r})\rho(\vec{r})d^3\vec{r} \tag{2.7}$$

The Hamiltonian is then constructed for these non-interacting particles under

an effective external potential, $v_{eff}(\vec{r})$:

$$\widehat{H} = -\sum_{i}^{N} \frac{1}{2}\nabla_i^2 + \sum_{i}^{N} v_{eff}(\vec{r}) \tag{2.8}$$

v_{eff} includes the original $v(\vec{r})$, the classic Coulomb repulsion J and the effect of the exchange-correlation functional E_{XC}:

$$v_{eff}(\vec{r}) = v(\vec{r}) + \frac{\delta J[\rho]}{\delta\rho(\vec{r})} + \frac{\delta E_{XC}[\rho]}{\delta\rho(\vec{r})} = v(\vec{r}) + v_c(\vec{r}) + v_{XC}(\vec{r}) \tag{2.9}$$

Since the fictitious particles are non-interacting, their coordinates decouple, and their wavefunction is a simple product of orbitals; this formulates the Kohn-Sham equations:

$$\widehat{H}^{KS}\psi_i(\vec{r}) = (-\frac{1}{2}\nabla_i^2 + v_{eff}(\vec{r}))\psi_i(\vec{r}) = \epsilon_i\psi_i(\vec{r}) \tag{2.10}$$

The structure of this equation set is very similar to the Hartree-Fock equations, and can also be solved with Roothaan-Hall-type equations.

2.2 Exchange-correlation functionals

The mathematical form of the exact exchange-correlation term, E_{XC} (and corresponding v_{XC}), is still unknown, and thus approximation to this is required. Many different approximated exchange-correlation functionals have been proposed. The first step in these approximations is the "Local Density Approximation" (LDA), which depends only on the value of the electron density at each point in space (but not its gradients). Generally, the exchange-correlational energy under the LDA can be written as:

$$E_{XC}^{LDA}[\rho] = \int \rho(\vec{r})\epsilon_{XC}(\rho)d\vec{r} \tag{2.11}$$

in which ϵ_{XC} is the exact exchange-correlation energy per particle calculated from the homogeneous electron gas. The LDA is still widely used in condensed

matter physics, but it is less useful for atoms and molecules, which are very different from the electron gas. Molecular properties, such as bond lengths and vibrational frequencies, can be somewhat accurately calculated with LDA;[45] however, most energetic properties are poor, especially the calculation of free atoms, which can be corrected by introducing one empirical parameter to represent the free atom energy. [46]

Beyond LDA, the first practical DFT approach used in modern molecular computations is the "Generalised Gradient Approximation" (GGA), in which the exchange-correlation term not only depends on the local electron density, but also on the gradient of the density of that point. Generally, a GGA exchange-correlation term can be written as:

$$E_{XC}^{GGA}[\rho] = \int \rho(\vec{r})\epsilon_{XC}(\rho, \vec{\nabla}\rho)d\vec{r} \tag{2.12}$$

The GGA takes the non-homogeneous character of real systems into consideration, which provides a significant enhancement over LDA, especially for the problem of overbinding energies. One of the most famous and widely used GGA functionals is PBE,[47] which is named after Perdew, Burke and Ernzerhof.

The GGA can be extended to meta-GGA by including the effect of the Kohn-Sham orbital kinetic energy density, τ, and/or the second order derivatives of the electron density, the Laplacian, $\nabla^2\rho$. A general example of the form of the meta-GGA exchange-correlation term can be written as:

$$E_{XC}^{Meta-GGA}[\rho] = \int \rho(\vec{r})\epsilon_{XC}(\rho, \vec{\nabla}\rho, \nabla^2\rho, \tau)d\vec{r} \tag{2.13}$$

A widely-used example of the meta-GGA is TPSS,[48] which is named after Tao, Perdew, Staroverov, and Scuseria. TPSS utilises only the Kohn-Sham orbital kinetic energy density τ, but not the second order derivatives of the electron density. Compared with PBE, TPSS has better atomisation energies for molecules.

The exact exchange energy can be calculated using the Hartree-Fock method. Incorporating a fixed fraction of the exact exchange, E_x^{HF}, we arrive at the "Hybrid functional". The popular hybrid functional B3LYP,[49] incorporates the Becke exchange functional, the LYP correlation functional and 3 parameters for their linear combination(a, b, c):

$$E_{XC}^{B3LYP} = (1-a)E_X^{VWN} + aE_X^{HF} + bE_X^{B88} + (1-c)E_C^{VWN} + cE_C^{BLYP} \quad (2.14)$$

In this thesis, most calculations are performed with another hybrid functional with fewer empirical parameters, TPSSh[48]. TPSSh uses only one parameter for the inclusion of exact exchange:

$$E_{XC}^{TPSSh} = (1-a)E_X^{TPSS} + aE_X^{HF} + E_C^{TPSS} \quad (2.15)$$

in which, Staroverov, Scuseria, Tao and Perdew suggest $a = 0.1$.

2.3 Self-consistent field procedure

As noted above, the Kohn-Sham equations, Equation 2.10, are structurally similar to the Hartree-Fock equations; they can be solved iteratively by Roothaan-Hall equations. We can write the spin orbitals ψ_i as a linear combination of N one-electron basis functions $\{\chi_\nu\}$:

$$\psi_i = \sum_{\nu}^{N} \chi_\nu C_{\nu i} \quad (2.16)$$

and rewrite Equation 2.10:

$$\sum_{\nu}^{N} \widehat{H}^{KS} \chi_\nu C_{\nu i} = \epsilon_i \sum_{\nu}^{N} \chi_\nu C_{\nu i} \quad (2.17)$$

Spanning the equation with another basis function $\{\chi_\mu^*\}$ will yield:

$$\sum_\nu^N \langle\chi_\mu|\widehat{H}^{KS}|\chi_\nu\rangle C_{\nu i} = \epsilon_i \sum_\nu^N \langle\chi_\mu|\chi_\nu\rangle C_{\nu i} = \sum_\nu^N H_{\mu\nu}^{KS} C_{\nu i} = \epsilon_i \sum_\nu^N S_{\mu\nu} C_{\nu i} \quad (2.18)$$

in which $S_{\mu\nu}$ is the overlap integral between basis functions χ_μ and χ_ν. Hence, the Kohn-Sham equation turns into a matrix equation - a generalised eigenvalue equation:

$$\mathbf{H}^{KS}\mathbf{C} = \epsilon\mathbf{S}\mathbf{C} \quad (2.19)$$

However, the Kohn-Sham Hamiltonian matrix $\mathbf{H}^{KS}$ depends on the orbital coefficient vectors $\mathbf{C}$, hence this equation must be solved iteratively by a self-consistent procedure:

1. The density matrix $\mathbf{P}^{old}$ (from previous cycle or the initial guess) is used to generate the Kohn-Sham Hamiltonian matrix $\mathbf{H}^{KS}$.

2. The Kohn-Sham Hamiltonian matrix $\mathbf{H}^{KS}$ is diagonalised to form the orbital coefficient vectors $\mathbf{C}$.

3. The new density matrix is formed with the orbital coefficients of the occupied orbitals: $\mathbf{P}_{\mu\nu}^{new} = \sum_i^{occ.} C_{\mu i}^* C_{\nu i}$.

4. Examine if the new density matrix $\mathbf{P}^{new}$ is close enough to the previous density matrix $\mathbf{P}^{old}$; if so, then this equation is solved; otherwise, generate a density matrix $\mathbf{P}^{next}$ for next cycle.

When the equation is solved, the v_{eff} in $\widehat{H}^{KS}$ is "self-consistent" with the electron density, thus this method is called "Self-Consistent Field" (SCF). To make the SCF converge, the generation of the $\mathbf{P}^{next}$ is the key step; the most intuitive way is to set $\mathbf{P}^{next} = \mathbf{P}^{new}$ directly, but this usually leads to strong oscillation or even divergence. Thus, different SCF algorithms have been proposed to deal with the convergence problem. Some typical SCF algorithms are discussed in following subsections.

2.3.1 Damping

One of the simplest and earliest methods used is "Damping", in which a fraction of the new density matrix is mixed into the previous one:

$$\boldsymbol{P}^{next} = \alpha \boldsymbol{P}^{new} + (1-\alpha)\boldsymbol{P}^{old}, \quad 0 < \alpha \leq 1 \tag{2.20}$$

where α is the damping constant. In comparison with the most intuitive way, damping can reduce oscillation due to the smaller step size. Typically, a fixed small value of α is chosen until convergence is near, then $\alpha = 0$ is used until final convergence is achieved. A disadvantage of the damping method is that it does not preserve the idempotency of the density matrix, $\mathbf{PSP} = 2\mathbf{P}$, hence undamped steps near convergence are necessary. Also, damping slows down the rate of convergence due to small step size, albeit it is still better than no convergence.

2.3.2 Direct Inversion in the Iterative Subspace (DIIS)

Direct Inversion in the Iterative Subspace (DIIS) is an extrapolation techinique proposed by Pulay,[50] widely used in the field of quantum chemistry. In this method, the elements of the chosen matrix in ith-iteration are viewed as a vector, $\mathbf{p}^i$; the DIIS approximated vector, $\mathbf{p}$, is assumed to be a linear combination of m previous guess vectors:

$$\mathbf{p}^f = \sum_i^m c_i \mathbf{p}^i \tag{2.21}$$

Hence, $\mathbf{p}^i$ can be written as the converged vector $\mathbf{p}^f$ plus an error term, $\mathbf{e}^i$. Thus, the DIIS approximate vector $\mathbf{p}$ can be written as:

$$\mathbf{p} = \sum_i^m c_i(\mathbf{p}^f + \mathbf{e}^i) = \mathbf{p}^f \sum_i^m c_i + \sum_i^m c_i \mathbf{e}^i \tag{2.22}$$

In practice, the error vector $\mathbf{e}^i$ is unknown, so we use the residual vector $\Delta\mathbf{p}^i$ instead:

$$\Delta\mathbf{p}^i = \mathbf{p}^i - \mathbf{p}^{i-1} \tag{2.23}$$

If the DIIS approximated vector $\mathbf{p}$ is equal to the converged vector $\mathbf{p}^f$, $\sum_i^m c_i$ has to be 1. Hence, this turns into a minimisation problem of the norm of the residual vector with the constraint $\sum_i^m c_i = 1$:

$$\langle \Delta\mathbf{p} | \Delta\mathbf{p} \rangle = \sum_{ij}^{m} c_i^* c_j B_{ij} \tag{2.24}$$

in which B_{ij} is an element of the overlap matrix:

$$B_{ij} = \langle \Delta\mathbf{p}^i | \Delta\mathbf{p}^j \rangle \tag{2.25}$$

The minimisation is done by a Lagrange undetermined multiplier technique. The Lagrangian $\mathcal{L}$ is constructed as

$$\mathcal{L} = \sum_{ij}^{m} c_i^* c_j B_{ij} - \lambda(1 - \sum_{i}^{m} c_i) \tag{2.26}$$

in which λ is the Lagrange multiplier. Assuming the coefficients $\{c_i\}$ are real, we can minimise $\mathcal{L}$ by differentiating it with respect to the coefficients c_k:

$$\frac{\partial \mathcal{L}}{\partial c_k} = \sum_{i}^{m} c_i B_{ik} + \sum_{j}^{m} c_j B_{kj} - \lambda = 2\sum_{i}^{m} c_i B_{ik} - \lambda = 0 \tag{2.27}$$

This results in m linear equations. Absorbing the factor of 2 into λ, then combining with the constraint $\sum_i^m c_i = 1$, we can solve a matrix equation to determine the coefficients $\{c_i\}$:

$$\begin{bmatrix} B_{11} & B_{12} & \cdots & B_{1m} & -1 \\ B_{21} & B_{22} & \cdots & B_{2m} & -1 \\ \vdots & \vdots & \ddots & \vdots & \vdots \\ B_{m1} & B_{m2} & \cdots & B_{mm} & -1 \\ -1 & -1 & \cdots & -1 & 0 \end{bmatrix} \begin{bmatrix} c_1 \\ c_2 \\ \vdots \\ c_m \\ \lambda \end{bmatrix} = \begin{bmatrix} 0 \\ 0 \\ \vdots \\ 0 \\ -1 \end{bmatrix} \tag{2.28}$$

Since the DIIS method is a multivariate search, it is usually better than most univariate search methods. Therefore, the DIIS method is widely used for

SCF iterations, CI calculations and geometry optimisations due to its excellent efficiency.

2.3.3 Quadratically Convergent SCF (QCSCF)

One of the major difficuties in SCF convergence is the fact that the Fock matrix depends on the MO coefficients. The Quadratically Convergent SCF (QCSCF) method[51] partially solves this problem by taking the effect of first-order variation into consideration.

Let an occupied spinorbital ψ_i change into ψ_i':

$$\psi_i \rightarrow \psi_i' = \psi_i + \sum_a^{vir.} D_{ia}\psi_a \tag{2.29}$$

in which ψ_a stands for the virtual spinorbitals. Thus, a wavefunction after such variation, $|\Psi\rangle$, which is generally a Slater determinant, can be expanded as follows:

$$|\Psi\rangle = D_0|\Psi_0\rangle + \sum_{ia} D_{ia}|\Psi_i^a\rangle + \frac{1}{2!}\sum_{ijab} D_{ia}D_{jb}|\Psi_{ij}^{ab}\rangle + \cdots \tag{2.30}$$

where $|\Psi_0\rangle$ is the ground state wavefunction obtained in the SCF procedures, $|\Psi_i^a\rangle$ is the singly-excited wavefunction with an electron excited from occupied spinorbital ψ_i to virtual spin orbital ψ_a, and D_{ia} is the corresponding excitation coefficient for $|\Psi_i^a\rangle$. The coefficient $D_0 = \langle\Psi_0|\Psi\rangle$ is introduced for normalisation. The energy can be calculated as follows:

$$\begin{aligned}
E =& \frac{\langle\Psi|\widehat{H}|\Psi\rangle}{\langle\Psi|\Psi\rangle} \\
=& \{D_0^*D_0E_0 + \sum_{ia}[D_0^*D_{ia}\langle\Psi_0|\widehat{H}|\Psi_i^a\rangle + D_{ia}^*D_0\langle\Psi_i^a|\widehat{H}|\Psi_0\rangle] \\
&+ \frac{1}{2}\sum_{ijab}[D_0^*D_{ia}D_{jb}\langle\Psi_0|\widehat{H}|\Psi_{ij}^{ab}\rangle + D_{ia}^*D_{jb}^*D_0\langle\Psi_{ij}^{ab}|\widehat{H}|\Psi_0\rangle + 2D_{ia}^*D_{jb}\langle\Psi_i^a|\widehat{H}|\Psi_j^b\rangle] \\
&+ \cdots\}(D_0^*D_0 + \sum_{ia} D_{ia}^*D_{ia})^{-1}
\end{aligned} \tag{2.31}$$

This equation can be written in a matrix form:

$$E = E_0 + \left\{ \begin{bmatrix} \mathbf{D} \\ \mathbf{D^*} \end{bmatrix}^\dagger \begin{bmatrix} D_0\mathbf{F} \\ D_0^*\mathbf{F^*} \end{bmatrix} + \frac{1}{2} \begin{bmatrix} \mathbf{D} \\ \mathbf{D^*} \end{bmatrix}^\dagger \begin{bmatrix} \mathbf{A} & D_0\mathbf{B} \\ D_0^*\mathbf{B^*} & \mathbf{A^*} \end{bmatrix} \begin{bmatrix} \mathbf{D} \\ \mathbf{D^*} \end{bmatrix} \right\} \{D_0^* D_0 + \mathbf{D^\dagger D}\}^{-1} \tag{2.32}$$

in which $\mathbf{D}$ is the vector of excitation coefficients $\{D_{ia}\}$, $\mathbf{F}$ is the occupied-virtual block of the Fock matrix $\langle \Psi_i^a | \widehat{H} | \Psi_0 \rangle$, and matrices $\mathbf{A}$ and $\mathbf{B}$ stand for the integrals:

$$A_{ia,jb} = \langle \Psi_i^a | \widehat{H} - E_0 | \Psi_j^b \rangle = (\epsilon_a - \epsilon_i)\delta_{ab}\delta_{ij} + (aj||ib) \tag{2.33}$$

$$B_{ia,jb} = \langle \Psi_{ij}^{ab} | \widehat{H} | \Psi_0 \rangle = (ab||ij); \tag{2.34}$$

Since $D_0 \approx 1$ when SCF convergence is near, we can simplify this equation by dropping the D_0 dependence in the $D_0\mathbf{B}$ term to make this expression quadratic in D:

$$E = E_0 + (\tilde{\mathbf{D}}^\dagger \tilde{\mathbf{F}} \tilde{\mathbf{D_0}} + \frac{1}{2}\tilde{\mathbf{D}}^\dagger \tilde{\mathbf{H}} \tilde{\mathbf{D}})(\frac{1}{2}\tilde{\mathbf{D_0}}^\dagger \tilde{\mathbf{D_0}} + \frac{1}{2}\tilde{\mathbf{D}}^\dagger \tilde{\mathbf{D}})^{-1} \tag{2.35}$$

in which $\tilde{\mathbf{D_0}} = \begin{bmatrix} \mathbf{D_0} \\ \mathbf{D_0}^* \end{bmatrix}$, $\tilde{\mathbf{D}} = \begin{bmatrix} \mathbf{D} \\ \mathbf{D}^* \end{bmatrix}$, $\tilde{\mathbf{F}} = \begin{bmatrix} \mathbf{F} & 0 \\ 0 & \mathbf{F}^* \end{bmatrix}$ and $\tilde{\mathbf{H}} = \begin{bmatrix} \mathbf{A} & \mathbf{B} \\ \mathbf{B^*} & \mathbf{A^*} \end{bmatrix}$.

If SCF convergence is achieved, the energy should be stationary; minimisation of the energy yields the secular equations:

$$\tilde{\mathbf{D}}^\dagger \tilde{\mathbf{F}} - (E - E_0)\tilde{\mathbf{D_0}}^\dagger = 0 \tag{2.36}$$

$$\tilde{\mathbf{F}}\tilde{\mathbf{D_0}} + \tilde{\mathbf{H}}\tilde{\mathbf{D}} - (E - E_0)\tilde{\mathbf{D}} = 0 \tag{2.37}$$

These equations can be written in a matrix form, which becomes an eigenvalue equation:

$$\begin{bmatrix} E_0\mathbf{I} & \tilde{\mathbf{F}}^\dagger \\ \tilde{\mathbf{F}} & E_0\mathbf{I}+\tilde{\mathbf{H}} \end{bmatrix} \begin{bmatrix} \tilde{\mathbf{D_0}} \\ \tilde{\mathbf{D}} \end{bmatrix} = E \begin{bmatrix} \tilde{\mathbf{D_0}} \\ \tilde{\mathbf{D}} \end{bmatrix} \tag{2.38}$$

The eigenvector should be normalised such that $\frac{1}{2}\tilde{\mathbf{D_0}}^\dagger\tilde{\mathbf{D_0}} + \frac{1}{2}\tilde{\mathbf{D}}^\dagger\tilde{\mathbf{D}} = 1$. Assuming the wavefunction is constrained to be real, this eigenvalue equation can be further simplified:

$$\begin{bmatrix} E_0\mathbf{I} & \mathbf{F}^\dagger \\ \mathbf{F} & E_0\mathbf{I}+\mathbf{A}+\mathbf{B} \end{bmatrix} \begin{bmatrix} \mathbf{D_0} \\ \mathbf{D} \end{bmatrix} = E \begin{bmatrix} \mathbf{D_0} \\ \mathbf{D} \end{bmatrix} \tag{2.39}$$

and the normalised condition becomes $\mathbf{D}_0^2 + \mathbf{D}^\mathrm{T}\mathbf{D} = 1$.

QCSCF needs similar computation resource to simple SCF, but far fewer iterations are needed. Generally, DIIS is faster than QCSCF, but QCSCF is usually helpful in difficult cases or when very tight convergence is needed.

2.4 Wavefunction stability

Even if the wavefunction is converged in SCF, Equation 2.18 ensures only that the energy is stationary by the variation principle - that is, stationary with respect to the first-order variation of orbital coefficients. To determine the energetic stability of a wavefunction, the second-order variation with respect to the orbital coefficients should be tested. In this section, I will discuss the constraint on a wavefunction, and the stability analysis[52, 53, 54] of a wavefunction converged in an SCF calculation. For convenience, here I assume the wavefunction is calculated with Hartree-Fock theory; the concept can be applied to DFT without too much effort.[53]

2.4.1 Constraints in Hartree-Fock theory

In general, a spin orbital ψ_i can be written as a complex function with spatial coordinates and a spin coordinate, and spans a set of N spatial basis functions

$\{\chi_\mu\}$:

$$\phi_i(r,\sigma) = \phi_i^\alpha(r)\alpha(\sigma) + \phi_i^\beta(r)\beta(\sigma) = \sum_\mu^N [C_{\mu i}^\alpha \chi_\mu \alpha(\sigma) + C_{\mu i}^\beta \chi_\mu \beta(\sigma)] \tag{2.40}$$

in which $\alpha(\sigma)$ and $\beta(\sigma)$ are the two spin basis functions; $\phi_i^\alpha(r)$ and $\phi_i^\beta(r)$ are the spatial orbitals, which can be separated into a real part $\mathrm{Re}(\phi_{\mathrm{i}}^{\alpha(\beta)})$ and an imaginary part $i\mathrm{Im}(\phi_{\mathrm{i}}^{\alpha(\beta)})$; $C_{\mu i}^\alpha$ and $C_{\mu i}^\beta$ are the orbital coefficients, which are complex numbers. This is called the "General Hartree-Fock (GHF) wavefunction", which needs $4N$ real numbers to descrbe a spinorbital $\psi_i(r,\sigma)$. It should be noted that these wavefunctions are not eigenfunctions of the $\widehat{S_z}$ or $\widehat{S^2}$ operators since the spin part cannot be separated. This wavefunction can be further constrained to be real, i.e., $\mathrm{Im}(\phi_{\mathrm{i}}^{\alpha(\beta)}) = 0$, to yield the real-GHF approximation.

Applying constraints to GHF wavefunctions in Equation 2.40 leads to approximations to Hartree-Fock theory. The most commonly applied constraint is the Unrestricted Hartree-Fock (UHF) theory, in which the spin part of each spinorbital in the wavefunction is either pure α or pure β:

$$\begin{aligned} \psi_i(r,\alpha) &= \phi_i^\alpha(r)\alpha(\sigma) = \textstyle\sum_\mu^N C_{\mu i}^\alpha \chi_\mu \alpha(\sigma) \\ \psi_i(r,\beta) &= \phi_i^\beta(r)\beta(\sigma) = \textstyle\sum_\mu^N C_{\mu i}^\beta \chi_\mu \beta(\sigma) \end{aligned} \tag{2.41}$$

This yields a UHF wavefunction, which needs $2N$ real numbers for a spinorbital. Note that a UHF wavefunction is an eigenfunction of $\widehat{S_z}$, but not an eigenfunction of $\widehat{S^2}$.

The next constraint, Restricted Hartree-Fock (RHF) theory, focuses on the spatial part of different spinorbitals; assuming that the number of electrons occupied in alpha orbitals and beta orbitals are n_α and n_β (and $n_\alpha > n_\beta$), then the first n_β α orbitals are restricted to have the same spatial part as the first n_β β orbitals; this forms n_β "doubly occupied" orbitals and $(n_\alpha - n_\beta)$ "singly occupied" orbitals. The closed-shell wavefunction is a special case of the RHF

wavefunction, in which $n_\alpha = n_\beta$.

$$\begin{aligned} \psi_i(r,\alpha) &= \phi_i(r)\alpha(\sigma) = \textstyle\sum_\mu^N C_{\mu i}\chi_\mu\alpha(\sigma) \\ \psi_i(r,\beta) &= \phi_i(r)\beta(\sigma) = \textstyle\sum_\mu^N C_{\mu i}\chi_\mu\beta(\sigma) \end{aligned} \tag{2.42}$$

The RHF wavefunction needs $2N$ real numbers for a spinorbital, but fewer spatial orbitals are needed than for the UHF wavefunction. Note that the RHF wavefunctions are eigenfunctions of $\widehat{S_z}$ and $\widehat{S^2}$. A restricted open-shell calculation always has higher energy than the corresponding UHF wavefunction, which has fewer constraints; therefore, only closed-shell RHF wavefunctions will be taken into consideration in stability analysis.

For GHF, UHF and RHF wavefunctions, the orbital coefficients $C_{\mu i}$ can be complex, but can be also constrained to be real; this will yield real-GHF, real-UHF and real-RHF wavefunctions.

2.4.2 Stability analysis of wavefunctions

A wavefunction is considered stable if none of the possible changes in the one electron orbitals leads to a lower energy. Thus, to analyse if a wavefunction is stable or not, we should examine *how the energy changes when virtual orbitals are allowed to mix with occupied orbitals.*

Using the variation scheme in Subsection 2.3.3, the energy can be calculated as Equation 2.31. Due to Brillouin's theorem, the first-order terms vanish, i.e., $\langle\Psi_0|\widehat{H}|\Psi_i^a\rangle = \langle\Psi_i^a|\widehat{H}|\Psi_0\rangle = 0$. Applying intermediate normalisation, $D_0 = 1$, and truncating the expansion to second order, the energy change

can be written as a matrix equation:

$$\begin{aligned}
\Delta E =& \frac{\langle\Psi|\widehat{H} - E_0|\Psi\rangle}{\langle\Psi|\Psi\rangle} \\
=& \frac{1}{2}\sum_{ijab}[D_{ia}D_{jb}\langle\Psi_0|\widehat{H}|\Psi_{ij}^{ab}\rangle + D_{ia}^*D_{jb}^*\langle\Psi_{ij}^{ab}|\widehat{H}|\Psi_0\rangle + 2D_{ia}^*D_{jb}\langle\Psi_i^a|\widehat{H} - E_0|\Psi_j^b\rangle] \\
=& \frac{1}{2}\sum_{ijab}[D_{ia}D_{jb}B_{ia,jb}^* + D_{ia}^*D_{jb}^*B_{ia,jb} + 2D_{ia}^*D_{jb}A_{ia,jb}] \\
=& \frac{1}{2}\begin{bmatrix}\mathbf{D^*} & \mathbf{D}\end{bmatrix}\begin{bmatrix}\mathbf{A} & \mathbf{B} \\ \mathbf{B^*} & \mathbf{A^*}\end{bmatrix}\begin{bmatrix}\mathbf{D} \\ \mathbf{D^*}\end{bmatrix} = \tilde{\mathbf{D}}^\dagger\tilde{\mathbf{H}}\tilde{\mathbf{D}}
\end{aligned} \tag{2.43}$$

in which, the notation of matrices $\mathbf{D}$, $\mathbf{A}$ and $\mathbf{B}$ is same as Subsection 2.3.3. If the matrix $\tilde{\mathbf{H}}$ is *positive-semidefinite*, i.e., *the eigenvalues of* $\tilde{\mathbf{H}}$ *are all non-negative*, then ΔE is always positive, which means the wavefunction is stable.

For real-GHF wavefunctions, the matrices $\mathbf{A}$ and $\mathbf{B}$ are real, thus Equation 2.43 can be written as:

$$\Delta E = \mathrm{Re}(\mathbf{D}^\dagger)(\mathbf{A}+\mathbf{B})\mathrm{Re}(\mathbf{D}) + \mathrm{Im}(\mathbf{D}^\dagger)(\mathbf{A}-\mathbf{B})\mathrm{Im}(\mathbf{D}) \tag{2.44}$$

The wavefunction is stable if $\Delta E > 0$; for *internal instability*, i.e., without releasing the constraint on the wavefunction, the matrix $(\mathbf{A}+\mathbf{B})$ has to be positive semidefinite. If the vector $\mathbf{D}$ has a non-zero imaginary component, i.e., the real-GHF wavefunction becomes complex in the variation, $\mathrm{Im}(\mathbf{D}^\dagger)(\mathbf{A}-\mathbf{B})\mathrm{Im}(\mathbf{D})$ will give a negative value if $(\mathbf{A}-\mathbf{B})$ has a negative eigenvalue, which may make the energy lower. That means, for a stable real-GHF wavefunction, the matrix $(\mathbf{A}-\mathbf{B})$ has to be positive-semidefinite, or it will lead to a *real-to-complex instability*, that is, the wavefunction can be more stable by releasing the constraint to become a complex-GHF wavefunction.

For real-UHF wavefunctions, the variation of wavefunctions has to be spin-conserving to retain the restriction of UHF, or it will become GHF. Hence, the excitation coefficients in $\mathbf{D}$ can be divided into *spin-conserved* excitations ($\alpha \to \alpha$,$\beta \to \beta$), $\mathbf{D'}$, and *spin-unconserved* excitation ($\alpha \to \beta$,$\beta \to \alpha$), $\mathbf{D''}$.

The matrices $\mathbf{A}$ and $\mathbf{B}$ can be divided using the same method, which will be also denoted with $'$ and $''$, respectively. The derivation of UHF stability analysis is very similar to GHF wavefunctions; for spin-conserved variation of a real UHF wavefunction, the change in energy can be written as:

$$\Delta E = \mathrm{Re}(\mathbf{D'}^{\dagger})(\mathbf{A'} + \mathbf{B'})\mathrm{Re}(\mathbf{D'}) + \mathrm{Im}(\mathbf{D'}^{\dagger})(\mathbf{A'} - \mathbf{B'})\mathrm{Im}(\mathbf{D'}) \tag{2.45}$$

Similar to GHF wavefunctions, the matrix $(\mathbf{A'} + \mathbf{B'})$ has to be positive semidefinite for internal instability. If the vector $\mathbf{D'}$ has a non-zero imaginary component, then the real-UHF wavefunction will become complex; in this case, this wavefunction has a real-to-complex instability if the matrix $(\mathbf{A} - \mathbf{B})$ has a negative eigenvalue.

For the spin-unconserved excitations of real-UHF wavefunctions, which yield GHF wavefunctions, the change in energy can be written in a very similar form:

$$\Delta E = \mathrm{Re}(\mathbf{D''}^{\dagger})(\mathbf{A''} + \mathbf{B''})\mathrm{Re}(\mathbf{D''}) + \mathrm{Im}(\mathbf{D''}^{\dagger})(\mathbf{A''} - \mathbf{B''})\mathrm{Im}(\mathbf{D''}) \tag{2.46}$$

in this case, the energy can be lowered by releasing the constraint on UHF to GHF wavefunction if the matrix $(\mathbf{A''} + \mathbf{B''})$ is positive-semidefinite. This called an *external instability*.

The situation of real-RHF wavefunctions is a little different. A restricted open-shell Hartree-Fock (ROHF) wavefunction always has higher energy than its corresponding UHF wavefunction, hence the folllowing discussion will focus on the closed-shell wavefunctions. For a closed-shell RHF wavefunction, an α spinorbital shares an identical spatial part with its corresponding β spinorbital; to keep the variation of a wavefunction in the UHF constraint (but not GHF), the excitations should be spin-conserved, that is, only the excitations in $\mathbf{D'}$ are necessary in this consideration.

The excitations in $\mathbf{D'}$ can be divided into $\alpha \rightarrow \alpha$ excitations, $\mathbf{D}^{\boldsymbol{\alpha\alpha}}$, and the $\beta \rightarrow \beta$ excitations, $\mathbf{D}^{\boldsymbol{\beta\beta}}$. To retain the constraint of a closed-shell RHF

wavefunction, the variation in α and β spinorbitals should be identical, hence it is natural to symmetrise the excitation, and define ${}^{\mathbf{1}}\mathbf{D'} = \frac{1}{\sqrt{2}}(\mathbf{D}^{\boldsymbol{\alpha\alpha}} + \mathbf{D}^{\boldsymbol{\beta\beta}})$ for singlet excitations; for the anti-symmetric part, $\frac{1}{\sqrt{2}}(\mathbf{D}^{\boldsymbol{\alpha\alpha}} - \mathbf{D}^{\boldsymbol{\beta\beta}})$, is then denoted with ${}^{\mathbf{3}}\mathbf{D'}$, which represents the triplet excitation. Similarly, the matrices $\mathbf{A'}$ and $\mathbf{B'}$ can be divided into a singlet component and a triplet component using the same method, which will be also denoted with ${}^{\mathbf{1}}$ and ${}^{\mathbf{3}}$, respectively.

Thus, stability analysis of real-RHF wavefunctions can be formulated with procedures similar to previous GHF and UHF counterparts. Focusing on only the singlet excitations ${}^{\mathbf{1}}\mathbf{D'}$, the change in energy can be written as:

$$\Delta E = \mathrm{Re}({}^{\mathbf{1}}\mathbf{D'}^{\dagger})({}^{\mathbf{1}}\mathbf{A'} + {}^{\mathbf{1}}\mathbf{B'})\mathrm{Re}({}^{\mathbf{1}}\mathbf{D'}) + \mathrm{Im}({}^{\mathbf{1}}\mathbf{D'}^{\dagger})({}^{\mathbf{1}}\mathbf{A'} - {}^{\mathbf{1}}\mathbf{B'})\mathrm{Im}({}^{\mathbf{1}}\mathbf{D'}) \quad (2.47)$$

The matrix $({}^{\mathbf{1}}\mathbf{A'} + {}^{\mathbf{1}}\mathbf{B'})$ has to be positive semidefinite for internal stability of the closed-shell RHF wavefunction, and the matrix $({}^{\mathbf{1}}\mathbf{A'} - {}^{\mathbf{1}}\mathbf{B'})$ has to be positive semidefinite for the real-to-complex stability of this real-RHF wavefunction. For the triplet counterparts, it can be easily derived that the matrix $({}^{\mathbf{3}}\mathbf{A'} + {}^{\mathbf{3}}\mathbf{B'})$ has to be positive semidefinite to retain the RHF constraint; otherwise, a triplet wavefunction would be more stable, which should always be calculated with UHF constraint at least.

SCF calculations on molecules with unusual geometries or open-shell electronic structures sometimes result in unstable wavefunctions, with internal, external and/or real-to-complex instabilities, thus stability analysis should be performed in these cases. Several computation packages, such as Gaussian09[55] and TURBOMOLE,[56] are capable of performing stability analysis, and re-optimise the SCF-converged wavefunction by changing the spinorbitals according to the excitation coefficients when any instability is found. Many low-symmetry and open-shell molecules are investiated in this thesis, and stablity analysis found instabilites in more than 50% of their wavefunctions during the calculations. Thus, stability analysis is one of the default steps in my calculations.

2.5 Geometry optimisation

For a molecule with a specific geometric structure, the total energy can be calculated using the procedures in the previous sections. Therefore, the total energy can be viewed as a multivariable function of the nuclear coordinates; minimisation of the total energy function results in the stationary geometry of this molecule. This procedure is called "Geometry optimisation", which finds the optimal geometry of a molecule. Since structural differences in a molecule usually lead to changes in its energy and other propreties, it is always important to do geometry optimisation before any analysis which needs physical significance.

The geometry of a molecule can be expressed by the position of the atoms. A typical expression is in cartesian coordinates, which easily define the molecule. However, it is usually more efficient to do the optimisation with *internal coordinates*, which are formed from a set of bond lengths, bond angles and dihedral angles, since they reflect the natural connectivity of chemical structures.

In a geometry optimisation procedure, the geometry is stationary only if the gradient vector of the energy function with respect to the position of the atoms, $\nabla E = \{\frac{\partial E}{\partial r_i}\}$, equals the zero vector; in addition, the second derivatives of the energy, the Hessian matrix, H, should be positive-definite, to ensure the system is optimised to a true minimum.

In practice, one of the most popular techniques to solve the optimisation problem is the GDIIS method,[57] which is a modified version of the DIIS method (see Subsection 2.3.2) using $-H^{-1}(\nabla E)$ as the estimated error vector. When the gradient vector, ∇E, is close enough to the zero vector, the geometry optimisation is converged. The eigenvalues of the Hessian matrix for this geometry correspond to square of the vibrational frequencies; if any one of the eigenvalues is negative, which leads to an imaginary frequency, the geometry is recognised as a saddle point, which needs further optimisation to a true minimum.

2.6 Relativistic effects

For particles with velocities comparable to the speed of light c, the expressions for the physics of the particles should be corrected with special relativity. In atomic units, the energy of the $1s$ electron in a hydrogen-like atom is $-\frac{Z^2}{2}$ where Z is the atomic number; from the virial theorem, $E = -T = \frac{1}{2}V$, the corresponding classical velocity of the $1s$ electron is Z. The speed of light in atomic units is approximately 137; in consequence, the velocities of core electrons in heavy elements are comparable to the speed of light, and relativistic effects should be taken into consideration. In this thesis, we focus on many compounds including lanthanides and actinides, which need relativistic corrections.

The Schrödinger equation does not incorporate relativistic effects natively. The equivalent relativistic quantum mechanical problem can be solved using the Dirac equation[58, 59] instead. A detailed discussion of the Dirac equation is very complicated and beyond the scope of this thesis; however, we note some important points here.

1. The wavefunction described by the Dirac equation is a four-component spinor rather than a scalar function. Two of the degrees of freedom are accounted for by spin, and the others are two different particles, electron and positron.

2. The Dirac equation has twice as many solutions for the wavefunction as the corresponding Schrödinger equation. Half of those solutions correspond to states with negative energies via coupling with positronic eigenstates.

3. The electron spin couples with the magnetic field generated by the movement of the electron. This is called the *spin-orbit coupling* (SOC) interaction, which emerges naturally in the Dirac equation.

The Dirac equation is usually very complicated to solve due to the four components in the wavefunction. Therefore, some approximate Hamiltonians

based on the Dirac equation have been proposed to remedy this problem. One of them is the Zeroth-Order Relativistic Approximation (ZORA).[60, 61, 62, 63] In the special theory of relativity, the total energy W of a particle moving in a potential V is written as:

$$W = \sqrt{m_0^2c^4 + p^2c^2} + V \tag{2.48}$$

where m_0 is the rest-mass of the particle, p is the momentum and c is the speed of light. It is convenient to define the energy of the particle as:

$$\begin{aligned} E = W - m_0c^2 =& \frac{p^2c^2}{m_0c^2 + \sqrt{m_0^2c^4 + p^2c^2}} + V \\ =& \frac{p^2c^2}{2m_0c^2 + E - V} + V \\ =& \frac{p^2c^2}{(2m_0c^2 - V)(1 + \frac{E}{2m_0c^2 - V})} + V \end{aligned} \tag{2.49}$$

Expand the expression in $(-\frac{E}{2m_0c^2-V})$:

$$\begin{aligned} E =& \frac{p^2c^2}{(2m_0c^2 - V)} \frac{1}{1 - (-\frac{E}{2m_0c^2-V})} + V \\ =& \frac{p^2c^2}{(2m_0c^2 - V)} \left[1 + \left(-\frac{E}{2m_0c^2 - V}\right) + \left(-\frac{E}{2m_0c^2 - V}\right)^2 + ...\right] + V \end{aligned} \tag{2.50}$$

This expression is valid only if $E < (2m_0c^2 - V)$, which is almost always correct in chemical applications. Keeping only the zeroth-order term gives the zeroth-order regular approximated (ZORA) energy:

$$E^{\text{zora}} = \frac{p^2c^2}{(2m_0c^2 - V)} + V \tag{2.51}$$

Considering the first-order term, we can obtain a correction to the ZORA

energy, the scaled ZORA energy:

$$E^{\text{scaled}} = \frac{E^{\text{zora}}}{1 + \frac{p^2c^2}{(2m_0c^2 - V)^2}} \tag{2.52}$$

This scaled ZORA energy turns out to be sufficiently accurate in most cases.

Another common approximate relativistic Hamiltonian is the Douglas-Kroll-Hess (DKH) Hamiltonian.[64, 65, 66, 67] Since the eigenstates of a Dirac Hamiltonian can be divided into electronic states and positronic states, it is possible to block-diagonalise the Hamiltonian into these two parts. In this case, the coupling between these two parts is zero, hence the electron part can be viewed as a fully relativistic electron-only Hamiltonian. The DKH method derives a sequence of expressions, which approximate this electron-only Hamiltonian up to arbitrary-order. The ZORA approach and the DKH approach are employed in some of the benchmarking calculations reported in this thesis.

Most chemical behaviour is determined mainly by the valence electrons, hence an alternative to the above approximate methods is to mimic the relativistic effect of the core electrons with an *Effective Core Potential* (ECP). In this context, a specific number of the core electrons are replaced by a potential field. The neglect of the explicit treatment of the core electrons significantly reduces the cost of a relativistic calculations, and often gives quite good results. The major steps to form an ECP are as follows:

1. Generate an all-electron wave function for the atom with a Hartree-Fock, a relativistic Dirac-Hartree-Fock, or a quasi-relativistic Wood-Boring calculation. In this thesis I use Stuttgart small-core ECP[68, 69] for lanthanides and actinides, which is based on quasi-relativistic Wood-Boring calculations of the atoms.

2. Replace the valence orbitals by a set of nodeless pseudo-orbitals, which have no nodes near the core, and are designed to behave correctly in the outer part.

3. Replace the core electrons by an ECP formed by a set of analytical functions (i.e., gaussians) of the nuclear-electron distance. The potential may be different for electrons with different angular momentum.

4. Fit the parameters of the potential to make the behaviour of the pseudo-orbitals match the valence orbitals in the all-electron wavefunction.

2.7 Basis sets

The concept of basis function is introduced when the eigenvalue problem of the Hamiltonian $\widehat{H}$ turns into a matrix equation. In such a context, the molecular orbitals can be written as linear combinations of the basis functions. This is not an approximation if the basis functions are complete; however, a complete basis set means that an infinite number of basis functions are required, which is always impossible in practical computation. In consequence, a necessary approximation is made by the introduction of a finite basis set, and the molecular orbitals are represented with such a basis set; as the basis set is smaller than an infinite set, this representation is poorer. Note that the choice of a basis set does not need to be orthonormal.

The choice of basis function affects the accuracy. If a single basis function is similar to the unknown molecular orbital, we can represent the molecular orbital with fewer basis functions for a given accuracy, thus reducing the size of the computation. Hence, the choice of the basis set is important to balance good accuracy with making the basis set as small as possible. For the calculation of molecules, a good choice of basis set are the atomic orbitals, which reflects the nature of each atom. There are two basic representations for atomic orbitals: *Slater type orbitals* (STO) and *Gaussian type orbitals* (GTO). The major difference between these two types of orbitals is the radial behaviour; the angular parts of both types of orbitals are the spherical harmonics. For STOs, the form of the radial behaviour is based on the electron distribution of a hydrogen atom since it is the only case for which an exact solution can be

obtained with the Schrödinger equation. The functional form of an STO is:

$$\chi_{\zeta,n,l,m}(r,\theta,\phi) = NY_{l,m}(\theta,\phi)r^{n-1}\mathrm{e}^{-\zeta r} \tag{2.53}$$

where ζ is the *Slater orbital exponent* which determines the steepness of the orbital, n is the principal quantum number, l is the angular momentum quantum number, m is the magnetic quantum number, (r,θ,ϕ) are the polar coordinates, N is the normalisation constant and $Y_{l,m}(\theta,\phi)$ are the spherical harmonics. STOs do not have any radial nodes, which can be mimicked by making linear combinations of them. The exponential dependence of r is similar to the behaviour in physical systems, and hence ensures a rapid convergence on increasing the number of STOs. Computationally, however, the exponential produces a cusp near the atomic nucleus, which leads to problems in integration; hence, integrals involving STOs almost always have to be evaluated numerically.

The functional form of a GTO can be written in polar or Cartesian coordinates:

$$\chi_{\zeta,n,l,m}(r,\theta,\phi) = NY_{l,m}(\theta,\phi)r^{2n-2-l}\mathrm{e}^{-\zeta r^2} \tag{2.54}$$

$$\chi_{\zeta,l_x,l_y,l_z}(x,y,z) = Nx^{l_x}y^{l_y}z^{l_z}\mathrm{e}^{-\zeta r^2} \tag{2.55}$$

The sum of l_x, l_y and l_z determines the type of orbital. Note that a d-type GTO in polar coordinates has 5 components, but the corresponding GTOs in Cartesian coordinates have 6 components, which may be transformed to 5 d-type GTOs and 1 s-type GTO; likewise, an f-type GTO in polar coordinates has 7 components, but the corresponding GTOs in Cartesian coordinates have 10 components, which may be transformed to 7 f-type GTOs and a set of 3 p-type GTOs. In practical computations, many programs evaluate the two-electron integrals in Cartesian coordinates, then generate pure spherical d- and $f-$functions by transforming the Cartesian components to the spherical functions. The r^2 dependence in the exponential allows easy analytical

integrations involving GTOs, but also leads to some problems. At the nucleus, a GTO has a zero slope, which is very different to the cusp in real atoms. Meanwhile, GTOs decrease too rapidly in the outer part compared with the wavefunctions of physical systems; this problem can be solved using a linear combinations of several GTOs to represent a single atomic orbital. Computationally, the increase in the number of GTO basis functions is compensated by the reduced resources required for the analytical calculation of the integrals; therefore, most applications utilitze GTOs as the basis set type in electronic structure calculations.

Computation time increases with the number of basis functions used. However, most chemical propreties depend on the valence electrons, and the core orbitals change very little in different chemical bonding situations. Hence, a lot of the computational resource is wasted on describing the chemically uninteresting core electrons. The concept of *Contracted basis sets* is proposed to remedy this situation. Since the core orbitals change very little, it is reasonable to approximate the trial wavefunction by making the linear combination of the inner basis functions constant, i.e., their ratio is no longer determined by the variational principle. The contraction of a basis set always increases the energy since it restricts the form of the trial wavefunctions, but it reduces the computational cost significantly.

The full set of basis functions is called the *primitive GTOs* (PGTOs), and the *Contracted GTOs* (CGTOs) are formed by fixing the linear combinations:

$$\chi^{CGTO} = \sum_{i}^{k} a_i \chi^{PGTO} \tag{2.56}$$

The notation, for example, (14s13p10d8f6g)→[10s9p5d4f3g] is use to describe the contraction in terms of primitive and contracted functions. Note that this notation does not indicate how the contraction is done, it only indicates the size of final basis after the contraction. There are two typical ways of contraction: *segmented contraction* and *general contraction*. In a segemented contraction,

the PGTOs are used only in specific CGTOs, for example:

$$\chi_1^{CGTO} = \sum_{i=1}^{6} a_i \chi_i^{PGTO} \tag{2.57}$$

$$\chi_2^{CGTO} = \sum_{i=7}^{9} a_i \chi_i^{PGTO} \tag{2.58}$$

$$\chi_3^{CGTO} = \chi_{10}^{PGTO} \tag{2.59}$$

In contrast, the general contraction allows the linear combination of all primitive functions in all contracted functions:

$$\chi_1^{CGTO} = \sum_{i=1}^{10} a_i \chi_i^{PGTO} \tag{2.60}$$

$$\chi_2^{CGTO} = \sum_{i=1}^{10} b_i \chi_i^{PGTO} \tag{2.61}$$

$$\chi_3^{CGTO} = \sum_{i=1}^{10} c_i \chi_i^{PGTO} \tag{2.62}$$

In this thesis, the lanthanide and actinide atoms are represented by the Stuttgart relativistic small-core ECP and associated segmented contracted basis sets with *s*-, *p*-, *d*-, *f*- and *g*-type functions.[68, 69]

After the decision on whether to use STOs or GTOs, the next problem is the number of basis functions to be used. The choice with the smallest feasible number is the *minimal basis set*, to use only the core and valence shell orbitals, and only one function for each orbital. A direct improvement of the basis set is to use more functions for each orbital; for example, a *Double Zeta* (DZ) type basis uses 2 basis functions with different ζ exponents for a single orbital. A DZ type basis allows a better description of different types of bonding in different directions since the two coefficients of different ζ exponents can be used to describe different bonds. However, since the core electrons are of little impact on the bonding nature, a doubling of core orbitals is often unnecessary. Hence, the *split-valence basis* which changes only the number of functions for the valence orbitals; for example, the *Valence Double Zeta*

(VDZ) uses 2 functions for each valence orbital. In addition, since covalent bonding is usually directional, *polarisation functions* represent the polarisation of the electron distribution of the atomic orbital by introducing another basis function with higher angular momentum; for instance, an *s*-orbital can be polarised with a *p*-orbital. The inclusion of a set of polarisation functions to a DZ-type basis result in a *Double Zeta plus Polarisation* (DZP) type basis. In this thesis, the *correlation consistent polarised Valence Triple Zeta* (cc-p**VTZ**) basis set[70, 71, 72] is used to represent most of the elements except for the lanthanides and actinides.

2.8 The Quantum Theory of Atoms in Molecules

The Quantum Theory of Atoms In Molecules (QTAIM),[73] which was developed by Prof. Richard F. W. Bader and co-workers, is a model of chemical systems based on topological analysis of electron density, which is a physical observable. The atoms and the bonds are re-defined using the natural expressions from the electron density, which can be obtained from either an electronic structure calculation or experimental measurement. This method has been widely used to investigate atomic and bonding properties, and other interatomic and intermolecular interactions.

2.8.1 Critical points

In the QTAIM, most properties are derived from the electron density $\rho(\boldsymbol{r})$. The Critical Points (CP), where the gradient of the electron density is a zero vector, can be divided into four types according to the second derivatives:

1. *Nuclear Critical Points* (NCPs): all second derivatives with respect to three directions are negative. It is a local maximum of the electron density, which indicates the position of a nucleus.

2. *Bond Critical Points* (BCPs): two second derivatives with respect to two directions are negative, and the remaining one is positive. This is a maximum in a plane, and a minimum in the direction perpendicular to

the plane. Two atoms are considered to be bonded if and only if there is a BCP between their NCPs.

3. *Ring Critical Points* (RCPs): two second derivatives with respect to two directions are positive, and the remaining one is negative. This is a minimum in a plane, and a maximum in the direction perpendicular to the plane. An RCP indicates the existence of a ring structure formed by other bonds, and is therefore surrounded by other BCPs.

4. *Cage Critical Points* (CCPs): all three second derivatives are positive, indicating that the point is a local minimum, and is surrounded by other RCPs.

The number of critical points for an isolated finite molecule follows the Poincaré-Hopf theorem[73]:

$$n_{NCP} - n_{BCP} + n_{RCP} - n_{CCP} = 1 \tag{2.63}$$

where n denotes the number of the subscripted type of CP. Violation of the relationship indicates missing critical points, and a further search should be carried out; however, satisfaction of the relationship does not ensure the completeness of the search.

2.8.2 Atom basin and bond path

After the search for the critical points, it is always possible to partition the molecular space into separate mononuclear regions, Ω, which represent the atom basins in QTAIM. The surfaces bounding the atom basins have zero flux in the gradient field of electron density, that is, they are not crossed by any gradient vectors of electron density $\nabla\rho(\boldsymbol{r})$ at any point, thus satisfying the following constraint:

$$\nabla\rho(\boldsymbol{r}) \cdot \boldsymbol{n}(\boldsymbol{r}) = 0 \tag{2.64}$$

where $\boldsymbol{n}(\boldsymbol{r})$ is the unit normal vector of the surfaces. In this context, the atom basin is bounded by at least one of these interatomic surfaces, which

may terminate at infinity. The atom in QTAIM is thus redefined as the union of a nucleus and its associated atom basin. Note that the local maximum may occur at a position without a nucleus, which is called a non-nuclear attractor (NNA), and will also form an atom basin. In quantum mechanics, the molecular properties can be viewed as the expectation value of an operator averaged over all space; this can be divided into the atomic contributions naturally by calculating the corresponding expectation value of the operator over the atom basin.

A BCP is always located on an interatomic surface between two bonded atoms, and the line of locally maximum electron density, which connects the BCP to the neighboring NCPs, is called a "bond path". The BCP has one positive second derivative in this direction, thus it is the local minimum along the bond path. Besides, the bond path always intersects the zero flux interatomic surface at the location of the corresponding BCP.

2.8.3 Bond properties and atomic properties

The electron densities, energy densities and related properties at the BCP reflect the chemical bonding nature, and thus these properties can be used for the characterization of a chemical bond. Here we list some typical bond properties from the topological properties of BCPs:[74]

- The strength of a chemical bond is reflected in the electron density at the BCP, ρ_{BCP}, which is usually greater than 0.20 a.u. in a covalent bond, and less than 0.10 a.u. in a closed-shell interaction (e.g., ionic bonding or van der Waals interaction.)

- The Laplacian at the BCP, $\nabla^2\rho_{BCP}$ is the sum of the three second derivatives of the electron density at the BCP. By the definition of the BCP, two of the second derivatives correspond to the directions perpendicular to the bond path, denoted λ_1 and λ_2, and are negative; these two second derivatives reflect the extent of the concentration of the electron density along the bond path. The second derivative for the third direction (λ_3),

i.e., along the bond path, is positive; this reflects the depletion of the electron density in the region near the interatomic surface. For a covalent bond, the amplitude of the two negative second derivatives are dominant, and $\nabla^2\rho_{BCP}$ is usually negative; for a closed-shell interaction, the positive second derivative is dominant, leading to a positive $\nabla^2\rho_{BCP}$. In strongly polar bonding, these second derivatives are comparable, hence the Laplacian in this case can have either sign.

- The energy densities (potential, kinetic, and total) are used to investigate the mechanics of a bonding interaction. The potential energy density $V(\boldsymbol{r})$ is the average effective potential field experienced by a single electron at a specific point $\boldsymbol{r}$. This is always negative, and integration over all space yields the overall potential energy of the molecule. On the other hand, the gradient kinetic energy density, $G(\boldsymbol{r})$, is always positive. The evaluation of total energy densities, $H(\boldsymbol{r}) = G(\boldsymbol{r}) + V(\boldsymbol{r})$, was proposed by Cremer and Kraka[75] for the comparison of these two energies. The integration of the total energy density over all space yields the total electronic energy. The total energy of the BCP, H_{BCP}, is negative for a typical covalent bond, which indicates the extent of the sharing of the electrons.

Besides the properties of the BCPs, the "delocalisation index" is defined as the magnitude of the exchange of electrons between two atom basins, which corresponds to the concept of bond order - the number of electron pairs shared between two bonded atoms. The delocalisation index between two atoms A and B, $\delta(A, B)$, is defined as:

$$\delta(A, B) = 2\sum_{\sigma} |F^{\sigma}(A, B)| \tag{2.65}$$

in which the Fermi correlation $F^{\sigma}(A, B)$ is defined as:

$$F^{\sigma}(A, B) = -\sum_{ij} S_{ij}(A)S_{ji}(B) \tag{2.66}$$

where σ is the spin, $S_{ij}(\Omega) = S_{ji}(\Omega)$ is the overlap integral of the two spinorbitals i and j over the basin Ω. Note that this definition is also valid for two non-bonded atoms.

The average of a property O over an atomic basin Ω is calculated as the expectation value of the operater $\hat{O}$ over the basin Ω, thus the definition of atomic kinetic energy, atomic potential energy and total atomic energy is straight-forward as the integration of $G(r)$, $V(r)$ and $H(r)$. The atomic electron population, $N(\Omega)$, is defined as the integration of the electron density over the basin Ω, thus the atomic charge in an atom basin Ω, $q(\Omega)$, is the sum of the nuclear charge Z_Ω and the negative charge contributed by the atomic electron population:

$$q(\Omega) = Z_\Omega - N(\Omega) \tag{2.67}$$

2.9 Atomic charge analysis schemes

Chemical properties are determined by the charge distribution within molecules, which can be calculated by population analysis. Once we obtain the electron density $\rho(\mathbf{r})$, the total number of the electrons can be written as the integration of the electron density, e.g., $N = \int \rho(\mathbf{r})dr$. Therefore, the atomic charge can be determined if the total molecular volume can be divided into regions, Ω_A, which each contain a single nucleus A with nuclear charge Z_A:

$$q(\Omega) = Z_A - \int_{\Omega_A} \rho(\mathbf{r})dr \tag{2.68}$$

The way to divide the space into atom basins is always chosen artificially; a different choice yields a different atom charge analysis scheme. In this thesis, four population analysis schemes are used to investigate the charge distribution of the compounds. The QTAIM charge analysis was already introduced in Subsection 2.8.3, and here we discuss the other three schemes.

2.9.1 Mulliken population analysis

Mulliken population analysis is straight-forward using the density matrix from an SCF calculation. In terms of the density matrix $\mathbf{P}$ spanned by the atomic orbitals $\{\chi_\mu\}$, the electron density can be written as:

$$\begin{aligned}\rho(\boldsymbol{r}) &= \sum_a^N \psi_a^*(\boldsymbol{r})\psi_a(\boldsymbol{r}) \\ &= \sum_a^N \sum_\nu C_{\nu a}^* \chi_\nu^*(\boldsymbol{r}) \sum_\mu C_{\mu a}\chi_\mu(\boldsymbol{r}) \\ &= \sum_\mu \sum_\nu \left[\sum_a^N C_{\mu a} C_{\nu a}^*\right] \chi_\nu^*(\boldsymbol{r})\chi_\mu(\boldsymbol{r}) \\ &= \sum_\mu \sum_\nu \mathbf{P}_{\mu\nu}\mathbf{S}_{\nu\mu} = \sum_\mu (\mathbf{PS})_{\mu\mu} = \mathrm{tr}(\mathbf{PS})\end{aligned} \tag{2.69}$$

in which N is the total number of electrons, and ψ_a are the occupied molecular orbitals. Thus, it is natural to interpret $(\mathbf{PS})_{\mu\mu}$ as the number of electrons to be associated with χ_μ, which implies that the charge is partitioned evenly between two atomic orbitals. This is called *Mulliken Population Analysis* (MPA). Since the atomic orbitals correspond to specific nuclei, the number of electrons associated with a given atom can be easily calculated by summing over all the atomic orbitals centered on that atom, and the partial atomic charge for an atom A can be written as:

$$q_A = Z_A - \sum_{\mu\in A}(\mathbf{PS}) \tag{2.70}$$

MPA is conceptually simple, but it often results in some problems. The lack of consideration of electronegativities of different atoms leads to unfeasible equal partitioning even in a strongly polar bond. Moreover, the equal partitioning between basis functions will yield very strange results if one atom uses bigger basis set than another, thus a balanced basis set is required. Nevertheless, MPA is still useful in comparing trends of charge differences among systems using similar basis functions.

2.9.2 Hirshfeld population analysis

Hirshfeld charges use the electron densities of free atoms for partitioning the molecular electron density. For each point $\mathbf{r}$ in space, the *promolecular density* is defined as the sum of electron densities of free atoms:

$$\rho^{pro}(\mathbf{r}) = \sum_A \rho_A^{at}(\mathbf{r}) \tag{2.71}$$

where $\rho_A^{at}(\mathbf{r})$ is the electron density of a spherically-averaged ground-state free atom A. Thus, the weighting factor w_A can be defined as the contribution to the promolecular density from the free atom A:

$$w_A(\mathbf{r}) = \frac{\rho_A^{at}(\mathbf{r})}{\rho^{pro}(\mathbf{r})} \tag{2.72}$$

In the *Hirshfeld Population Analysis* (HPA) scheme, the atomic contribution to the actual molecular electron density $\rho^{actual}(\mathbf{r})$ at each point in space is mimicked by these weighting factors, hence the partial charge of an atom A is defined as:

$$q_A = Z_A - \int w_A(\mathbf{r})\rho^{actual}(\mathbf{r})dr \tag{2.73}$$

Typically, the electron density of neutral atoms is used in HPA, but other valence configurations may be considered when needed.

2.9.3 Natural population analysis

MPA may sometimes give problematic results due to the non-orthogonality of the atomic basis, and several orthogonalisation methods have been proposed to resolve this problem. The concept of *Natural Atomic Orbitals* (NAOs) is thus proposed to provide a method to obtain an orthonormal basis set, which is also localised to represent the atomic orbitals.

The NAOs are constructed by diagonalisation of the one centre density matrix, followed by removal of interatomic overlap. The procedure is as follows:

- The density matrix $\mathbf{D}$ can be written in terms of blocks of basis functions

corresponding to specific atoms:

$$\mathbf{D} = \begin{bmatrix} \mathbf{D}^{\mathrm{AA}} & \mathbf{D}^{\mathrm{AB}} & \mathbf{D}^{\mathrm{AC}} & \cdots \\ \mathbf{D}^{\mathrm{BA}} & \mathbf{D}^{\mathrm{BB}} & \mathbf{D}^{\mathrm{BC}} & \cdots \\ \mathbf{D}^{\mathrm{CA}} & \mathbf{D}^{\mathrm{CB}} & \mathbf{D}^{\mathrm{CC}} & \cdots \\ \vdots & \vdots & \vdots & \ddots \end{bmatrix} \tag{2.74}$$

Each of the atomic blocks is diagonalised to produce pre-NAOs; these pre-NAOs preserve the necessary radial and angular nodal characteristics, hence they are orthogonal to each other on the same atom, but they are non-orthogonal to pre-NAOs on different atoms.

- The next step in the construction of the NAOs is to remove the overlap between pre-NAOs of different atoms. The pre-NAOs $\{\phi_i\}$ are made orthogonal to generate orthogonal orbitals $\{\phi_i^w\}$ by minimising the occupancy-weighted norm of the variation in orbitals, e.g., $\sum_i \omega_i \|\phi_i^w - \phi_i\|^2$. The weight ω_i is the occupancy of the orbital ϕ_i; hence, orbitals with low occupancy are free to rotate significantly during the orthogonalisation procedure, but orbitals with high occupancy will be strongly preserved. This can be achieved by the following sequence:

  1. Separate the pre-NAOs into the strongly occupied *natural minimal basis* and weakly occupied *Rydberg orbitals*.
  2. The natural minimal basis is made orthogonal by the occupancy-weighted procedure above.
  3. The Rydberg orbitals are orthogonalised with respect to the minimal natural basis on the same atom by a Gram-Schmidt orthogonalisation.
  4. The Rydberg orbitals are also orthogonalised by the occupancy-weighted procedure.

The final set of orthogonal orbitals are the NAOs, and the diagonal elements of the density matrix spanned by the NAOs are the orbital populations. Thus,

Natural Population Analysis (NPA) can be done with a procedure very similar to MPA, and the atomic charge can be obtained as the summation of populations of the NAOs corresponding to the atom and the charge of the nucleus.

Chapter 3

Computational Details

Electronic structure at the DFT level is computed with either the Gaussian09[55] (G09) program or the Amsterdam Density Functional[76, 77, 78] (ADF) 2012 program. In the G09 calculations, relativistic effects are included via one of the two following ways: (1) The Stuttgart relativistic small-core pseudopotentials and associated basis sets (s-, p-, d-, f- and g-type functions, segmented contractions)[68, 69] for the lanthanide atoms and actinide atoms, and Dunning's cc-pVTZ bases for the other atoms. Most calculations in this thesis are performed with this method. (2) Segmented All-electron Relativistically Contracted (SARC) basis sets in conjuction with the Douglas-Kroll-Hess[64, 65, 66, 67] second-order scalar relativistic Hamiltonian (SARC-DKH2)[79]. (3) SARC basis sets with the Douglas-Kroll-Hess fourth-order relativistic Hamiltonian (SARC-DKHSO), which includes the effect of spin-orbit coupling. Due to the lack of analytical derivatives in the DKH hamiltonian in G09, the geometry of these molecules are optimised with the first method, and wavefunction stability checks[52, 53] performed to ensure the molecules are in their ground state. The exchange-correlation functional used in the geometry optimisation and stability check, if not mentioned explicitly, is TPSSh due to its best performance in the benchmarking calculations (see Section 4.1). The "ultrafine" grid was adopted for numerical integration within the DFT framework.

In the ADF calculations, relativistic effects are included by means of the

scalar relativistic zeroth order regular approximation.[60, 61, 62] All electron triple-ζ double polarised (TZ2P) basis sets and the TPSSh exchange-correlation functional are used in all ADF calculations based on the G09 optimised geometries. The integration grid is set to 6.0, and the SCF convergence criteria are set to the ADF defaults.

The bond strength in the actinide compounds is represented by the bond energy. Both the molecule/fragment electronic energy differences and the bond energies including zero point energy (ZPE) corrections are calculated for benchmarking the methods. Zero point energy correction is computed from the vibrational frequencies, and basis set superposition error (BSSE) is calculated with the counterpoise method[80, 81]. However, these two corrections are not included in the remaining calculations of bond energies since the benchmarking in Sec 4.1 shows that the effect of these corrections is negligible, and the accuracy of the calculated energies is not really improved. The solvent effects of water ($\epsilon = 78.3553$) were evaluated using the integral equation formalism of the polarized continuum model (IEF-PCM) [82, 83] utilizing the universal force field (UFF) radii.[84]

Quantum Theory of Atoms In Molecules (QTAIM)[73] analysis is performed in the following two ways: (1) For the electron densities calculated by G09, the QTAIM properties are calculated with the AIMAll[85] package. We use G09 to generate extended wavefunction files for input to the AIMAll package. (2) ADF has limited built-in QTAIM analysis, which is used in this report to calculate the QTAIM properties at the bond critical points.

For bond dissociation energies, bond interaction energies and ionisation energies, the energy unit in this report is always kJ/mol if not explicitly mentioned, and the unit of bond length is always Å. All QTAIM properties are in the corresponding atomic units.

Chapter 4

Actinide Oxides

4.1 Benchmarking the methods for actinide oxides

In order to build up the relationship between bond strength, covalency and QTAIM properties, it is important to obtain a reliable electron density with a feasible method. To compare with previously obtained theoretical and experimental data for actinide atoms, monoxides[86, 87, 88] and dioxides,[86, 87] calculations on the ionisation energies and bonding energies of these systems with different charges have been performed.

I began by optimising the geometries of AnO^{n+} and AnO_2^{n+} (An = Th-Cm; n = 0, 1, 2). Three exchange correlation functionals, B3LYP, TPSS and TPSSh, were used in these calculations. Relativistic effects were included with the ECP mentioned in Chapter 3. The bond lengths of molecules optimised with different functionals are listed in Table 4.1.1. For the AnO_2 molecules, the averaged bond length of the two An-O bonds is shown. The ThO_2 molecule is bent (118.5° for B3LYP, 118.1° for TPSS and 118.6° for TPSSh) in its neutral charge state, and in all the other cases the geometry optimisation leads to a linear structure. As the table shows, the three exchange correlation functionals give results similar to each other and usually to the geometry optimised previously by CASPT2[87].

The bond strength in the actinide oxides is represented by the bond dis-

Molecule	Method	Th	Pa	U	Np	Pu	Am	Cm
AnO	Literature-CASPT2[87]	1.863	1.818	1.838	1.839	1.820	1.801	1.836
	B3LYP	1.832	1.803	1.840	1.834	1.827	1.833	1.840
	TPSS	1.839	1.812	1.838	1.831	1.829	1.844	1.839
	TPSSh	1.831	1.801	1.834	1.827	1.821	1.835	1.832
AnO^+	Literature-CASPT2[87]	1.827	1.804	1.796	1.798	1.789	1.782	1.792
	B3LYP	1.800	1.776	1.800	1.792	1.791	1.781	1.796
	TPSS	1.807	1.800	1.801	1.796	1.789	1.787	1.800
	TPSSh	1.799	1.794	1.797	1.788	1.781	1.777	1.791
AnO^{2+}	Literature-CASPT2[87]	1.790	1.733	1.720	1.723	1.731	1.808	1.791
	B3LYP	1.763	1.738	1.725	1.723	1.722	1.776	1.840
	TPSS	1.768	1.745	1.734	1.735	1.741	1.785	1.794
	TPSSh	1.760	1.735	1.722	1.721	1.723	1.775	1.814
AnO_2	Literature-CASPT2[87]	1.923	1.816	1.827	1.761	1.744	1.807	1.832
	B3LYP	1.896	1.805	1.788	1.818	1.746	1.825	1.836
	TPSS	1.898	1.812	1.810	1.800	1.802	1.833	1.841
	TPSSh	1.891	1.801	1.794	1.806	1.806	1.821	1.831
AnO_2^+	Literature-CASPT2[87]	1.832	1.767	1.745	1.723	1.704	1.721	1.746
	B3LYP	1.867	1.767	1.752	1.719	1.713	1.715	1.747
	TPSS	1.870	1.775	1.762	1.742	1.725	1.731	1.760
	TPSSh	1.860	1.764	1.750	1.728	1.711	1.714	1.745
AnO_2^{2+}	Literature-CASPT2[87]	1.903	1.726	1.710	1.700	1.675	1.679	1.674
	B3LYP	1.849	1.771	1.692	1.675	1.660	1.665	1.687
	TPSS	1.873	1.782	1.706	1.703	1.690	1.683	1.705
	TPSSh	1.886	1.768	1.692	1.688	1.673	1.665	1.686

Table 4.1.1: An-O bond length in the optimised geometries with different exchange correlation functionals. (Unit: Å)

sociation energy, D, which is calculated by the following equations:

$$D[\mathrm{AnO}^{n+}] = E[\mathrm{An}^{n+}] + E[\mathrm{O}] - E[\mathrm{AnO}^{n+}] \tag{4.1}$$

$$D[\mathrm{OAn\text{-}O}^{n+}] = E[\mathrm{AnO}^{n+}] + E[\mathrm{O}] - E[\mathrm{AnO}_2^{n+}] \tag{4.2}$$

$$D[\mathrm{AnO}_2^{n+}] = \frac{E[\mathrm{An}^{n+}] + 2E[\mathrm{O}] - E[\mathrm{AnO}_2^{n+}]}{2} \tag{4.3}$$

where $n+$ is the positive charge of the actinide species. Note that Eq. 4.2 is analogous to the experimental measurement of D while Eq. 4.3 is the average of D which should reflect the average bond strength. Relativistic effects are included with the three G09 methods mentioned in Chapter 3: (1) ECP, (2) SARC-DKH2 and (3) SARC-DKHSO. Moreover, the results with the zero point energy (ZPE) and BSSE corrections are also calculated for comparison.

The energies from this benchmarking process are listed in Appendix B; experimental and theoretical values from the literature are also listed for comparison. The mean absolute errors (MAE), summarised in Table 4.1.2 (ionisation energies) and Table 4.1.3 (bond dissociation energies), are calculated as the average of the difference between the calculated result and the experimental value. It should be noted that the experimental values for the bond dissociation energy of ThO_2^{2+} and CmO_2^{2+} are only rough estimates,[86] hence the seemingly strange calculated result is not unexpected. The MAE in this case is calculated from the data for PaO_2^{2+}, UO_2^{2+}, NpO_2^{2+}, PuO_2^{2+}, and AmO_2^{2+}.

As Table 4.1.2 and Table 4.1.3 show, the calculations with the TPSSh exchange correlation functional, Stuttgart ECP and basis sets usually have the smallest MAE; calculations with B3LYP and TPSS normally give good results, too. The inclusion of ZPE and BSSE correction does not improve the result, and the value of these corrections are negligible, hence these two corrections are not taken into consideration in subsequent calculations. Calculations with the SARC basis sets and the DKH/DKHSO Hamiltonians usually lead to larger MAE since they produce some outlier values, which are very different to other values with several times the standard deviation; e.g., the first ionisation energy

Method	IE1(An)	IE2(An)	IE1(AnO)	IE2(AnO)	IE1(AnO_2)	IE2(AnO_2)
B3LYP	20.4	18.3	23.0	30.8	37.0	88.2
B3LYP+ZPE+BSSE	N/A	N/A	43.9	36.6	36.5	80.0
B3LYP+DKH	25.2	38.0	24.1	31.5	37.5	82.6
B3LYP+DKH+ZPE+BSSE	N/A	N/A	40.3	37.2	35.9	77.6
B3LYP+DKHSO	35.1	42.8	28.9	23.1	36.5	85.5
B3LYP+DKHSO+ZPE+BSSE	N/A	N/A	52.1	22.8	35.0	79.0
TPSS	39.5	20.5	11.7	19.0	43.5	76.5
TPSS+ZPE+BSSE	N/A	N/A	11.7	33.2	40.9	89.7
TPSS+DKH	92.9	95.4	12.1	21.7	156.8	84.8
TPSS+DKH+ZPE+BSSE	N/A	N/A	13.4	31.4	155.6	101.1
TPSS+DKHSO	79.1	83.2	11.7	20.1	147.7	87.8
TPSS+DKHSO+ZPE+BSSE	N/A	N/A	14.4	29.5	146.5	104.2
TPSSh	37.7	23.7	13.1	20.8	40.8	76.7
TPSSh+ZPE+BSSE	N/A	N/A	14.9	28.1	123.3	116.0
TPSSh+DKH	40.6	28.6	13.9	21.8	44.6	83.5
TPSSh+DKH+ZPE+BSSE	N/A	N/A	15.7	24.9	39.8	88.5
TPSSh+DKHSO	40.5	29.6	18.2	24.3	42.6	86.3
TPSSh+DKHSO+ZPE+BSSE	N/A	N/A	20.0	28.1	37.9	90.6

Table 4.1.2: Mean absolute error of ionisation energies from different methods. (Unit: kJ/mol) An=Th-Cm.

Method	D(AnO)	D(AnO^+)	D(AnO^{2+})	D(OAn-O)	D(OAn^+-O)	D(OAn^{2+}-O)
B3LYP	45.6	65.1	97.6	25.1	31.0	59.4
B3LYP+ZPE+BSSE	62.7	66.5	90.3	36.4	24.5	65.1
B3LYP+DKH	38.9	72.5	85.4	23.0	44.3	51.9
B3LYP+DKH+ZPE+BSSE	62.3	72.7	75.2	41.5	33.9	57.2
B3LYP+DKHSO	55.6	73.2	96.0	21.5	40.6	57.1
B3LYP+DKHSO+ZPE+BSSE	79.0	73.7	85.7	40.7	36.0	57.2
TPSS	39.2	48.6	66.9	51.4	89.2	61.1
TPSS+ZPE+BSSE	31.4	42.2	78.4	43.4	82.0	40.4
TPSS+DKH	44.9	112.1	67.0	309.2	369.8	418.7
TPSS+DKH+ZPE+BSSE	34.5	102.6	67.4	313.3	377.0	444.8
TPSS+DKHSO	44.9	102.8	69.7	287.4	343.9	394.8
TPSS+DKHSO+ZPE+BSSE	37.4	93.2	72.0	291.4	351.1	421.0
TPSSh	30.7	50.3	88.7	28.7	57.6	45.3
TPSSh+ZPE+BSSE	29.3	47.5	106.6	25.5	128.0	49.7
TPSSh+DKH	30.9	46.6	74.0	35.0	69.4	59.1
TPSSh+DKH+ZPE+BSSE	28.9	43.8	90.8	28.9	56.3	74.8
TPSSh+DKHSO	33.2	49.8	81.7	34.6	71.8	58.6
TPSSh+DKHSO+ZPE+BSSE	32.3	52.6	99.6	29.8	60.1	74.4

Table 4.1.3: Mean absolute error of bond dissociation energies D from different methods. (Unit: kJ/mol) An=Th-Cm.

of thorium calculated with the TPSS functional and the SARC-DKH2 method is 1039 kJ/mol, which is almost two times the value calculated with other methods. A possible reason for the outlier values is that the wavefunction is not stable; however, the DKH/DKHSO results without considering the outlier values still have larger MAEs than the ones calculated with ECPs.

The three exchange correlation functionals give good results in both geometry optimisation and the evaluation of ionisation energies and bond dissociation energies, and they are comparable to the results from the CASPT2 method,[87] which is much more time-consuming. The TPSSh functional usually gives slighter better values than the other two functionals; in addition, the utilising of ECP mostly gives smaller MAEs than using the DKH/DKHSO Hamiltonian. Moreover, due to the lack of analytical derivatives in DKH relativistic calculations in G09, geometry optimisations could not performed with DKH/DKHSO, meaning that calculating everything with ECPs would make the whole procedure more straight-forward. For all these reasons, I decided to choose the TPSSh exchange correlation functional with the Stuttgart small core ECP for subsequent calculations.

4.2 QTAIM properties of actinide oxides

In order to investigate the possible relationship between bond strength and QTAIM properties, I performed QTAIM analysis of these actinide oxides with different charges based on the wavefunctions generated with G09. Selected QTAIM properties, especially of the Bond Critical Points (BCP), are summarised in Table 4.2.1 and Table 4.2.2. QTAIM properties from the AnO_2 BCP are the average values of two BCPs. The bond dissociation energies D listed in these tables are the values calculated with TPSSh and Stuttgart small-core ECP, described in the previous subsection; D of AnO_2 is calculated from Eq.4.3, the averaged bond dissociation energy of the actinide dioxide.

As the tables show, most of the ρ_{BCP} are larger than 0.2, which indicates that the bonding in actinide oxides has an obvious shared shell interaction. The

	ThO	PaO	UO	NpO	PuO	AmO	CmO
D	904.8	852.2	807.2	745.7	633.6	534.5	716.8
R	1.831	1.801	1.834	1.827	1.821	1.835	1.832
ρ_{BCP}	0.262	0.284	0.259	0.259	0.257	0.242	0.241
$\nabla^2\rho_{BCP}$	0.323	0.298	0.411	0.488	0.504	0.548	0.673
V_{BCP}	-0.536	-0.586	-0.515	-0.520	-0.508	-0.462	-0.484
G_{BCP}	0.308	0.330	0.309	0.321	0.317	0.300	0.326
H_{BCP}	-0.228	-0.256	-0.206	-0.199	-0.191	-0.163	-0.158
δ	2.044	2.157	2.005	2.042	2.061	2.011	2.029
$\left\lvert\Delta Q_{\mathrm{An}}^{\mathrm{QTAIM}}\right\rvert$	1.122	1.052	1.106	1.076	1.049	1.066	1.061
	ThO^+	PaO^+	UO^+	NpO^+	PuO^+	AmO^+	CmO^+
D	883.5	831.0	804.8	708.5	590.9	474.1	617.7
R	1.799	1.794	1.797	1.788	1.781	1.777	1.791
ρ_{BCP}	0.283	0.287	0.284	0.286	0.285	0.283	0.269
$\nabla^2\rho_{BCP}$	0.323	0.321	0.424	0.498	0.512	0.499	0.710
V_{BCP}	-0.607	-0.609	-0.596	-0.605	-0.596	-0.564	-0.567
G_{BCP}	0.344	0.344	0.351	0.365	0.362	0.344	0.372
H_{BCP}	-0.263	-0.264	-0.245	-0.240	-0.234	-0.220	-0.195
δ	2.041	2.031	2.023	2.074	2.097	2.079	2.081
$\left\lvert\Delta Q_{\mathrm{An}}^{\mathrm{QTAIM}}\right\rvert$	1.019	0.988	0.988	0.948	0.905	0.877	0.913
	ThO^{2+}	PaO^{2+}	UO^{2+}	NpO^{2+}	PuO^{2+}	AmO^{2+}	CmO^{2+}
D	879.7	756.2	639.6	491.5	324.3	153.4	295.9
R	1.760	1.735	1.722	1.721	1.723	1.775	1.814
ρ_{BCP}	0.314	0.336	0.346	0.346	0.335	0.282	0.232
$\nabla^2\rho_{BCP}$	0.314	0.272	0.282	0.349	0.443	0.583	0.707
V_{BCP}	-0.709	-0.760	-0.774	-0.765	-0.729	-0.570	-0.467
G_{BCP}	0.394	0.414	0.422	0.426	0.420	0.358	0.322
H_{BCP}	-0.315	-0.346	-0.352	-0.339	-0.309	-0.212	-0.145
δ	2.116	2.228	2.315	2.372	2.417	2.248	1.827
$\left\lvert\Delta Q_{\mathrm{An}}^{\mathrm{QTAIM}}\right\rvert$	0.885	0.794	0.700	0.622	0.537	0.436	0.427

Table 4.2.1: The bond interaction energy D (kJ/mol), bond lengths R (Å), the electron density at the BCP ρ_{BCP} (a.u), the Laplacian at the BCP $\nabla^2\rho_{BCP}$ (a.u), the potential energy density V_{BCP} (a.u), the gradient kinetic energy density $G_{BCP}(a.u)$, the total energy of the BCP H_{BCP} (a.u), the delocalisation index δ (a.u), and the change of the QTAIM partial charge on the actinide atom $\left\lvert\Delta Q_{\mathrm{An}}^{\mathrm{QTAIM}}\right\rvert$ (a.u) of actinide monoxides. The bond interaction energy D is calculated using Equation 4.1.

	ThO_2	PaO_2	UO_2	NpO_2	PuO_2	AmO_2	CmO_2
D	801.7	833.3	766.3	712.3	628.6	518.0	585.1
R	1.891	1.801	1.794	1.806	1.806	1.821	1.831
ρ_{BCP}	0.224	0.288	0.290	0.273	0.270	0.254	0.245
$\nabla^2\rho_{BCP}$	0.328	0.237	0.254	0.255	0.308	0.433	0.449
V_{BCP}	-0.427	-0.582	-0.577	-0.515	-0.500	-0.466	-0.440
G_{BCP}	0.255	0.321	0.320	0.289	0.289	0.287	0.276
H_{BCP}	-0.173	-0.261	-0.257	-0.226	-0.212	-0.179	-0.164
δ	1.738	2.053	2.067	1.942	1.921	1.864	1.745
$\left\lvert\Delta Q_{\mathrm{An}}^{\mathrm{QTAIM}}\right\rvert$	2.364	2.130	2.035	2.097	2.009	1.986	1.993
	ThO_2^+	PaO_2^+	UO_2^+	NpO_2^+	PuO_2^+	AmO_2^+	CmO_2^+
D	698.5	830.3	765.4	690.9	587.7	468.0	458.3
R	1.860	1.764	1.750	1.728	1.711	1.714	1.745
ρ_{BCP}	0.228	0.314	0.325	0.338	0.347	0.339	0.307
$\nabla^2\rho_{BCP}$	0.370	0.224	0.241	0.249	0.278	0.383	0.477
V_{BCP}	-0.449	-0.672	-0.691	-0.722	-0.740	-0.703	-0.614
G_{BCP}	0.271	0.364	0.376	0.392	0.405	0.399	0.367
H_{BCP}	-0.178	-0.308	-0.315	-0.330	-0.335	-0.304	-0.247
δ	1.704	2.031	2.084	2.143	2.182	2.175	2.026
$\left\lvert\Delta Q_{\mathrm{An}}^{\mathrm{QTAIM}}\right\rvert$	1.785	1.885	1.726	1.604	1.487	1.363	1.300
	ThO_2^{2+}	PaO_2^{2+}	UO_2^{2+}	NpO_2^{2+}	PuO_2^{2+}	AmO_2^{2+}	CmO_2^{2+}
D	489.2	581.1	577.6	479.4	373.7	238.3	265.8
R	1.886	1.768	1.692	1.688	1.673	1.665	1.686
ρ_{BCP}	0.195	0.288	0.377	0.380	0.387	0.385	0.359
$\nabla^2\rho_{BCP}$	0.516	0.473	0.314	0.346	0.379	0.447	0.512
V_{BCP}	-0.388	-0.649	-0.891	-0.890	-0.902	-0.882	-0.790
G_{BCP}	0.258	0.383	0.485	0.488	0.499	0.497	0.459
H_{BCP}	-0.129	-0.265	-0.406	-0.402	-0.404	-0.385	-0.331
δ	1.598	2.046	2.305	2.336	2.363	2.360	2.266
$\left\lvert\Delta Q_{\mathrm{An}}^{\mathrm{QTAIM}}\right\rvert$	1.030	1.203	1.219	1.048	0.920	0.804	0.621

Table 4.2.2: The bond interaction energy D (kJ/mol), bond lengths R (Å), the electron density at the BCP ρ_{BCP} (a.u), the Laplacian at the BCP $\nabla^2\rho_{BCP}$ (a.u), the potential energy density V_{BCP} (a.u), the gradient kinetic energy density $G_{BCP}(a.u)$, the total energy of the BCP H_{BCP} (a.u), the delocalisation index δ (a.u), and the change of the QTAIM partial charge on the actinide atom $\left\lvert\Delta Q_{\mathrm{An}}^{\mathrm{QTAIM}}\right\rvert$ (a.u) of actinide dioxides. The bond interaction energy D is calculated using Equation 4.3.

positive sign of $\nabla^2\rho_{BCP}$ arises from the highly polarised bond. The total energy densities H_{BCP}, calculated as $H_{BCP} = G_{BCP} + V_{BCP}$, are all negative, i.e. are dominated by the potential energy densities V_{BCP}. The delocalisation indices δ, which indicate the number of exchanged electrons and can be considered as the bond order, are mostly larger than 1.7. The relation between optimised bond length R and ρ_{BCP} in the actinide oxide molecules and their cations is shown in Figure 4.1, and is well correlated with $R^2 = 0.954$ in exponential curve fitting. This suggests a good relationship between electron density and the bond length across different actinide elements in different charge states.

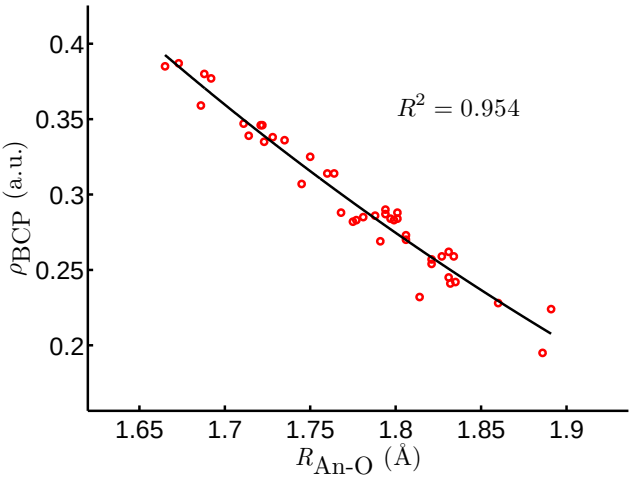

Figure 4.1: ρ_{BCP} against bond length in AnO and AnO_2 molecules, cations and dications. The R^2 value corresponds to exponential fitting: $\rho_{BCP} = 7.93\exp(-1.51R) - 0.246$.

	AnO	AnO^+	AnO^{2+}	AnO_2	AnO_2^+	AnO_2^{2+}
R	0.101	0.860	0.136	0.009	0.152	0.204
ρ_{BCP}	0.457	0.082	0.254	0.068	0.042	0.150
$\nabla^2\rho_{BCP}$	0.506	0.477	0.664	0.659	0.663	0.120
V_{BCP}	0.616	0.647	0.390	0.252	0.005	0.094
G_{BCP}	0.120	0.120	0.249	0.082	0.082	0.137
H_{BCP}	0.616	0.607	0.464	0.370	0.012	0.063
δ	0.153	0.691	0.001	0.170	0.076	0.138
$\lvert\Delta Q_{\mathrm{An}}^{\mathrm{QTAIM}}\rvert$	0.325	0.986	0.964	0.481	0.931	0.901

Table 4.2.3: The correlation coefficients R^2 from linear regression of the selected properties and D in actinide oxides.

Searching for a potential relationship between D and QTAIM properties,

the correlation coefficients R^2 between the selected properties and D in actinide oxides are listed in Table 4.2.3. The bond dissociation energy is essentially not linearly correlated with ρ_{BCP}, ∇^2_{BCP}, V_{BCP}, G_{BCP}, H_{BCP} and δ; however, I find strong correlation between D and $\left|\Delta Q^{\mathrm{QTAIM}}_{\mathrm{An}}\right|$, the absolute value of the change of the QTAIM partial charge on the actinide atom in the dissociation process, for the cationic systems, although the R^2 value is still low for the correlation for the neutral systems. These correlations are shown for AnO^{n+} $(n = 0, 1, 2)$ on the left hand side of Figure 4.2.

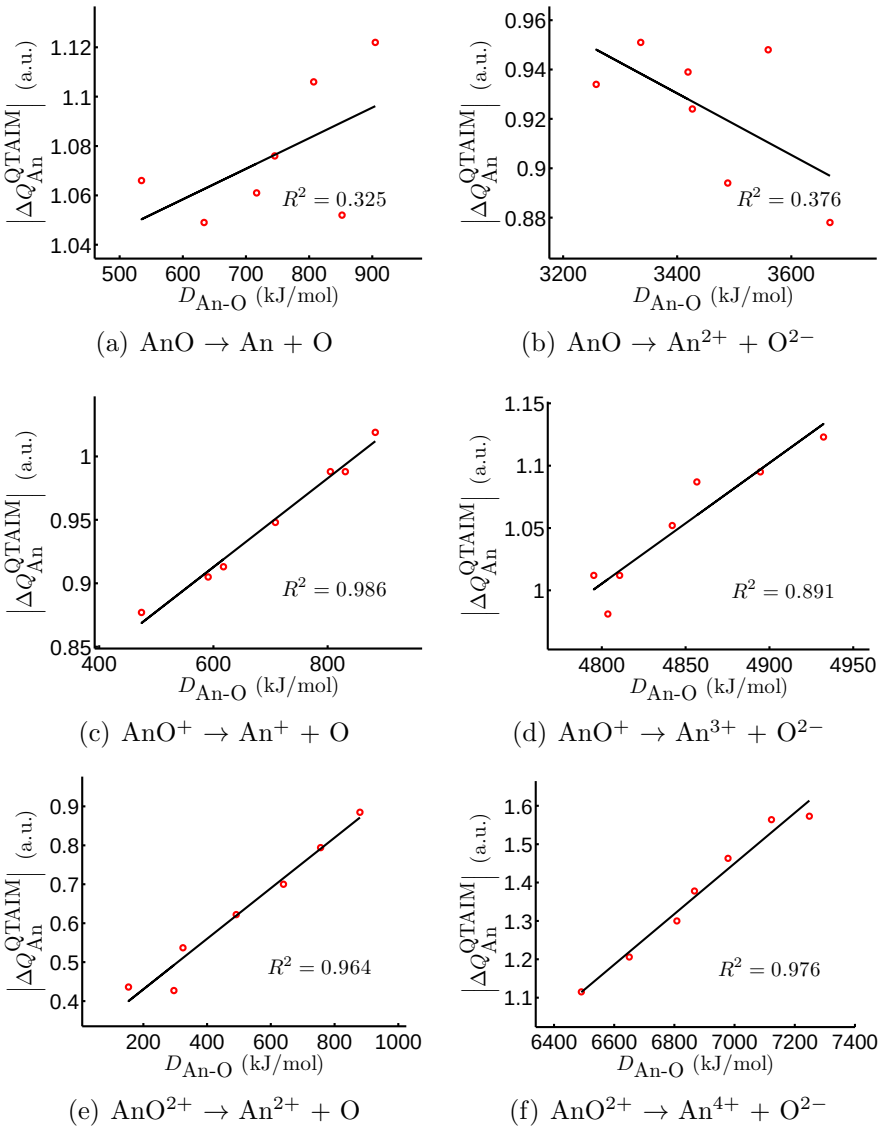

(a) $\mathrm{AnO} \rightarrow \mathrm{An} + \mathrm{O}$ (b) $\mathrm{AnO} \rightarrow \mathrm{An}^{2+} + \mathrm{O}^{2-}$

(c) $\mathrm{AnO}^{+} \rightarrow \mathrm{An}^{+} + \mathrm{O}$ (d) $\mathrm{AnO}^{+} \rightarrow \mathrm{An}^{3+} + \mathrm{O}^{2-}$

(e) $\mathrm{AnO}^{2+} \rightarrow \mathrm{An}^{2+} + \mathrm{O}$ (f) $\mathrm{AnO}^{2+} \rightarrow \mathrm{An}^{4+} + \mathrm{O}^{2-}$

Figure 4.2: $\left|\Delta Q^{\mathrm{QTAIM}}_{\mathrm{An}}\right|$ against D_{AnO} in actinide monoxides. The R^2 values correspond to linear fitting.

The dissociation energy D is evaluated with Eq. 4.1 and Eq. 4.3 for the monoxides and dioxides, respectively, in which I chose the dissociation process to form neutral oxygen atoms. Another route of dissociation is possible, e.g., I can choose to separate the actinide monoxide to form the oxygen dianion (O^{2-}):

$$D[\mathrm{AnO}^{n+}] = E[\mathrm{An}^{(n+2)+}] + E[\mathrm{O}^{2-}] - E[\mathrm{AnO}^{n+}]. \tag{4.4}$$

This will lead to very large bond dissociation energies due to the separation of opposite charge. However, the correlation with $\left|\Delta Q_{\mathrm{An}}^{\mathrm{QTAIM}}\right|$ still holds in the cationic cases even for this type of dissociation, which is shown in the right column of Figure 4.2. This type of correlation may arise from the ionicity of the actinide-oxygen bonds.

Table 4.2.4 shows the correlation of D (to neutral O atom) with the change of the QTAIM partial charge on the actinide atom in the dissociation process under different atomic charge analysis schemes; for the cationic species, Mulliken charges also show good correlation for AnO^{2+}, AnO_2^+ and AnO_2^{2+} ($R^2 > 0.780$), but the correlation is poor for AnO^+ with $R^2 = 0.236$; Hirshfeld charges show good correlation for AnO^{2+} and AnO_2^+ ($R^2 > 0.878$) but poor correlation for AnO^+ and AnO_2^{2+}; natural charges show good correlation for AnO^{2+} and AnO_2^{2+} ($R^2 > 0.761$) and medium correlation for AnO^+ and AnO_2^+ ($R^2 = 0.613$ and 0.566, respectively). Obviously, $\left|\Delta Q_{\mathrm{An}}^{\mathrm{QTAIM}}\right|$ correlates better than other atomic charge analysis schemes for the cationic species of actinide oxides.

Method	$\left\|\Delta Q_{\mathrm{An}}^{\mathrm{QTAIM}}\right\|$	$\left\|\Delta Q_{\mathrm{An}}^{\mathrm{Mulliken}}\right\|$	$\left\|\Delta Q_{\mathrm{An}}^{\mathrm{Hirshfeld}}\right\|$	$\left\|\Delta Q_{\mathrm{An}}^{\mathrm{natural}}\right\|$
$D(\mathrm{AnO})$	0.329	0.620	0.233	0.045
$D(\mathrm{AnO}^+)$	0.986	0.236	0.082	0.613
$D(\mathrm{AnO}^{2+})$	0.964	0.978	0.878	0.968
$D(\mathrm{AnO_2})$	0.481	0.341	0.072	0.000
$D(\mathrm{AnO_2^+})$	0.931	0.780	0.925	0.566
$D(\mathrm{AnO_2^{2+}})$	0.901	0.896	0.303	0.761

Table 4.2.4: The correlation coefficients R^2 from linear regression of $D_{\text{An-O}}$ against $|\Delta Q_{\mathrm{An}}|$ under different atomic charge analysis schemes.

4.3 Summary

In summary, in order to obtain a reliable electron density for the subsequent QTAIM analysis, I benchmarked several computational methods by calculating the ionisation energies and bond dissociation energies of actinide oxides. For the exchange-correlation functionals, TPSSh usually gives slightly smaller MAEs than TPSS and B3LYP; for the inclusion of relativistic effects, the utilizing of ECP and associated basis sets gives smaller MAEs than the using of DKH/DKHSO Hamiltonian with the SARC basis sets. The inclusion of ZPE and BSSE correction does not improve the result, hence these two corrections are not applied in subsequent calculations.

To find possible relationships between bond strength and QTAIM properties, I performed QTAIM analysis on the electron densities of these actinide oxides. The bond dissociation energy is not well correlated with ρ_{BCP}, ∇^2_{BCP}, V_{BCP}, G_{BCP}, H_{BCP} or δ; however, in all cationic actinide oxides, I found strong correlation between the bond dissociation energy and $\left|\Delta Q^{\mathrm{QTAIM}}_{\mathrm{An}}\right|$, the absolute value of the change of the QTAIM partial charge on the actinide atom. This correlation is also valid while separating the actinide monoxide to form the oxygen dianion.

Chapter 5

Actinide Compounds with N-based Ligands

5.1 Actinide compounds with a single N-based ligand

The eventual target molecules of this research are complexes with BTP-like ligands, in which the actinide-ligand bonding is likely to be different from the actinide-oxygen bonding in the previous chapter; hence, I have calculated some simple compounds which contain actinide-nitrogen bonding. In this section, I focus on the relation between bond interaction energies and QTAIM properties of actinide compounds with a single nitrogen-based ligand; although these are not chemically realistic structures, they are clearly important in relation to the structures of the real compounds.

To simplify the computation, I chose small ligands which are representative of electron withdrawing or donating effects. I chose three X-type ligands: NH_2^-, $N(CH_3)_2^-$, $N(CF_3)_2^-$, and four L-type ligands: pyridine (Py), pentafluoropyridine (PyF), pyrazine (Pz) and 1,3,5-triazine (Tz). The L-type ligands are depicted in Figure 5.1. All molecular structures in this section are optimised with the TPSSh functional with the Stuttgart small-core ECP and basis sets for the actinides and cc-pVTZ basis sets for other elements. Molecular structures are constrained to have C_{2V} point group symmetry.

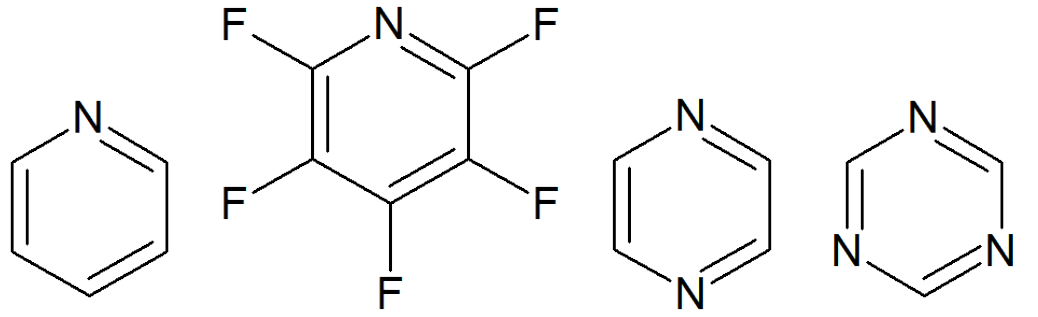

(a) Pyridine (Py) (b) Pentafluoropyridine (PyF) (c) Pyrazine (Pz) (d) 1,3,5-Triazine (Tz)

Figure 5.1: Structures of selected L-type ligands.

I assume all actinide atoms are in the trivalent state An(III); hence the molecules I calculate in this section are doubly-charged cations for AnX-type complexes, and triply-charged cations for AnL-type complexes. The actinide-nitrogen bond strength is represented as the interaction energy E_{int}:

$$E^n_{\text{int}}[\text{MX}^{(n-m)+}] = E[\text{MX}^{(n-m)+}] - (E[\text{M}^{n+}] + E[\text{X}^{m-}]) \tag{5.1}$$

where n is the positive charge of the actinide atom, M stands for the metal, and X stands for the corresponding ligand with negative charges m^- in the actinide complexes with a single ligand. For X-type ligands, two types of interaction energies, E^3_{int} and E^2_{int} are calculated with Eq. 5.1, in which the ligand fragments correspond to X^- anion and X$\cdot$ radical, respectively; for L-type ligands, only the E^3_{int}-type bond interaction energy is calculated. Note that E_{int} generally has a negative sign, which is opposite to the dissociation energy D used in previous chapter.

Calculated E_{int}, bond lengths and selected QTAIM properties of these single-ligand complexes are summarised in Table 5.1.1 and Table 5.1.2. For the X-type complexes, Table 5.1.1 shows that the AmX complexes give a An-N bond length which is much longer than for the other actinides, which is also reflected in a lower E^2_{int}. The PuX complexes also have long bond lengths, shorter than only the AmX complexes, as well as a lower E^2_{int}. However, the

E^3_{int} increases as the atomic number increases, except for a little decrease in the CmX complexes. Similarly, the calculated ρ_{BCP} and H_{BCP} also give abruptly smaller values in the AmX complexes, which implies a possible relation with the long bond length. All calculated ρ_{BCP} are smaller than 0.18, indicating that the An-N bond is not as covalent (at least in the QTAIM sense) as the An-O bond in the actinide oxides; this is most likely because there is significant multiple bond character in the oxides, but not in the An-N bond. The H_{BCP} is still negative, but its magnitude is much smaller than in the actinide oxides. The delocalisation indices δ are around 0.6 to 1.4, which are also much smaller than for the oxides.

For the L-type complexes, Table 5.1.2 has some "not available" entries, which means the molecules did not fully optimise or did not pass the wave-function stability check. Moreover, geometry optimisation of PuTz and AmTz gives extremely large An-N bond lengths, which means a single 1,3,5-triazine may not bind to these two cations. Similarly to the X-type ligands, the AmL and PuL complexes have longer bond lengths than the other actinides and the trend of E_{int} is also similar to the trend in X-type complexes. The calculated ρ_{BCP} and H_{BCP} are even smaller, especially for the AmL and PuL complexes, which is almost certainly a consequence of the long bond length. The H_{BCP} are only slightly negative, which means the potential energy density V_{BCP} and kinetic energy density G_{BCP} are almost comparable. These ρ_{BCP} and H_{BCP} data are reasonably similar to cyclopentadienyl actinide complexes calculated previously, e.g., $AnCp_4$[29] and $AnCp_3$[28]. The delocalisation indices δ are around 0.2 to 0.9, indicating the covalent interaction is even weaker than the X-type complexes.

The correlation between bond length and ρ_{BCP} is shown in Figure 5.2. All data from both X type and L-type complexes are well correlated together with $R^2 = 0.985$ in exponential curve fitting, which implies the physics in the bonding of the two type complexes are not too different. However, Figure 5.3 shows that the bond interaction energy is not well correlated with ρ_{BCP}, no

			An-X^{2+}, An={Th-Cm}, X^-=NH_2^-				
E^3_{int}	-2338.4	-2369.2	-2397.7	-2430.5	-2487.0	-2559.5	-2463.0
E^2_{int}	-557.1	-509.9	-469.8	-402.6	-308.2	-243.2	-376.7
R	2.087	2.079	2.056	2.046	2.063	2.300	2.032
ρ_{BCP}	0.154	0.154	0.158	0.161	0.152	0.087	0.158
$\nabla^2\rho_{BCP}$	0.212	0.241	0.302	0.334	0.357	0.266	0.403
V_{BCP}	-0.223	-0.223	-0.242	-0.246	-0.230	-0.115	-0.247
G_{BCP}	0.138	0.141	0.158	0.165	0.160	0.091	0.174
H_{BCP}	-0.085	-0.081	-0.083	-0.081	-0.070	-0.024	-0.073
δ	1.273	1.277	1.328	1.376	1.396	0.908	1.384
$Q^{\text{QTAIM}}_{\text{An}}$	2.365	2.362	2.332	2.291	2.220	1.988	2.268
			An-X^{2+}, An={Th-Cm}, X^-=$N(CH_3)_2^-$				
E^3_{int}	-2372.2	-2405.5	-2424.6	-2463.2	-2529.0	-2631.0	-2493.2
E^2_{int}	-586.0	-553.4	-493.5	-431.8	-347.0	-308.9	-403.8
R	2.038	2.053	2.019	2.014	2.079	2.376	2.014
ρ_{BCP}	0.179	0.164	0.178	0.179	0.150	0.078	0.169
$\nabla^2\rho_{BCP}$	0.181	0.231	0.274	0.314	0.333	0.212	0.398
V_{BCP}	-0.268	-0.239	-0.277	-0.277	-0.224	-0.093	-0.267
G_{BCP}	0.157	0.149	0.173	0.177	0.153	0.073	0.183
H_{BCP}	-0.112	-0.091	-0.104	-0.099	-0.070	-0.020	-0.084
δ	1.358	1.268	1.370	1.403	1.304	0.624	1.408
$Q^{\text{QTAIM}}_{\text{An}}$	2.197	2.206	2.182	2.131	2.019	1.819	2.099
			An-X^{2+}, An={Th-Cm}, X^-=$N(CF_3)_2^-$				
E^3_{int}	-2021.3	-2056.1	-2086.1	-2118.0	-2179.4	-2272.3	-2151.8
E^2_{int}	-534.8	-491.5	-447.7	-367.8	-265.7	-198.0	-343.8
R	2.151	2.128	2.103	2.088	2.108	2.350	2.073
ρ_{BCP}	0.140	0.144	0.148	0.151	0.141	0.079	0.149
$\nabla^2\rho_{BCP}$	0.160	0.193	0.252	0.288	0.314	0.238	0.343
V_{BCP}	-0.183	-0.192	-0.210	-0.216	-0.201	-0.099	-0.219
G_{BCP}	0.112	0.120	0.137	0.144	0.140	0.079	0.153
H_{BCP}	-0.072	-0.072	-0.074	-0.072	-0.061	-0.020	-0.067
δ	0.955	0.996	1.054	1.122	1.164	0.739	1.118
$Q^{\text{QTAIM}}_{\text{An}}$	2.418	2.398	2.366	2.316	2.226	1.979	2.294

Table 5.1.1: The bond interaction energy E_{int} (kJ/mol), bond lengths R (Å), the electron density at the BCP ρ_{BCP} (a.u), the Laplacian at the BCP $\nabla^2\rho_{BCP}$ (a.u), the potential energy density V_{BCP} (a.u), the gradient kinetic energy density $G_{BCP}(a.u)$, the total energy of the BCP H_{BCP} (a.u), the delocalisation index δ (a.u), and the QTAIM partial charge on the actinide atom $Q^{\text{QTAIM}}_{\text{An}}$ (a.u) of actinide complexes with X-type ligands.

An-L^{3+}, An={Th-Cm}, L=Py							
E^3_{int}	-724.5	-762.1	-786.2	-811.4	-881.4	-1000.9	-841.5
R	2.266	2.229	2.204	2.199	2.435	2.827	2.221
ρ_{BCP}	0.114	0.121	0.125	0.125	0.070	0.030	0.112
$\nabla^2\rho_{BCP}$	0.134	0.148	0.190	0.209	0.170	0.086	0.230
V_{BCP}	-0.131	-0.142	-0.155	-0.156	-0.073	-0.023	-0.141
G_{BCP}	0.082	0.089	0.101	0.104	0.058	0.022	0.099
H_{BCP}	-0.049	-0.052	-0.054	-0.052	-0.015	-0.001	-0.042
δ	0.787	0.843	0.876	0.902	0.549	0.265	0.806
$Q^{\text{QTAIM}}_{\text{An}}$	2.551	2.511	2.476	2.426	2.155	1.91	2.364
An-L^{3+}, An={Th-Cm}, L=PyF							
E^3_{int}	-631.5	-693.8	-689.8	-718.8	-836.0	N/A	-757.0
R	2.327	2.342	2.267	2.307	2.875	N/A	2.501
ρ_{BCP}	0.095	0.088	0.103	0.093	0.025	N/A	0.057
$\nabla^2\rho_{BCP}$	0.160	0.184	0.217	0.221	0.079	N/A	0.158
V_{BCP}	-0.107	-0.100	-0.127	-0.112	-0.018	N/A	-0.058
G_{BCP}	0.073	0.073	0.091	0.084	0.019	N/A	0.049
H_{BCP}	-0.033	-0.030	-0.036	-0.029	0.001	N/A	-0.009
δ	0.666	0.637	0.752	0.715	0.233	N/A	0.435
$Q^{\text{QTAIM}}_{\text{An}}$	2.602	2.560	2.52	2.415	1.985	N/A	2.197
An-L^{3+}, An={Th-Cm}, L=Pz							
E^3_{int}	-615.7	-656.4	-680.7	-756.8	-893.0	-1036.9	-809.5
R	2.310	2.297	2.373	2.476	2.723	2.977	2.518
ρ_{BCP}	0.106	0.108	0.089	0.067	0.039	0.022	0.059
$\nabla^2\rho_{BCP}$	0.120	0.120	0.144	0.156	0.102	0.061	0.140
V_{BCP}	-0.115	-0.114	-0.093	-0.068	-0.032	-0.014	-0.058
G_{BCP}	0.073	0.072	0.064	0.053	0.029	0.015	0.046
H_{BCP}	-0.043	-0.042	-0.028	-0.015	-0.004	0.001	-0.011
δ	0.710	0.718	0.613	0.504	0.320	0.208	0.437
$Q^{\text{QTAIM}}_{\text{An}}$	2.568	2.500	2.370	2.223	2.004	1.922	2.142
An-L^{3+}, An={Th-Cm}, L=Tz							
E^3_{int}	-574.5	-615.5	-626.7	-695.6	N/A	N/A	-751.5
R	2.325	2.288	2.351	2.524	N/A	N/A	2.550
ρ_{BCP}	0.099	0.105	0.088	0.059	N/A	N/A	0.053
$\nabla^2\rho_{BCP}$	0.142	0.152	0.180	0.151	N/A	N/A	0.146
V_{BCP}	-0.110	-0.117	-0.099	-0.058	N/A	N/A	-0.052
G_{BCP}	0.073	0.077	0.072	0.048	N/A	N/A	0.044
H_{BCP}	-0.037	-0.039	-0.027	0.010	N/A	N/A	-0.008
δ	0.721	0.764	0.677	0.492	N/A	N/A	0.437
$Q^{\text{QTAIM}}_{\text{An}}$	2.592	2.540	2.429	2.235	N/A	N/A	2.161

Table 5.1.2: The bond interaction energy E_{int} (kJ/mol), bond lengths R (Å), the electron density at the BCP ρ_{BCP} (a.u), the Laplacian at the BCP $\nabla^2\rho_{BCP}$ (a.u), the potential energy density V_{BCP} (a.u), the gradient kinetic energy density $G_{BCP}(a.u)$, the total energy of the BCP H_{BCP} (a.u), the delocalisation index δ (a.u), and the QTAIM partial charge on the actinide atom $Q^{\text{QTAIM}}_{\text{An}}$ (a.u) of actinide complexes with L-type ligands. N/A = not available.

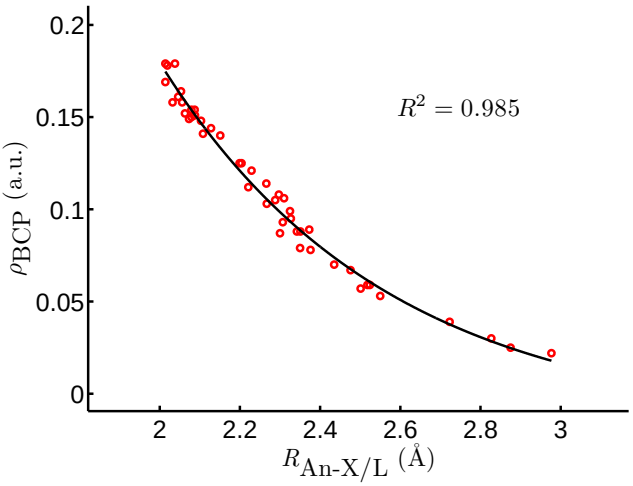

Figure 5.2: ρ_{BCP} against bond length in X-type and L-type actinide complexes. The R^2 value corresponds to exponential fitting: $\rho_{BCP} = 6.85\exp(-1.78R) - 0.017$.

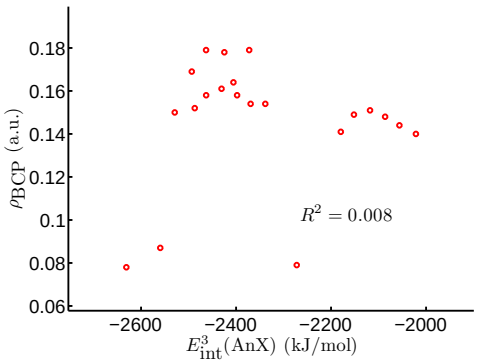

(a) ρ_{BCP} vs E^3_{int}, X-type

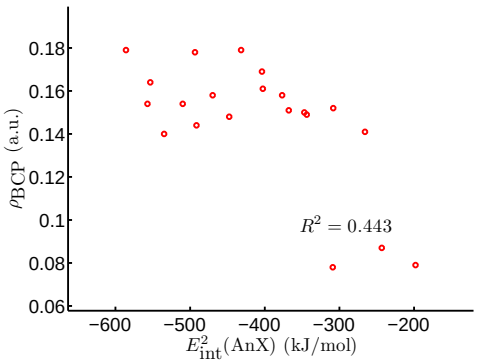

(b) ρ_{BCP} vs E^2_{int}, X-type

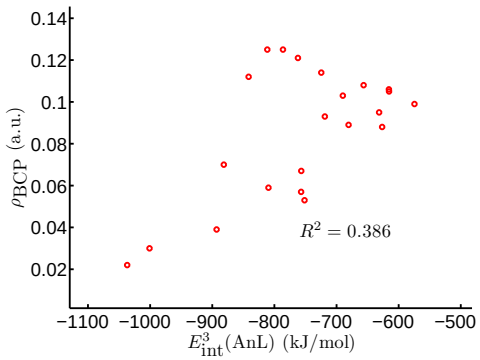

(c) ρ_{BCP} vs E^3_{int}, L-type

Figure 5.3: ρ_{BCP} against E_{int} in actinide complexes with a single ligand. The R^2 values correspond to linear fitting.

matter which type of ligand. Similarly, ∇^2_{BCP}, H_{BCP} and δ are also not well correlated with bond interaction energies (R^2 range from 0.000 to 0.516).

The QTAIM charges of the actinide atoms, $Q^{\mathrm{QTAIM}}_{\mathrm{An}}$, are also listed in Table 5.1.1 and Table 5.1.2. Similar to the trend of bond length and E_{int}, there is a significant decrease of the actinide QTAIM charges beginning from the uranium complexes, and the lowest values occur in americum complexes, which are lower than 2.0. However, the formal charge of the actinide atom in these complexes should be 3.0. This indicates strong electron donation from both X-type and L-type ligand, leading to an electronic configuration close to Am(II) in the strongest case. I find very good negative correlations between the change of the partial charge on the actinide atoms on going from free ion to complex formation $\left|\Delta Q^{\mathrm{QTAIM}}_{\mathrm{An}}\right|$ and E^3_{int} as shown in Figure 5.4, with all the R^2 values larger than 0.873. Besides, as shown in Figure 5.5, the E^2_{int} of X-type complexes also show good correlation in most cases, except for some AmX complexes.

Considering the $AmPy^{3+}$ complex as the combination of Am^{3+} ion and pyridine molecule, one may expect the configuration of the americium atom in the complex to be [Rn]$5f^6$, and the molecular orbitals of the complex based on the pyridine's π orbitals to be fully occupied. However, as Figure 5.6 shows, the alpha LUMO of the $AmPy^{3+}$ complex is almost purely a pyridine π orbital, which implies strong ligand-to-metal charge transfer (LMCT); moreover, the configuration of the americium atom is almost half-filled [Rn]$5f^7$ by population analysis, which also suggests the Am(II) oxidation state.

To clarify if this charge-transfer phenomenon is a method-sensitive result or not, single-point calculations of $AmPy^{3+}$ at the Hartree-Fock (HF) and MP2 levels were carried out; a single-point TPSSh calculation under aqueous environvent simulated with PCM, at the gas-phase geometry, was also performed for comparison. The Mulliken charge of the americium atom, $Q^{\mathrm{Mulliken}}_{\mathrm{Am}}$, from these calculations are listed in Table 5.1.3. Obviously, gas-phase TPSSh, HF and MP2 give similar results for the Mulliken charge, but the inclusion

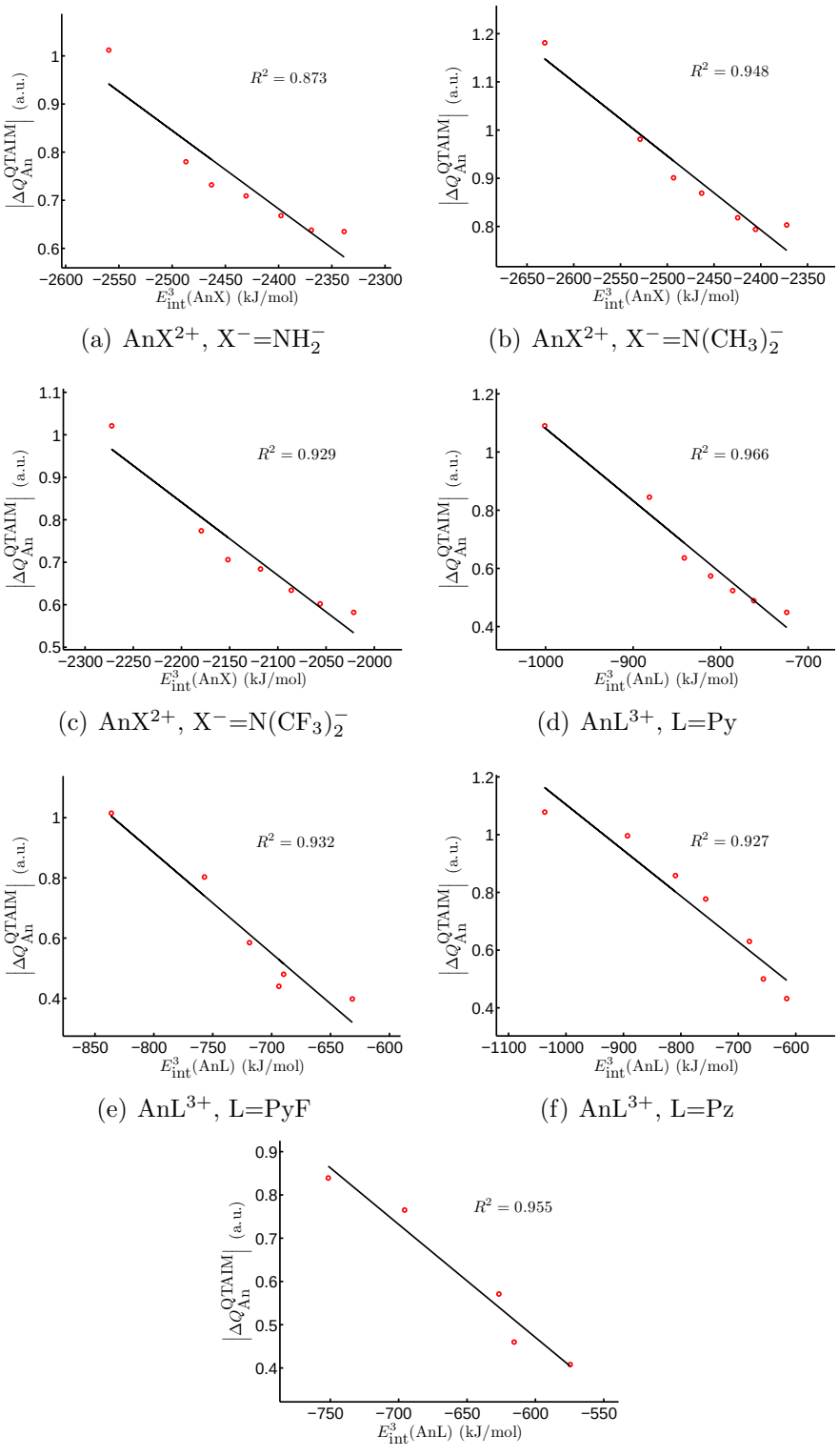

(a) AnX^{2+}, X^-=NH_2^- (b) AnX^{2+}, X^-=$N(CH_3)_2^-$

(c) AnX^{2+}, X^-=$N(CF_3)_2^-$ (d) AnL^{3+}, L=Py

(e) AnL^{3+}, L=PyF (f) AnL^{3+}, L=Pz

(g) AnL^{3+}, L=Tz

Figure 5.4: $\left|\Delta Q_{\mathrm{An}}^{\mathrm{QTAIM}}\right|$ against E^3_{int} in complexes of actinides with single ligands. The R^2 values correspond to linear fitting.

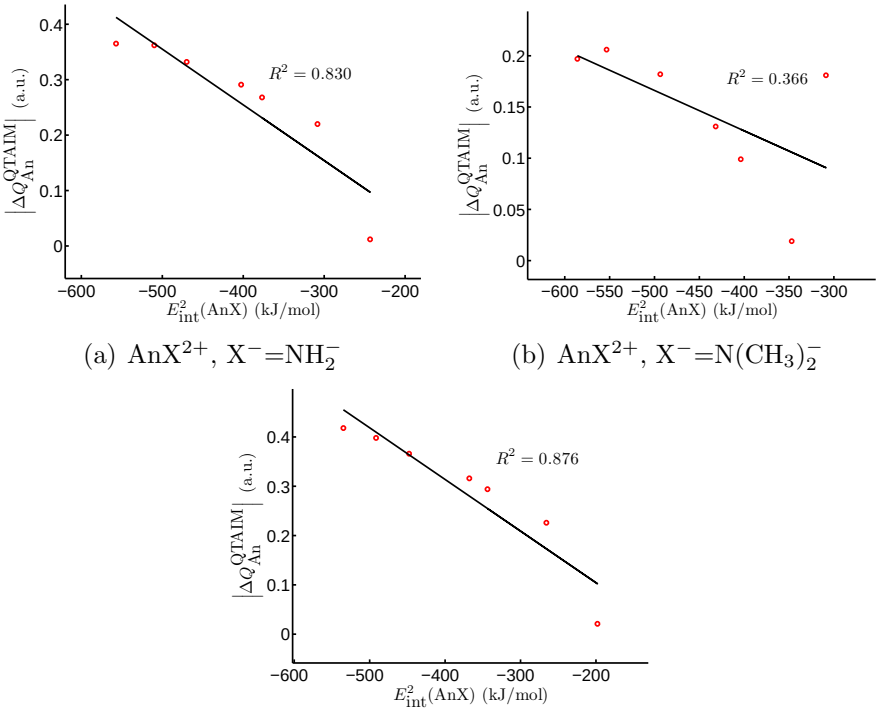

(a) AnX^{2+}, X^-=NH_2^-

(b) AnX^{2+}, X^-=$N(CH_3)_2^-$

(c) AnX^{2+}, X^-=$N(CF_3)_2^-$

Figure 5.5: $\left|\Delta Q_{\mathrm{An}}^{\mathrm{QTAIM}}\right|$ against E^2_{int} in complexes of actinides with single ligands. The R^2 values correspond to linear fitting.

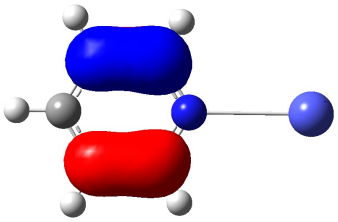

Figure 5.6: The alpha LUMO of $AmPy^{3+}$ calculated with the TPSSh functional. The isovalue is 0.05.

of solvation really makes a large difference. The $Q_{\mathrm{Am}}^{\mathrm{Mulliken}}$ calculated using TPSSh/PCM is very near to 3.0, which means the LMCT is greatly reduced; as Figure 5.7 shows, the alpha LUMO of $AmPy^{3+}$ is now an f orbital, which implies the $[Rn]5f^6$ configuration and Am(III) in this case. The Py π orbital is the alpha HOMO in this case (not shown). I will return to this in the subsequent sections.

Method	$Q_{\mathrm{Am}}^{\mathrm{Mulliken}}$
TPSSh	1.840
HF	1.889
MP2	1.866
TPSSh with PCM(water)	2.814

Table 5.1.3: Calculated $Q_{\mathrm{Am}}^{\mathrm{Mulliken}}$ in $AmPy^{3+}$ using different methods.

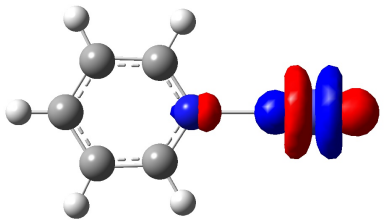

Figure 5.7: The alpha LUMO of $AmPy^{3+}$ calculated with the TPSSh functional and PCM(Water). The isovalue is 0.05.

It should be noted that although it is in theory possible to computationally modify the X-type ligands NR_2^- to L-type ligands NR_3, the geometry optimisation of most of these complexes did not converge. Figure 5.8 shows the potential energy surface of the hypothetical Am-NH_3 complex. Obviously, the potential well is not deep enough, hence it is not possible to get a feasible geometry to calculate the interaction energy and perform the QTAIM analysis. Calculations with L-type NR_3 ligands were therefore not pursued further.

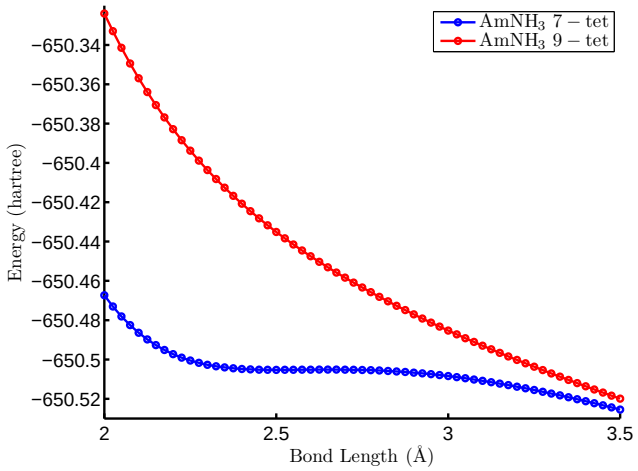

Figure 5.8: Potential energy surface of hypothetical Am-NH_3 whose geometry did not converge. Results with spin multiplicity = 7 shown in blue line, and results with spin multiplicity = 9 shown in red line.

5.2 Actinide compounds with three N-based ligands

Geometry optimisations of trivalent actinide complexes with three ligands were performed from C_{3V} symmetrised structures as initial guesses. To simplify the computation, I chose the L-type ligands from the previous section since they converge more quickly than the X-type complexes in most cases; besides, the L-type ligands are closer to BTP than the X-type ligands. All molecular structures in this section were optimised with the TPSSh functional with the Stuttgart small-core ECP and basis set for actinides and cc-pVTZ basis sets for other elements. Similar to the previous section, I assume all the actinide atoms are in the trivalent state An(III); hence, the molecules I calculated in this section are triply-charged cations since only L-type ligands are selected. The bond interaction energies E^3_{int} of the An-N bonding in these complexes are calculated as follow:

$$E^3_{\text{int}}[\text{ML}_3^{3+}] = \frac{E[\text{ML}_3^{3+}] - (E[\text{M}^{3+}] + E[\text{L}_3])}{3} \tag{5.2}$$

in which M stands for the metal, $E[L_3]$ corresponds to the energy of the three L-type ligands in the geometry of corresponding complex. Bond length and QTAIM properties used in the following discussion are the average value of the three bonds since some of the optimised structures did not maintain perfect three fold symmetry.

The E^3_{int}, bond length and selected QTAIM properties of selected trivalent actinide complexes are summarised in Table 5.2.1. Obviously, their average bond lengths are longer than the single ligand complexes, which is also reflected in E^3_{int}, ρ_{BCP}, H_{BCP} and δ. More "not available" entries appear in Table 5.2.1, which reflects the higher difficulty of geometry optimisation. Similar to the single ligand complexes, AmL_3 and PuL_3 have longer bond lengths than the other actinides, which is also reflected in lower values of E^3_{int}, ρ_{BCP}, H_{BCP}, δ; besides, low actinide QTAIM charges (< 2.1) are found in the AmL_3^{3+} complexes, indicating strong electron donation from the ligands, again implying Am(II). The delocalisation indices δ of these An-N bonds are between 0.37 and 0.60, indicating the covalent interaction in these bonds are weaker than in the single-ligand complexes in the previous section.

The correlation between bond length and ρ_{BCP} is shown in Figure 5.9. All data from complexes with L-type ligands are considered together with $R^2 = 0.801$, lower than for single-ligand complexes, in exponential curve fitting. Figure 5.10 indicates the absence of correlation between the bond interaction energy E^3_{int} and ρ_{BCP}. Likewise, ∇^2_{BCP}, H_{BCP} and δ are also not well correlated with bond interaction energies (R^2 range from 0.062 to 0.165). However, $\left|\Delta Q^{\text{QTAIM}}_{\text{An}}\right|$ again shows resonable to good negative correlation with E^3_{int} (Figure 5.11); all the R^2 values are larger than 0.652.

As aforementioned, one may expect a $[\text{Rn}]5f^6$ configuration for the americium atom and fully occupied ligand orbitals in AmL_3^{3+}. However, as Figure 5.12 shows, the alpha LUMO of $AmPz_3^{3+}$ has substantial contribution from pyrazine's occupied σ orbital, which implies LMCT; moreover, the occupancy of the f orbitals in the americium atom is larger than 6.0 by population

AnL_3^{3+}, An={Th-Cm}, L=Py							
E^3_{int}	-541.7	-536.2	N/A	N/A	-577.2	-590.2	-578.1
R	2.392	2.416	N/A	N/A	2.363	2.366	2.355
ρ_{BCP}	0.089	0.078	N/A	N/A	0.083	0.082	0.083
$\nabla^2\rho_{BCP}$	0.126	0.164	N/A	N/A	0.185	0.180	0.198
V_{BCP}	-0.089	-0.082	N/A	N/A	-0.091	-0.089	-0.096
G_{BCP}	0.060	0.062	N/A	N/A	0.068	0.067	0.073
H_{BCP}	-0.029	-0.021	N/A	N/A	-0.022	-0.022	-0.023
δ	0.598	0.539	N/A	N/A	0.582	0.578	0.548
$Q_{\text{An}}^{\text{QTAIM}}$	2.193	2.292	N/A	N/A	2.156	2.084	2.199
AnL_3^{3+}, An={Th-Cm}, L=PyF							
E^3_{int}	-441.5	-457.2	N/A	N/A	-491.9	N/A	-497.4
R	2.480	2.475	N/A	N/A	2.414	N/A	2.392
ρ_{BCP}	0.069	0.066	N/A	N/A	0.071	N/A	0.073
$\nabla^2\rho_{BCP}$	0.142	0.162	N/A	N/A	0.188	N/A	0.197
V_{BCP}	-0.068	-0.067	N/A	N/A	-0.078	N/A	-0.083
G_{BCP}	0.052	0.054	N/A	N/A	0.063	N/A	0.066
H_{BCP}	-0.016	-0.013	N/A	N/A	-0.016	N/A	-0.017
δ	0.463	0.459	N/A	N/A	0.493	N/A	0.475
$Q_{\text{An}}^{\text{QTAIM}}$	2.419	2.378	N/A	N/A	2.246	N/A	2.284
AnL_3^{3+}, An={Th-Cm}, L=Pz							
E^3_{int}	-463.4	N/A	-474.0	-485.8	-506.2	-530.1	-504.8
R	2.414	N/A	2.420	2.405	2.429	2.526	2.382
ρ_{BCP}	0.085	N/A	0.077	0.077	0.072	0.057	0.079
$\nabla^2\rho_{BCP}$	0.119	N/A	0.166	0.183	0.174	0.154	0.185
V_{BCP}	-0.083	N/A	-0.082	-0.085	-0.077	-0.058	-0.088
G_{BCP}	0.057	N/A	0.062	0.065	0.060	0.048	0.067
H_{BCP}	-0.027	N/A	-0.020	-0.019	-0.017	-0.010	-0.021
δ	0.573	N/A	0.532	0.541	0.506	0.403	0.519
$Q_{\text{An}}^{\text{QTAIM}}$	2.201	N/A	2.266	2.215	2.091	1.880	2.180
AnL_3^{3+}, An={Th-Cm}, L=Tz							
E^3_{int}	-426.6	-425.6	N/A	-439.9	N/A	-490.0	-466.9
R	2.427	2.473	N/A	2.441	N/A	2.593	2.398
ρ_{BCP}	0.082	0.069	N/A	0.072	N/A	0.048	0.075
$\nabla^2\rho_{BCP}$	0.126	0.151	N/A	0.171	N/A	0.140	0.185
V_{BCP}	-0.080	-0.069	N/A	-0.076	N/A	-0.047	-0.083
G_{BCP}	0.056	0.053	N/A	0.060	N/A	0.041	0.065
H_{BCP}	-0.024	-0.016	N/A	-0.017	N/A	-0.006	-0.019
δ	0.573	0.506	N/A	0.513	N/A	0.371	0.518
$Q_{\text{An}}^{\text{QTAIM}}$	2.212	2.331	N/A	2.264	N/A	1.841	2.212

Table 5.2.1: The bond interaction energy E^3_{int} (kJ/mol), bond lengths R (Å), the electron density at the BCP ρ_{BCP} (a.u), the Laplacian at the BCP $\nabla^2\rho_{BCP}$ (a.u), the potential energy density V_{BCP} (a.u), the gradient kinetic energy density $G_{BCP}(a.u)$, the total energy of the BCP H_{BCP} (a.u), the delocalisation index δ (a.u), and the QTAIM partial charge on the actinide atom $Q_{\text{An}}^{\text{QTAIM}}$ (a.u) of actinide complexes with three L-type ligands. N/A = not available.

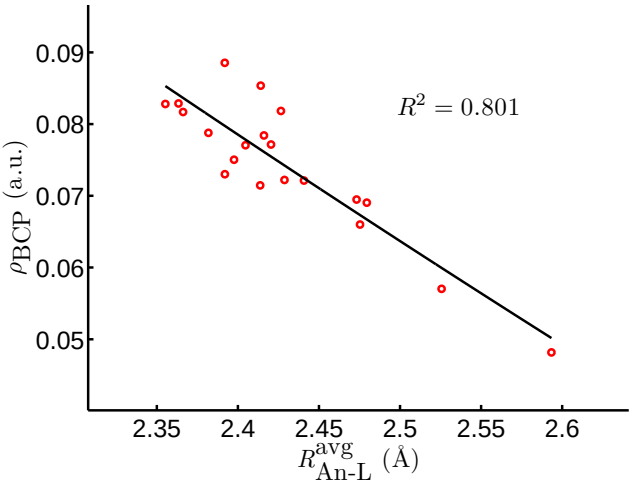

Figure 5.9: ρ_{BCP} against averaged bond length in actinide complexes with three L-type ligands. Note that the R^2 value corresponds to exponential fitting $\rho_{BCP} = 1.081\exp(-0.259R) - 0.502$ although it looks like a straight line.

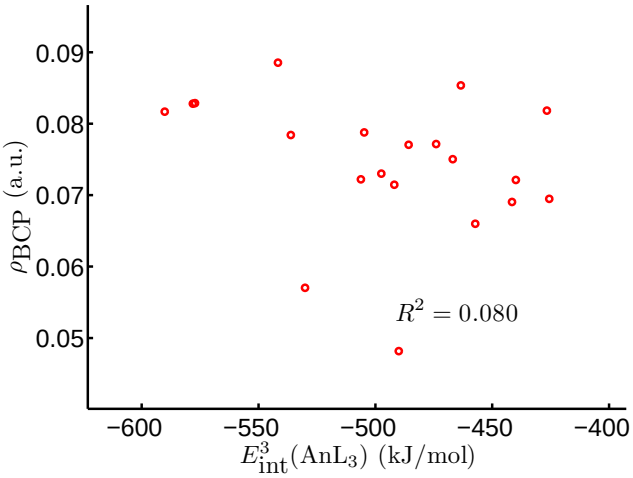

Figure 5.10: ρ_{BCP} against E^3_{int} in actinide complexes with three L-type ligands. The R^2 value corresponds to linear fitting.

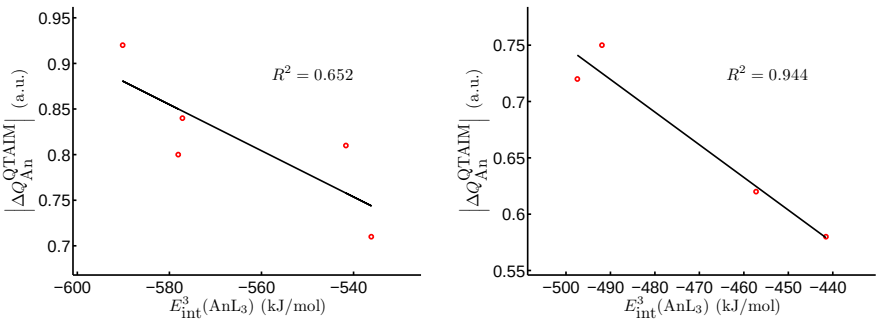

(a) AnL^{3+}, L=Py (b) AnL^{3+}, L=PyF

(c) AnL^{3+}, L=Pz (d) AnL^{3+}, L=Tz

Figure 5.11: $\left|\Delta Q_{\mathrm{An}}^{\mathrm{QTAIM}}\right|$ against E_{int}^{3} in complexes of actinides with three L-type ligands. The R^2 values correspond to linear fitting.

analysis, i.e., similar to the Am(II) oxidation state discussed in the previous section.

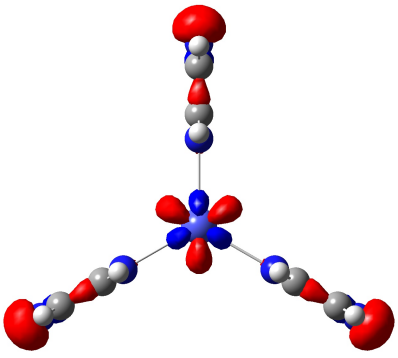

Figure 5.12: The alpha LUMO of $AmPz_3^{3+}$ calculated with the TPSSh functional. The isovalue is 0.05.

To find out if the method once again affects this charge-transfer phenomenon, single-point calculations of $AmPz_3^{3+}$ at the HF and MP2 levels were carried out; also, a TPSSh calculation under aqueous environvent simulated

with PCM was performed. The Mulliken charges of the americium atom, $Q_{\mathrm{Am}}^{\mathrm{Mulliken}}$, from these calculations are listed in Table 5.2.2. HF and MP2 give higher $Q_{\mathrm{Am}}^{\mathrm{Mulliken}}$ than TPSSh, hence I performed an additional single-point calculation with the TPSS correlational functional and exact Hartree-Fock exchange, which gives a similar result to HF. The alpha LUMO from the HF calculation is shown in Figure 5.13, which is totally different to the result with TPSSh; the first few unoccupied orbitals do not contain any character from occupied orbitals of pyrazine. The $Q_{\mathrm{Am}}^{\mathrm{Mulliken}}$ calculated using TPSSh/PCM is 2.431, which is much larger than all the other methods calculated without PCM. Figure 5.14 shows that the alpha LUMO of $AmPz_3^{3+}$ under PCM is mostly an f orbital from the americium atom, which implies the absence of LMCT, leading to a more Am(III)-like oxidation state.

Method	$Q_{\mathrm{Am}}^{\mathrm{Mulliken}}$
TPSSh	1.590
TPSS+100% HF Exchange	2.193
HF	2.173
MP2	1.979
TPSSh with PCM(water)	2.431

Table 5.2.2: Calculated $Q_{\mathrm{Am}}^{\mathrm{Mulliken}}$ in $AmPz_3^{3+}$ using different methods.

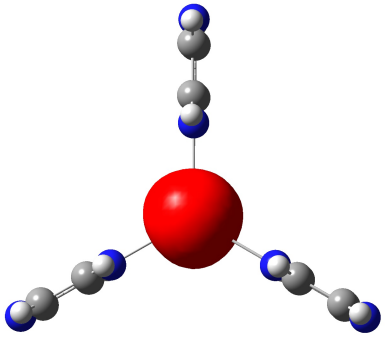

Figure 5.13: The alpha LUMO of $AmPz_3^{3+}$ calculated with the Hartree-Fock method. The isovalue is 0.05.

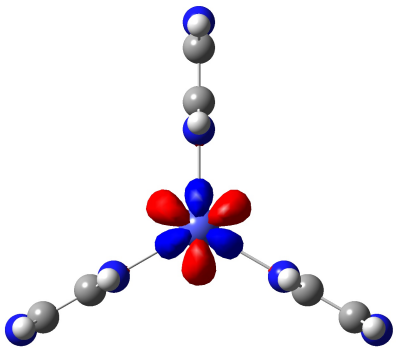

Figure 5.14: The alpha LUMO of $AmPz_3^{3+}$ calculated with the TPSSh functional under PCM(Water). The isovalue is 0.05.

5.3 Actinide compounds with a single azine-based ligand in aqueous solution

In previous sections, I have calculated bond interaction energies and some QTAIM properties of gas-phase actinide complexes with one or three simple ligands, and I have found some patterns and an interesting correspondence between bond interaction energy and the variation of the QTAIM charge on the actinide atoms. However, the SANEX process separates minor actinides from lanthanides *in aqueous solutions*, in which the electronic and geometric structure can differ from those of the gas-phase species. In addition, a few of the molecules calculated here showed problematic geometries in gas-phase optimisations, which may arise due to the absence of solvent effects. However, research has shown that continuum solvation models suffer from larger solvation energy errors for highly charged species,[89, 90, 91] which makes the interaction energies abnormally small (~20kJ/mol) or even negative. In light of this, I have therefore chosen to optimise the geometry in aqueous environment, and calculate the interaction energies and other QTAIM metrics using gas-phase wavefunctions at these geometries.

In this section, I perform such calculations on actinide compounds with a single N-donor ligand. These molecules are optimised with the TPSSh functional and the Stuttgart small-core ECP and basis sets for the actinides and

cc-pVTZ basis sets for other elements, with the inclusion of aqueous environment via PCM. Similar to the previous sections, the molecules are in their triply-charged state. E^3_{int}-type interaction energies of the An-N bonds in these complexes are calculated as Eq. 5.1 where each term reflects a gas-phase single-point calculation; the subsequent QTAIM analyses are also based on the same gas-phase wavefunction at the geometry optimised with solvent effects, as noted above.

The E^3_{int}, bond length and selected QTAIM properties are summarised in Table 5.3.1. It should be noted that many complexes with PyF have unreasonably long bond lengths, which means the corresponding QTAIM properties are also unreliable; therefore, the following discussion is based on the results of complexes with the other three ligands. The average bond length is longer than the result without the inclusion of solvent effect, which also reflects in E^3_{int}, ρ_{BCP}, H_{BCP} and δ. Different from previous results, the AmL^{3+} and PuL^{3+} complexes no longer have bond lengths longer than the other actinides; this is also reflected in E^3_{int}, ρ_{BCP}, H_{BCP} and δ. The delocalisation indices δ are around 0.36 to 0.69, indicating a weaker covalent interaction due to the longer bond length.

The correlation between bond length and ρ_{BCP} is shown in Figure 5.15. All complexes with Py, Pz and Tz are correlated together with $R^2 = 0.830$ in exponential curve fitting. Figure 5.16 shows that there is almost no correlation between the bond interaction energy and ρ_{BCP}. H_{BCP} and δ are also not well correlated with E^3_{int} (R^2 is 0.148 and 0.192, respectively), but ∇^2_{BCP} shows weak correlation with E^3_{int} with R^2=0.348.

The trend in QTAIM charge on the actinide atom, $Q^{\text{QTAIM}}_{\text{An}}$, is very similar to the previous results without solvent effect, indicating that the previous abrupt change in bond length is not related to the QTAIM charge difference of these complexes. As Figure 5.17(a) shows, $Q^{\text{QTAIM}}_{\text{An}}$ follows the same trend as the results from the gas-phase geometries while the trend of bond length is very different; the value of $Q^{\text{QTAIM}}_{\text{An}}$ decreases gradually across the actinide

AnL^{3+}, An={Th-Cm}, L=Py							
E^3_{int}	-698.8	-696.0	-711.5	-766.1	-865.7	-963.8	-810.2
R	2.450	2.562	2.584	2.575	2.519	2.501	2.535
ρ_{BCP}	0.082	0.068	0.061	0.057	0.060	0.060	0.059
$\nabla^2\rho_{BCP}$	0.102	0.075	0.094	0.116	0.141	0.160	0.125
V_{BCP}	-0.076	-0.052	-0.050	-0.050	-0.056	-0.062	-0.054
G_{BCP}	0.051	0.035	0.037	0.039	0.046	0.051	0.043
H_{BCP}	-0.025	-0.017	-0.013	-0.010	-0.011	-0.011	-0.011
δ	0.689	0.661	0.596	0.536	0.507	0.448	0.522
$Q^{\text{QTAIM}}_{\text{An}}$	2.581	2.549	2.438	2.304	2.153	2.021	2.249
AnL^{3+}, An={Th-Cm}, L=PyF							
E^3_{int}	-535.4	-466.9	-552.0	-618.6	-764.6	-892.8	-681.6
R	2.580	4.099	3.088	3.892	2.875	3.054	3.035
ρ_{BCP}	0.060	0.002	0.018	0.003	0.025	0.017	0.019
$\nabla^2\rho_{BCP}$	0.102	0.006	0.048	0.009	0.077	0.053	0.050
V_{BCP}	-0.050	-0.001	-0.011	-0.001	-0.018	-0.011	-0.011
G_{BCP}	0.038	0.001	0.011	0.002	0.019	0.012	0.012
H_{BCP}	-0.012	0.000	0.001	0.000	0.001	0.001	0.001
δ	0.554	0.055	0.235	0.052	0.246	0.162	0.207
$Q^{\text{QTAIM}}_{\text{An}}$	2.645	2.190	2.255	2.043	2.050	1.936	2.120
AnL^{3+}, An={Th-Cm}, L=Pz							
E^3_{int}	-593.6	-618.3	-629.4	-709.8	-818.9	-935.9	-737.8
R	2.451	2.546	2.744	2.579	2.551	2.541	2.576
ρ_{BCP}	0.082	0.068	0.044	0.056	0.055	0.055	0.053
$\nabla^2\rho_{BCP}$	0.099	0.085	0.074	0.121	0.138	0.144	0.121
V_{BCP}	-0.075	-0.054	-0.031	-0.050	-0.051	-0.054	-0.047
G_{BCP}	0.050	0.038	0.025	0.040	0.043	0.045	0.039
H_{BCP}	-0.025	-0.016	-0.006	-0.010	-0.008	-0.009	-0.009
δ	0.639	0.542	0.407	0.461	0.426	0.387	0.430
$Q^{\text{QTAIM}}_{\text{An}}$	2.603	2.467	2.312	2.257	2.108	2.001	2.196
AnL^{3+}, An={Th-Cm}, L=Tz							
E^3_{int}	-548.0	-552.5	-631.5	-629.5	-743.5	-853.2	-674.4
R	2.574	2.470	2.351	2.725	2.569	2.558	2.746
ρ_{BCP}	0.061	0.077	0.089	0.040	0.051	0.051	0.037
$\nabla^2\rho_{BCP}$	0.100	0.107	0.183	0.096	0.140	0.153	0.091
V_{BCP}	-0.050	-0.071	-0.100	-0.031	-0.048	-0.052	-0.028
G_{BCP}	0.038	0.049	0.073	0.028	0.041	0.045	0.026
H_{BCP}	-0.013	-0.022	-0.027	-0.004	-0.006	-0.007	-0.003
δ	0.539	0.637	0.674	0.399	0.430	0.384	0.360
$Q^{\text{QTAIM}}_{\text{An}}$	2.614	2.486	2.434	2.249	2.130	2.000	2.188

Table 5.3.1: The bond interaction energy E^3_{int} (kJ/mol), bond lengths R (Å), the electron density at the BCP ρ_{BCP} (a.u), the Laplacian at the BCP $\nabla^2\rho_{BCP}$ (a.u), the potential energy density V_{BCP} (a.u), the gradient kinetic energy density $G_{BCP}(a.u)$, the total energy of the BCP H_{BCP} (a.u), the delocalisation index δ (a.u), and the QTAIM partial charge on the actinide atom $Q^{\text{QTAIM}}_{\text{An}}$ (a.u) of actinide complexes with single L-type ligands in aqueous environment.

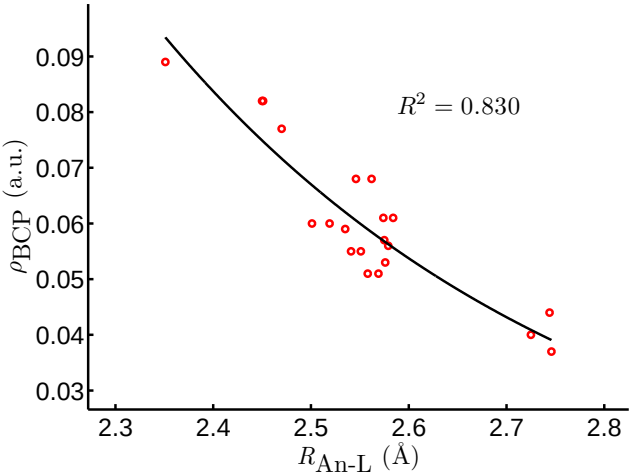

Figure 5.15: ρ_{BCP} against averaged bond length in actinide complexes with single L-type ligand optimised with PCM. The R^2 value corresponds to exponential fitting: $\rho_{BCP} = 19.87\exp(-2.289R) + 0.0021$.

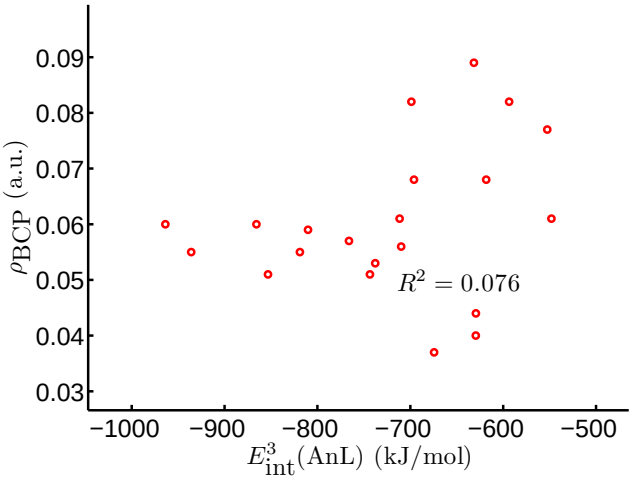

Figure 5.16: ρ_{BCP} against E^3_{int} in actinide complexes with single L-type ligand optimised with PCM. The R^2 value corresponds to linear fitting.

series, to the lowest value at AmL^{3+}, then increases at CmL^{3+}. The lowest value is 2.021 in $AmPy^{3+}$, 2.001 in $AmPz^{3+}$ and 2.000 in $AmTz^{3+}$, which suggests the americium atom is in its Am(II) state, just like in previous sections. This also suggests that the LMCT is not very sensitive to variations in molecular geometry induced by the inclusion of solvent effect. Similar to the results at gas-phase geometries, Figure 5.18 shows good negative correlation between $\left|\Delta Q^{\mathrm{QTAIM}}_{\mathrm{An}}\right|$ and E^3_{int}-type bond interaction energy for complexes with the individual ligands, and all the R^2 values are larger than 0.856. Unlike the actinide

oxides in Section 4.2, different atomic charge analysis schemes lead to similar results. They all show good negative correlation with E^3_{int}; e.g., for $AnPy^{3+}$, the R^2 values are 0.948 for Mulliken charge, 0.940 for Hirshfeld charge and 0.921 for natural charge.

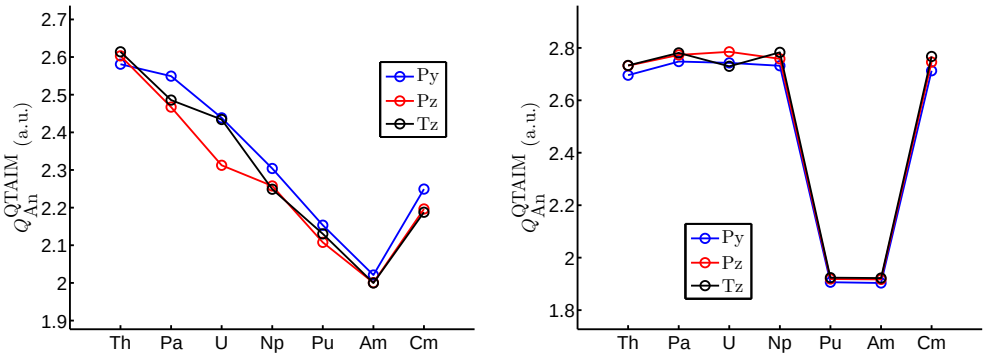

(a) TPSSh (b) Hartree-Fock

Figure 5.17: $Q^{\text{QTAIM}}_{\text{An}}$ in $AnPy^{3+}$ (blue), $AnPz^{3+}$ (red) and $AnTz^{3+}$ (black) using (a) TPSSh and (b) HF.

Apart from $\left|\Delta Q^{\text{QTAIM}}_{\text{An}}\right|$, the charge difference between the An atom and the neighboring nitrogen atom is also well correlated with bond interaction energy for complexes with single ligands. This suggests good correlation between $Q^{\text{QTAIM}}_{\text{An}}$ and $Q^{\text{QTAIM}}_{\text{N}}$, which may arise from the LMCT; as shown in Figure 5.19, all AnL^{3+} except ThL^{3+} show good linear correlation between $Q^{\text{QTAIM}}_{\text{An}}$ and $Q^{\text{QTAIM}}_{\text{N}}$, which suggests that the bonding nature in ThL^{3+} may be somewhat different.

I have shown that the Hartree-Fock method may give different electronic structures to DFT; hence, I performed a series of single-point Hartree-Fock calculations at the geometry optimised with DFT with the TPSSh functional and solvent effect. Table 5.3.2 summarises the calculated $Q^{\text{QTAIM}}_{\text{An}}$ of the actinide complexes calculated with the DFT/TPSSh and Hartree-Fock methods, which is also shown in Figure 5.17(b). Both methods gives $Q^{\text{QTAIM}}_{\text{An}}$ in almost the same range, but with a very different trend. TPSSh gives gradually decreasing $Q^{\text{QTAIM}}_{\text{An}}$ while Hartree-Fock calculations gives very similar $Q^{\text{QTAIM}}_{\text{An}}$ in ThL^{3+} to NpL^{3+} and CmL^{3+}, with a sudden decrease for PuL^{3+} and AmL^{3+}.

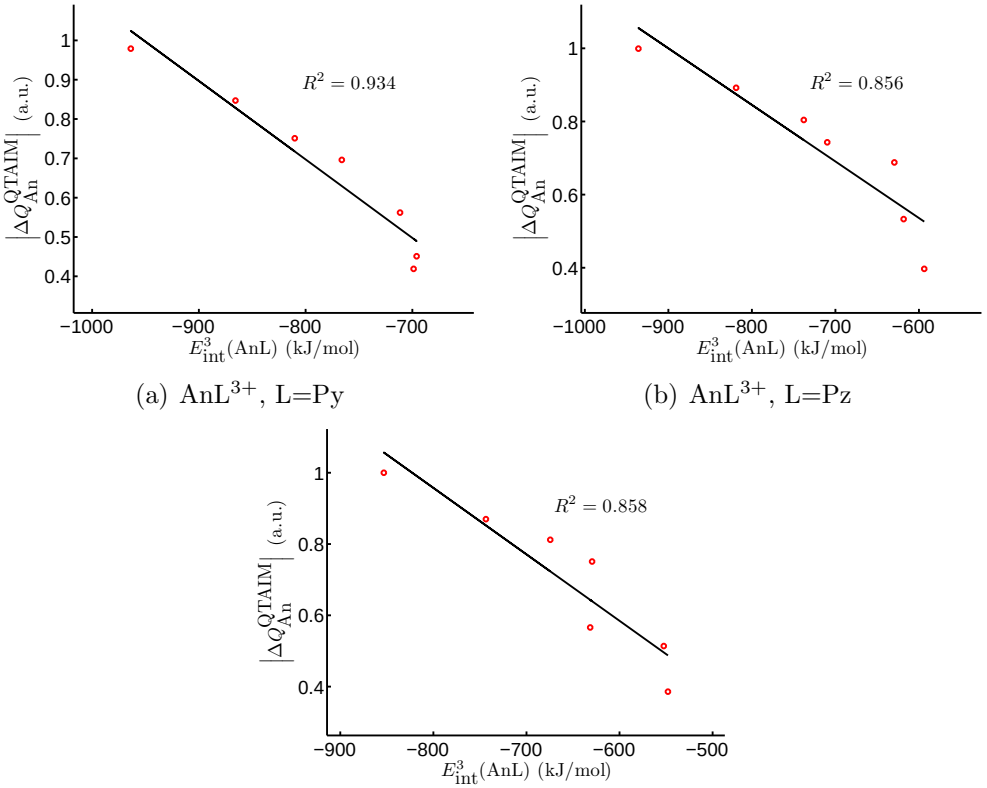

(a) AnL^{3+}, L=Py (b) AnL^{3+}, L=Pz

(c) AnL^{3+}, L=Tz

Figure 5.18: $\left|\Delta Q_{\mathrm{An}}^{\mathrm{QTAIM}}\right|$ against E^3_{int} in complexes of actinides with single ligands. The R^2 values correspond to linear fitting. All data are obtained from TPSSh calculations.

AnL^{3+}, An={Th-Cm}, L=Py							
TPSSh	2.580	2.549	2.438	2.303	2.153	2.020	2.249
HF	2.695	2.747	2.742	2.731	1.906	1.903	2.712
AnL^{3+}, An={Th-Cm}, L=Pz							
TPSSh	2.603	2.466	2.312	2.257	2.107	2.000	2.196
HF	2.731	2.773	2.784	2.758	1.918	1.916	2.745
AnL^{3+}, An={Th-Cm}, L=Tz							
TPSSh	2.613	2.485	2.434	2.248	2.130	1.999	2.187
HF	2.732	2.780	2.729	2.782	1.923	1.922	2.767

Table 5.3.2: Calculated $Q_{\mathrm{An}}^{\mathrm{QTAIM}}$ of actinide complexes with single L-type ligands using different methods.

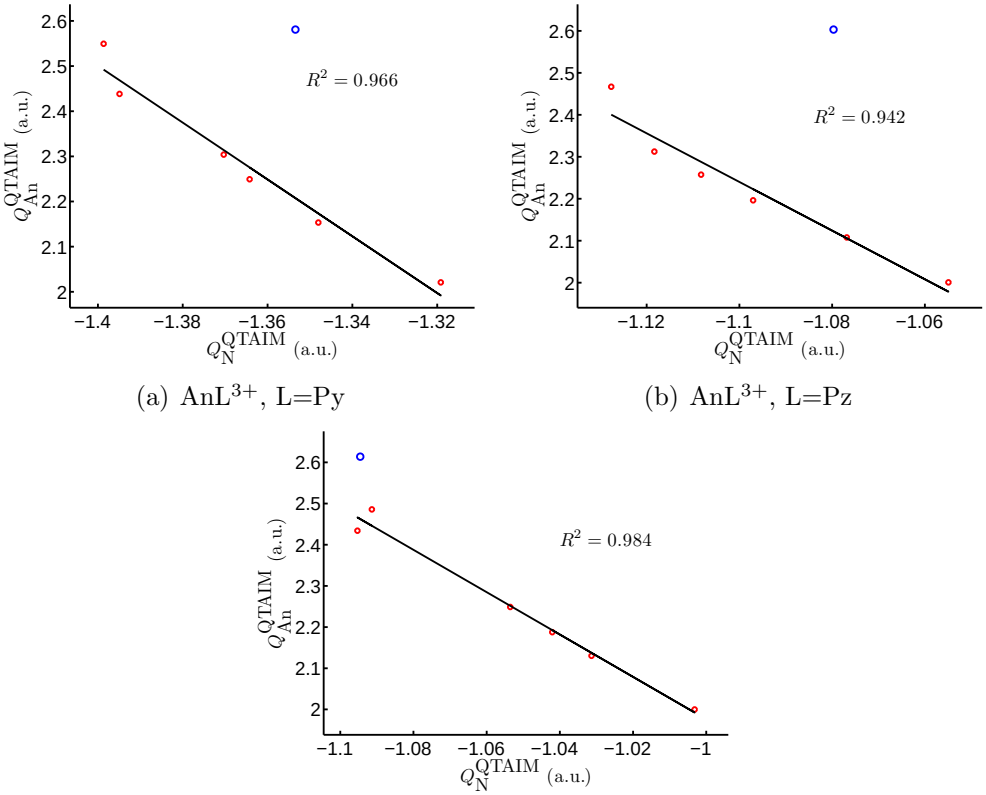

(a) AnL^{3+}, L=Py

(b) AnL^{3+}, L=Pz

(c) AnL^{3+}, L=Tz

Figure 5.19: Q_{An}^{QTAIM} against Q_N^{QTAIM} in complexes of actinides with single ligands. The data from ThL^{3+} complexes are presented as blue circles, and the R^2 values correspond to linear fitting using all other data.

To understand the origin of this difference, the molecular orbitals of these optimised wavefunctions are examined. Figure 5.20 shows the α-spin LUMOs of $AnPy^{3+}$ (An=Th, U, Am) given by the TPSSh and Hartree-Fock wavefunctions. Although TPSSh gives a d orbital and Hartree-Fock gives an s orbital, respectively, the alpha LUMO of $ThPy^{3+}$ is concentrated on the thorium atom in both cases; the pyridine's π bonding orbital is fully occupied in both cases, resulting in the similar Q_{An}^{QTAIM}. However, the situation changes in UPy^{3+}. In the TPSSh wavefunction of UPy^{3+}, the LUMO is composed of both an f-orbital on the uranium atom and the pyridine's π bonding orbital, showing some LMCT character; however, the LUMO of the Hartree-Fock calculation, which is very similar to the LUMO of $ThPy^{3+}$, is concentrated on the uranium atom. The different extent of LMCT explains why TPSSh gives gradually

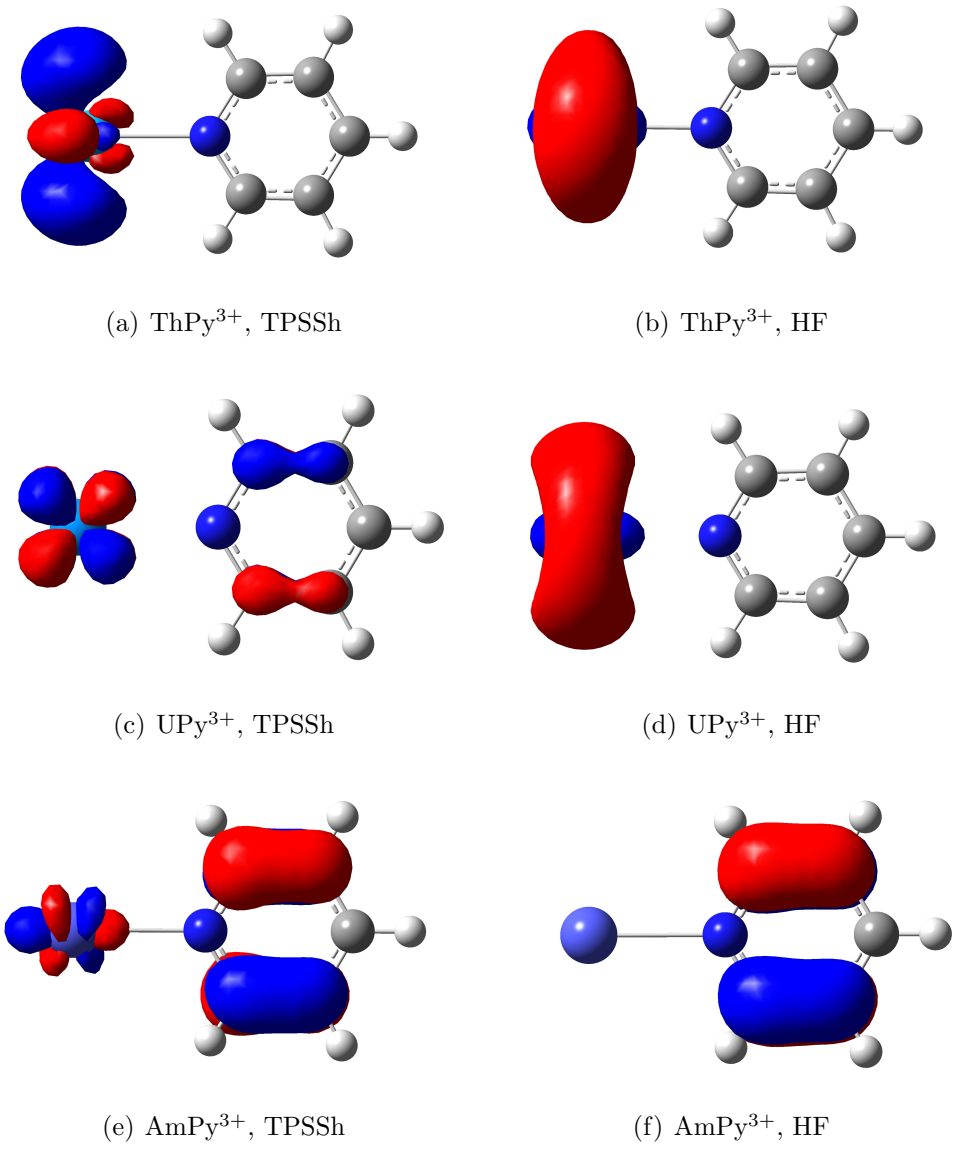

(a) $ThPy^{3+}$, TPSSh (b) $ThPy^{3+}$, HF

(c) UPy^{3+}, TPSSh (d) UPy^{3+}, HF

(e) $AmPy^{3+}$, TPSSh (f) $AmPy^{3+}$, HF

Figure 5.20: The α-spin LUMO of $AnPy^{3+}$ calculated with TPSSh and HF at the geometry optimised with solvent effect. The isovalue is 0.05.

decreasing $Q_{\mathrm{An}}^{\mathrm{QTAIM}}$, but Hartree-Fock gives almost unchanged partial charge. Finally, the LUMO of $AmPy^{3+}$ from both TPSSh and HF is very similar; they are mainly concentrated on the pyridine, with a small amount of f orbital character on the americium atom. Both methods indicate strong LMCT in $AmPy^{3+}$, leading to an Am(II) oxidation state with an $[Rn]5f^7$ configuration.

5.4 Actinide compounds with three azine-based ligands in aqueous solution

I have found an interesting relationship between E_{int}^3 and $\left|\Delta Q_{\mathrm{An}}^{\mathrm{QTAIM}}\right|$ in early actinide complexes at their gas-phase geometry, and this relationship exists in single ligand complexes with the consideration of solvent effects. Therefore, it is natural to analyse the relationship in the PCM-solvated trivalent actinide complexes with three nitrogen-based ligands. These triply charged molecules are also optimised with the TPSSh functional and the Stuttgart small-core ECP and basis sets for the actinides and cc-pVTZ basis sets for other elements, with the inclusion of aqueous environment via PCM. With the geometry optimised with solvent effect, E_{int}^3-type interaction energy of these complexes are calculated with a gas-phase single-point calculation as Eq.5.2. The subsequent QTAIM analyses are also calculated with the gas-phase wavefunction at that geometry. I use C_{3V} symmetrised structures as initial guesses, and the C_3 symmetry is maintained in the optimised structures.

The E_{int}^3, bond length and selected QTAIM properties are summarised in Table 5.4.1. In the previous section, I found unreasonably long bond lengths in some AnPyF compounds, which implies a lack of chemical bond between actinide atom and PyF ligand; since it is shown in the gas-phase calculations in the previous sections that the bond strength in AnL_3 should be even weaker than AnL, I only perform calculations on compounds with the other three L-type ligands, i.e. Py, Pz and Tz. The averaged An-N bond lengths in AnL_3^{3+} are longer than in the single-ligand counterpart; these longer average bond lengths are again reflected in E_{int}^3, ρ_{BCP}, H_{BCP} and δ, which are generally

lower than the corresponding values from single ligand species. It should be noted that the AmL_3^{3+} and PuL_3^{3+} complexes have bond lengths similar to the other AnL_3^{3+} compounds, just like the result from single ligand complexes calculated with PCM. Note that the calculation of $AmTz_3^{3+}$ did not converge, which results in the column of "not available" entries.

AnL_3^{3+}, An={Th-Cm}, L=Py							
E^3_{int}	-517.1	-513.5	-519.6	-534.4	-550.9	-562.7	-552.6
R	2.605	2.651	2.652	2.612	2.590	2.581	2.587
ρ_{BCP}	0.061	0.052	0.051	0.054	0.055	0.052	0.054
$\nabla^2\rho_{BCP}$	0.084	0.104	0.098	0.109	0.113	0.130	0.111
V_{BCP}	-0.047	-0.043	-0.041	-0.046	-0.048	-0.049	-0.047
G_{BCP}	0.034	0.034	0.033	0.037	0.038	0.041	0.038
H_{BCP}	-0.013	-0.008	-0.008	-0.009	-0.010	-0.008	-0.010
δ	0.513	0.449	0.454	0.470	0.481	0.413	0.463
$Q^{\text{QTAIM}}_{\text{An}}$	2.212	2.332	2.302	2.270	2.196	2.006	2.232
AnL_3^{3+}, An={Th-Cm}, L=Pz							
E^3_{int}	-440.9	-438.6	-441.3	-464.9	-490.3	-518.9	-481.5
R	2.619	2.679	2.724	2.638	2.620	2.617	2.626
ρ_{BCP}	0.059	0.049	0.045	0.050	0.050	0.048	0.050
$\nabla^2\rho_{BCP}$	0.081	0.090	0.082	0.107	0.120	0.125	0.105
V_{BCP}	-0.045	-0.038	-0.033	-0.042	-0.044	-0.044	-0.042
G_{BCP}	0.033	0.030	0.027	0.034	0.037	0.038	0.034
H_{BCP}	-0.012	-0.007	-0.006	-0.008	-0.007	-0.006	-0.008
δ	0.486	0.431	0.416	0.433	0.399	0.364	0.417
$Q^{\text{QTAIM}}_{\text{An}}$	2.230	2.336	2.286	2.204	2.026	1.852	2.157
AnL_3^{3+}, An={Th-Cm}, L=Tz							
E^3_{int}	-390.3	-388.8	-389.7	-411.3	-434.2	N/A	-431.5
R	2.691	2.753	2.783	2.704	2.648	N/A	2.672
ρ_{BCP}	0.051	0.043	0.040	0.044	0.048	N/A	0.044
$\nabla^2\rho_{BCP}$	0.077	0.083	0.072	0.094	0.100	N/A	0.100
V_{BCP}	-0.036	-0.031	-0.028	-0.035	-0.039	N/A	-0.036
G_{BCP}	0.028	0.026	0.023	0.029	0.032	N/A	0.031
H_{BCP}	-0.009	-0.005	-0.005	-0.006	-0.007	N/A	-0.006
δ	0.449	0.410	0.405	0.410	0.432	N/A	0.394
$Q^{\text{QTAIM}}_{\text{An}}$	2.296	2.357	2.322	2.226	2.148	N/A	2.153

Table 5.4.1: The bond interaction energy E^3_{int} (kJ/mol), bond lengths R (Å), the electron density at the BCP ρ_{BCP} (a.u), the Laplacian at the BCP $\nabla^2\rho_{BCP}$ (a.u), the potential energy density V_{BCP} (a.u), the gradient kinetic energy density $G_{BCP}(a.u)$, the total energy of the BCP H_{BCP} (a.u), the delocalisation index δ (a.u), and the QTAIM partial charge on the actinide atom $Q^{\text{QTAIM}}_{\text{An}}$ (a.u) of actinide complexes with three L-type ligands in aqueous environment. N/A = not available.

With $R^2 = 0.628$ in exponential curve fitting, the correlation between bond length and ρ_{BCP} in all three-ligands compounds with Py, Pz and Tz is shown in Figure 5.21. Figure 5.22 shows that there is poor correlation between the bond interaction energy and ρ_{BCP} with $R^2 = 0.388$; based on the calculations in previous sections, it may even be that this correlation is accidental. Likewise, H_{BCP} and δ are also not well correlated with E^3_{int} (R^2 is 0.265 and 0.104, respectively), but ∇^2_{BCP} shows medium correlation with R^2 = 0.568.

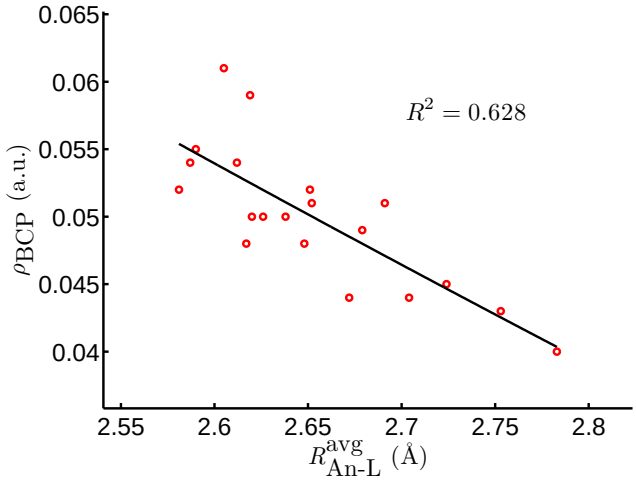

Figure 5.21: ρ_{BCP} against averaged bond length in actinide complexes with three L-type ligands optimised with PCM. The R^2 value corresponds to exponential fitting: $\rho_{BCP} = 0.577\exp(-0.258R) - 0.2409$.

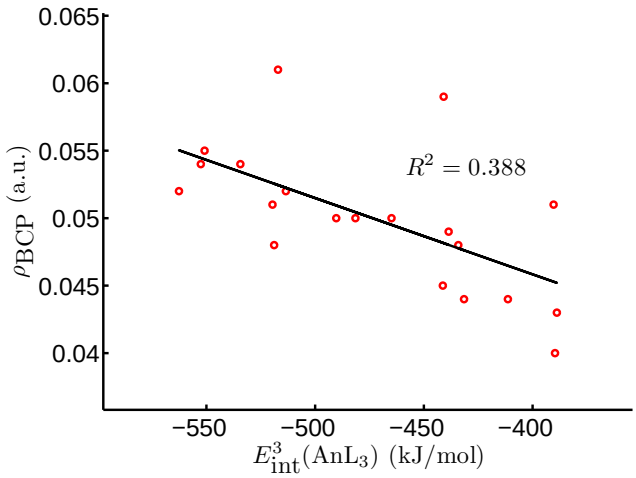

Figure 5.22: ρ_{BCP} against E^3_{int} in actinide complexes with three L-type ligands optimised with PCM. The R^2 value corresponds to linear fitting.

The trend of QTAIM charges is similar to the previous results without solvent effect except for ThL_3^{3+}. As Figure 5.23 shows, while Q_{An}^{QTAIM} decreases gradually across the actinide series, to the lowest value at AmL_3^{3+}, then increases at CmL_3^{3+}, the Q_{An}^{QTAIM} of ThL_3^{3+} is lower than neighboring PaL_3^{3+}. The charges in AnL_3^{3+} are generally lower than AnL^{3+} in the early actinides (Th-U) by more than 0.1; by contrast, for Np to Cm, Q_{An}^{QTAIM} of AnL_3^{3+} are very close to the charge in AnL^{3+}, except for $AmPz_3^{3+}$. Figure 5.24 shows good negative correlation between $\left|\Delta Q_{An}^{QTAIM}\right|$ and E_{int}^3-type bond interaction energy for complexes with the individual ligands, and the R^2 values are very high for L = Pz and Tz, but less so for L= Py.

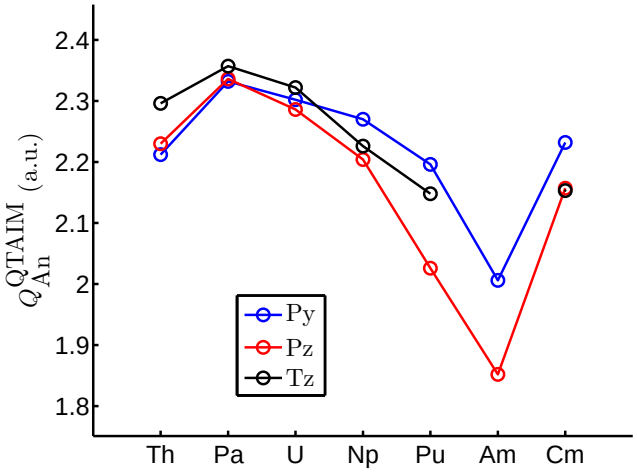

Figure 5.23: Q_{An}^{QTAIM} in $AnPy_3^{3+}$ (blue), $AnPz_3^{3+}$ (red) and $AnTz_3^{3+}$ (black) using different methods.

I have shown, in previous sections, strong LMCT in americium compounds, which leads to an electronic configuration close to Am(II). As Figure 5.25 shows, the alpha LUMO of $AmPy_3^{3+}$ has substantial contribution from the pyridines' π orbital, which again confirms the LMCT; moreover, the occupation number of $5f$ orbital in the americium atom is 6.5 in natural population analysis, which again shows the tendency toward the Am(II) oxidation state discussed in the previous sections.

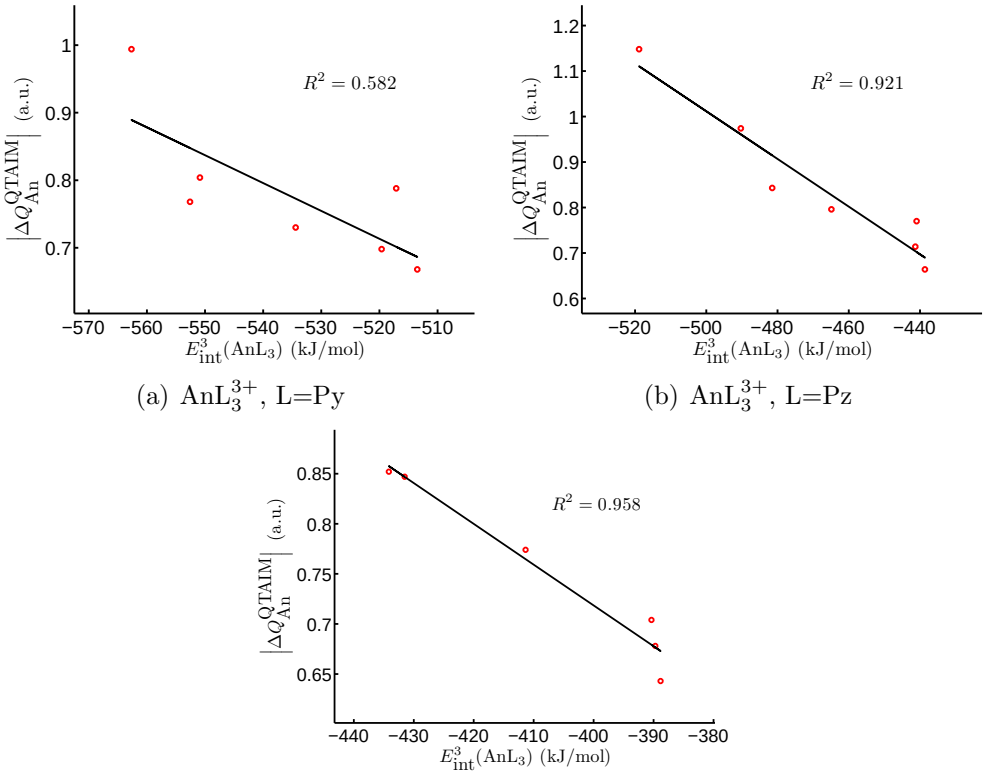

(a) AnL_3^{3+}, L=Py

(b) AnL_3^{3+}, L=Pz

(c) AnL_3^{3+}, L=Tz

Figure 5.24: $\left|\Delta Q_{\mathrm{An}}^{\mathrm{QTAIM}}\right|$ against E^3_{int} in complexes of actinides with three ligands. The R^2 values correspond to linear fitting.

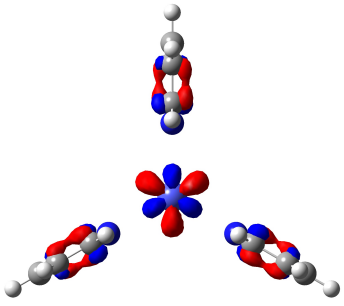

Figure 5.25: The alpha LUMO of $AmPy_3^{3+}$ from gas-phase TPSSh wavefunction. Noted that the geometry is optimised with PCM. The isovalue is 0.05.

5.5 Summary

In summary, although ρ_{BCP}, H_{BCP} and δ do not correlate with bond interaction energy in simple actinide-ligand compounds, I find that the change of the QTAIM partial charge on the actinide atom in the An-N bond formation process correlates with the bond interaction energy rather well. This correlation is valid for actinide compounds with one single N-based ligand and three N-based ligands, with and without the inclusion of solvent effect. Both E^2_{int} and E^3_{int} show very good correlation to $\left|\Delta Q^{\text{QTAIM}}_{\text{An}}\right|$ for actinide compounds containing X-type ligands or L-type ligands.

In all cases, the ρ_{BCP} and the bond lengths in the An-N bonds are well correlated in exponential curve fitting. The low ρ_{BCP} and low δ indicate the low covalency in An-N bonds. The H_{BCP} is all negative with magnitude smaller than actinide oxides. Generally, the An-N bonds in actinide compounds with three N-based ligands have δ smaller than the actinide compounds with a single N-based ligand; in addition, the average An-N bond length of these actinide compounds in aqueous phase is longer than the result without the inclusion of solvent effect, hence the ρ_{BCP}, H_{BCP} and δ are also smaller.

The alpha LUMOs of the americium compounds show significant contribution from the occupied orbital of the ligands, which implies strong LMCT and leads to an Am(II) oxidation state in americium compounds. This effect occurs in other actinide compounds to some extent, and the different extent of LMCT explains why TPSSh gives gradually decreasing $Q^{\text{QTAIM}}_{\text{An}}$ across the actinide series but increases at CmL^{3+}.

Chapter 6

Actinide and Lanthanide Compounds with Polyazine Ligands

6.1 Lanthanum-bisazine complexes and the contribution from single azine components

The target molecules, BTP-like ligands, are constructed with azine donor groups; for example, BTP is a trisazine, and BTBP and BTPhen are tetrakis-azines. It is natural to suppose that these types of ligands should reflect the chemical properties of the individual azine groups in the ligand, at least to some extent. In 2013, de Sahb *et al.* showed that the binding energy of lanthanum-polyazine complexes can be viewed as the sum of the binding energies to individual single azines.[1] They divided a multidentate polyazine ligand into contributions from individual azine groups and bidendate chelating rings, as shown in Figure 6.1.

De Sahb *et al.* analysed the interaction energies of 1:1 La^{3+}-azine complexes. They chose 7 isolated single azines (shown in Figure 6.2), all 28 possible combinations of unique bisazine ligands constructed from these 7 single azines, and several trisazine ligands constructed in the same way. For the single azines, they performed geometry optimisations while constraining the

La^{3+} ion to be positioned along the vector from the centre of the azine to the coordinating nitrogen atom, to mimic the geometry in polyazine complexes. For the bisazines and trisazines, geometry optimisations were performed without constraints. They then calculated the interaction energies of La^{3+} with all these single azines (ΔE_1), bisazines (ΔE_2) and trisazines (ΔE_3), and they found that the interaction energies of La^{3+} to bisazines and trisazines are well correlated with the sum of the corresponding interaction energies of their single azine components, that is, $\Delta E_{2(3)} = k \sum \Delta E_1$, where k is the constant of proportionality.

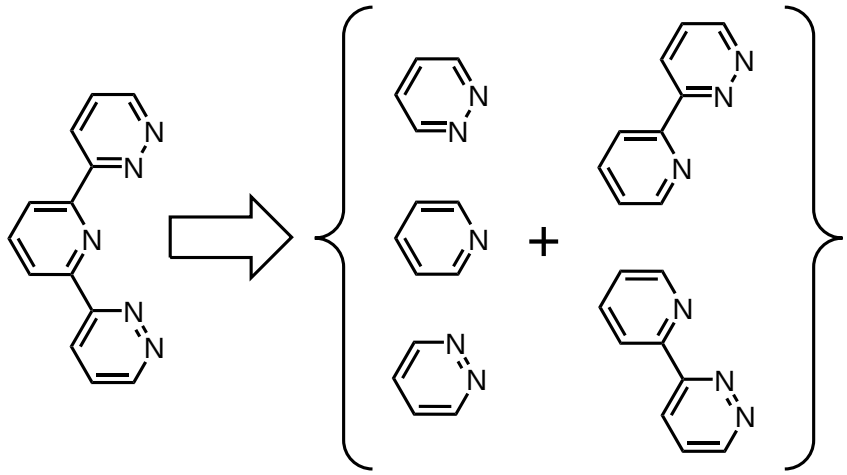

Figure 6.1: Multidentate ligands viewed as collections of individual donor groups and bidentate chelates. Reconstructed from Figure 3 in Reference [1].

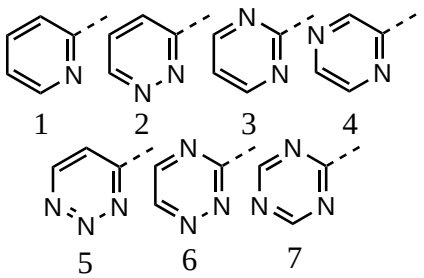

Figure 6.2: The 7 chosen single azine donor groups in Reference [1].

The calculations in their work were computed with the B3LYP functional; they used the LANL2DZ effective core potential basis sets for lanthanum, and 6-31+G* basis set for all carbon, nitrogen and hydrogen atoms. All their cal-

culations were done in gas-phase except for the calculations of reorganisation energies in solvent. In this thesis, I use a different protocol in most of my calculations, hence it is essential to reproduce the correlation before further analysis. In this section, I calculate the 1:1 La^{3+}-ligand complexes with single azine and bisazine ligands, and try to find if the correlations found by de Sahb *et al.* are still valid. These molecules are optimised with the TPSSh functional and the Stuttgart small-core ECP and basis sets for the lanthanum and cc-pVTZ basis sets for other elements, with the inclusion of aqueous environment via PCM. Similar to the previous sections, the molecules are in their triply-charged state. E^3_{int}-type interaction energies of the La-N bonds in these complexes are calculated as Eq. 5.1 where each term reflects a gas-phase single-point calculation at the geometry optimised with solvent effects; the subsequent QTAIM analysis are also based on the same gas-phase wavefunction.

Firstly, I calculated the La^{3+}-single azine complexes. I chose the same 7 single azines (shown in Figure 6.2), performed geometry optimisations with the constraint used by de Sahb *et al.*, that is, to position the La^{3+} ion along the vector from the centre of the azine to the coordinating nitrogen atom. The calculated E^3_{int}, bond length and selected QTAIM properties are summarised in Table 6.1.1. The bond lengths are similar to the actinide-azine complexes in Section 5.3, as are E^3_{int}, ρ_{BCP} and H_{BCP}. The delocalisation indices δ are around 0.40 to 0.58, indicating a weak covalent interaction. For the binding strength, these azines can be ranked in order of their E^3_{int}: **2** > **1** > **6** > **5** > **3** > **4** > **7**, which is different from de Sahb's gas-phase result in the order of **3** and **5**. Note that the notation E^3_{int} of the single azine complexes corresponds to ΔE_1 in de Sahb's article. Here I separate the 7 azines into 3 groups by their binding strength to La^{3+}: **1** and **2** have strong affinity (> −700 kJ/mol); **3**, **4**, **5** and **6** have medium affinity (−700 to −600 kJ/mol); and the last, **7** has weak affinity (< −600 kJ/mol).

For the bisazines complexes, I have calculated all 28 bisazines constructed by all possible combinations of azine pairs using azines **1**-**7**. Bisazines con-

LaL^{3+}, L={**1**-**7**}							
azine	**1**	**2**	**3**	**4**	**5**	**6**	**7**
E^3_{int}	-716.0	-734.6	-638.1	-632.9	-643.9	-655.4	-564.8
R	2.599	2.604	2.737	2.748	2.757	2.744	2.772
ρ_{BCP}	0.058	0.060	0.044	0.043	0.042	0.044	0.039
$\nabla^2\rho_{BCP}$	0.073	0.062	0.063	0.063	0.062	0.060	0.066
V_{BCP}	-0.042	-0.042	-0.027	-0.026	-0.025	-0.027	-0.024
G_{BCP}	0.030	0.029	0.022	0.021	0.021	0.021	0.020
H_{BCP}	-0.012	-0.013	-0.006	-0.005	-0.005	-0.006	-0.004
δ	0.580	0.574	0.453	0.405	0.418	0.432	0.403
$Q^{\text{QTAIM}}_{\text{La}}$	2.426	2.474	2.389	2.359	2.412	2.410	2.383

Table 6.1.1: The bond interaction energy E^3_{int} (kJ/mol), bond lengths R (Å), the electron density at the BCP ρ_{BCP} (a.u), the Laplacian at the BCP $\nabla^2\rho_{BCP}$ (a.u), the potential energy density V_{BCP} (a.u), the gradient kinetic energy density $G_{BCP}(a.u)$, the total energy of the BCP H_{BCP} (a.u), the delocalisation index δ (a.u), and the QTAIM partial charge on the lanthanum atom $Q^{\text{QTAIM}}_{\text{La}}$ (a.u) of La complexes with azines **1**-**7** in aqueous environment.

structed with azines ***x*** and ***y*** are named (***x***-***y***). All computations are performed with the same protocol as the single azine complexes, except for releasing the constraints in the geometry optimisations. However, the geometries of La^{3+}-(**1**-**6**) and La^{3+}-(**2**-**5**) did not fully optimise, hence only the other 26 bisazines are used in the following analysis. The calculated E^3_{int} and the QTAIM partial charge on the lanthanum atom $Q^{\text{QTAIM}}_{\text{La}}$ are summarised in Table 6.1.2. The E^3_{int} of the bisazine complexes correspond to ΔE_2 in de Sahb's article. Although a bisazine has 2 La-N bonds, the E^3_{int} of the bisazine complexes are obviously less than twice E^3_{int} of the single azine complexes (compare Tables 6.1.1 and 6.1.2). The change of the QTAIM partial charge on the lanthanum atoms are very similar to the single azine complexes; the QTAIM partial charge varies only very little as the ligand varies, and Figure 6.3 shows that there is no correlation between E^3_{int} and $\left|\Delta Q^{\text{QTAIM}}_{\text{La}}\right|$. In Chapter 5 I showed that $\left|\Delta Q^{\text{QTAIM}}_{\text{An}}\right|$ is a good indicator of bond strength when the ligand is held constant and the metal is varied. Figure 6.3 shows that this is not true when the metal is held constant and the ligand varies, presumably because the metal charge varies so little.

Bisazine	E^3_{int}	$Q^{\text{QTAIM}}_{\text{La}}$	Bisazine	E^3_{int}	$Q^{\text{QTAIM}}_{\text{La}}$
(**1-1**)	-1138.1	2.353	(**3-5**)	-1003.2	2.390
(**1-2**)	-1158.6	2.369	(**3-6**)	-1046.0	2.373
(**1-3**)	-1080.9	2.357	(**3-7**)	-952.2	2.364
(**1-4**)	-1049.5	2.349	(**4-4**)	-970.8	2.351
(**1-5**)	-1076.8	2.394	(**4-5**)	-996.7	2.387
(**1-7**)	-1012.1	2.376	(**4-6**)	-1021.6	2.367
(**2-2**)	-1188.2	2.385	(**4-7**)	-922.0	2.351
(**2-3**)	-1110.7	2.376	(**5-5**)	-996.7	2.431
(**2-4**)	-1079.6	2.371	(**5-6**)	-1021.1	2.414
(**2-6**)	-1108.1	2.390	(**5-7**)	-940.4	2.408
(**2-7**)	-1038.2	2.392	(**6-6**)	-1056.4	2.390
(**3-3**)	-1033.6	2.355	(**6-7**)	-967.6	2.391
(**3-4**)	-1003.0	2.345	(**7-7**)	-852.7	2.353

Table 6.1.2: The bond interaction energy E^3_{int} (kJ/mol), and the QTAIM partial charge on the lanthanum atom $Q^{\text{QTAIM}}_{\text{La}}$ (a.u) of La^{3+}-bisazine complexes in aqueous environment.

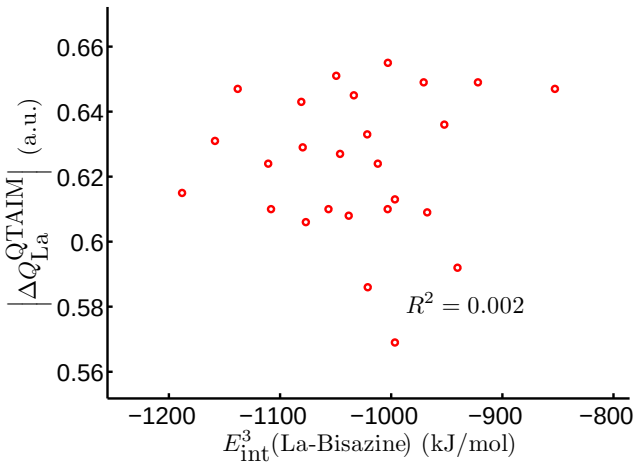

Figure 6.3: $\left|\Delta Q^{\text{QTAIM}}_{\text{La}}\right|$ against E^3_{int} in La^{3+}-bisazine complexes. The R^2 value corresponds to linear fitting.

The strong correlation between the bisazines' interaction energies (ΔE_2) and the sum of corresponding single azines' interaction energies ($\sum \Delta E_1$) is shown in Figure 6.4. The R^2 is 0.964, a bit lower than de Sahb's result ($R^2 = 0.984$). The points in Figure 6.4 can be separated into 5 groups; the leftmost points, which correspond to the bisazines constructed only with azines which have strong affinity, **1** and **2**; the rightmost most point, which refers to the bisazine (**7**-**7**), the one constructed with the weakeast azine **7**; likewise, the other 3 groups can be assigned using combinations of the three groups of azines.

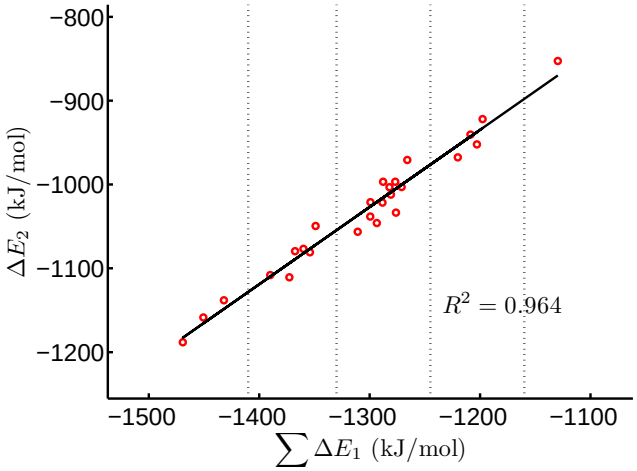

Figure 6.4: ΔE_2 against $\sum \Delta E_1$ in La^{3+}-bisazine complexes. Note that ΔE_2 corresponds to the bisazines' E^3_{int}, and ΔE_1 stands for the corresponding single azines' E^3_{int} (data from Tables 6.1.1 and 6.1.2). The R^2 value corresponds to linear fitting. The dotted lines separate these points into 5 groups by the binding strength of the corresponding single azine components.

Figure 6.4 shows that $\sum \Delta E_1$ is a good indicator of the binding strength of the bisazines; the interaction energy of a bisazine can be divided into contributions of corresponding azines. If we choose a bisazine constructed from two of the same azines, the interaction energies can be divided equally into the contributions of the 2 azines; in other words, E^3_{int} of this bisazine is twice the contribution of the corresponding azine, which can be viewed as a new indicator $\Delta E_1'$. Hence, for an azine $\boldsymbol{x}$, $\Delta E_1'$ *is defined as half the* E^3_{int} *of the bisazine (*$\boldsymbol{x}$-$\boldsymbol{x}$*)*. The concept of $\Delta E_1'$ is shown schematically in Figure 6.5. Figure 6.6

shows the excellent correlation between ΔE_2 and this new indicator $\Delta E_1'$. R^2 is 0.990, which is even higher than the correlation with ΔE_1 ($R^2 = 0.964$ from my data, and 0.984 in de Sahb's article).

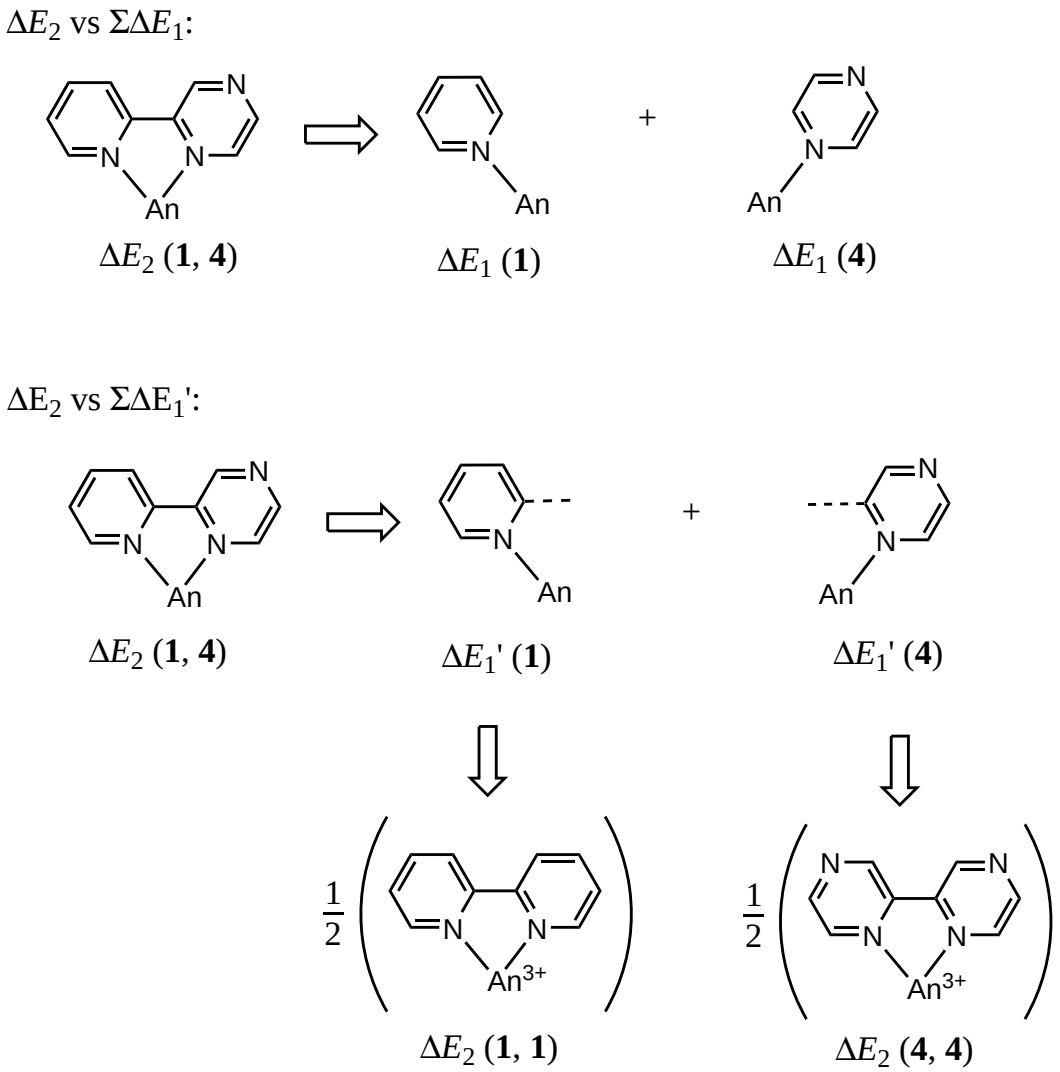

Figure 6.5: Schematic diagram of the relation among ΔE_2, ΔE_1 and the new indicator $\Delta E_1'$. Note that ΔE_2 corresponds to the bisazines' E_{int}^3, ΔE_1 stands for the corresponding single azines' E_{int}^3, and $\Delta E_1'$ stands for half the E_{int}^3 of the bisazine constructed from two of the same azines.

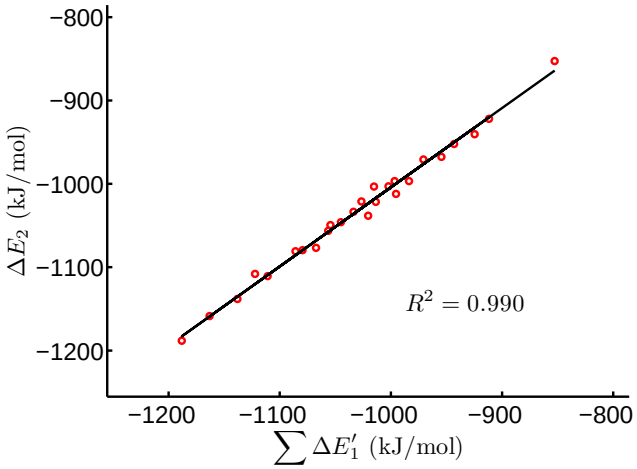

Figure 6.6: ΔE_2 against $\sum \Delta E_1'$ in La^{3+}-bisazine complexes. Note that ΔE_2 corresponds to the bisazines' E_{int}^3, and $\Delta E_1'$ stands for half the E_{int}^3 of the bisazine constructed from two of the same azines (data from Table 6.1.2). The R^2 value corresponds to linear fitting.

6.2 Actinide-bisazine complexes and the contribution from single azine components

In the previous section, I verified the correlation between the interaction energy of La^{3+}-bisazine complexes and their components. The correlation observed by de Sahb et al. was reproduced, and a new indicator $\sum \Delta E_1'$, which reflects the effect of a single azine in a bisazine more accurately, was introduced. However, in its +3 oxidation state La is an f-element without any f-electrons; aiming at the rational design of SANEX ligands, it is neccessary to establish if the correlation is still valid for actinide complexes, especially when the f shell is not empty. I now calculate the 1:1 An^{3+}-ligand complexes (An = Th-Cm) with the same 7 single azine donors and chosen bisazine ligands, to see if the correlation between interaction energy in actinide-bisazine complexes and their single azine components is still valid. All calculations are at same level as the lanthanum complexes in the previous section.

Firstly, I calculate the An^{3+}-single azine complexes. Note that the An^{3+} ion should be constrained on the vector from the centre of the azine to the coordinating nitrogen atom in geometry optimisation, to match the previous approach for La^{3+}. However, although I did not apply this constraint in Sec-

			An^{3+}-**1**, An={Th-Cm}				
E^3_{int}	-698.8	-696.0	-711.5	-766.1	-865.7	-963.8	-810.2
R	2.450	2.562	2.584	2.575	2.519	2.501	2.535
ρ_{BCP}	0.082	0.068	0.061	0.057	0.060	0.060	0.059
$\nabla^2\rho_{BCP}$	0.102	0.075	0.094	0.116	0.141	0.160	0.125
V_{BCP}	-0.076	-0.052	-0.050	-0.050	-0.056	-0.062	-0.054
G_{BCP}	0.051	0.035	0.037	0.039	0.046	0.051	0.043
H_{BCP}	-0.025	-0.017	-0.013	-0.010	-0.011	-0.011	-0.011
δ	0.689	0.661	0.596	0.536	0.507	0.448	0.522
$Q^{\text{QTAIM}}_{\text{An}}$	2.581	2.549	2.438	2.304	2.153	2.021	2.249
			An^{3+}-**2**, An={Th-Cm}				
E^3_{int}	-705.0	-719.4	-721.0	-773.9	-865.2	-967.7	-809.7
R	2.439	2.517	2.597	2.549	2.520	2.513	2.548
ρ_{BCP}	0.084	0.074	0.062	0.064	0.063	0.059	0.060
$\nabla^2\rho_{BCP}$	0.100	0.077	0.078	0.104	0.122	0.136	0.109
V_{BCP}	-0.078	-0.059	-0.048	-0.055	-0.058	-0.057	-0.052
G_{BCP}	0.052	0.039	0.034	0.040	0.044	0.045	0.040
H_{BCP}	-0.027	-0.020	-0.014	-0.014	-0.014	-0.011	-0.012
δ	0.642	0.618	0.574	0.555	0.505	0.441	0.525
$Q^{\text{QTAIM}}_{\text{An}}$	2.603	2.556	2.479	2.378	2.227	2.096	2.309
			An^{3+}-**3**, An={Th-Cm}				
E^3_{int}	-624.8	-629.1	-633.3	-709.7	-813.2	-925.6	-754.8
R	2.461	2.572	2.722	2.572	2.544	2.535	2.560
ρ_{BCP}	0.079	0.065	0.046	0.057	0.056	0.055	0.056
$\nabla^2\rho_{BCP}$	0.103	0.082	0.075	0.119	0.136	0.143	0.121
V_{BCP}	-0.073	-0.050	-0.033	-0.051	-0.052	-0.054	-0.050
G_{BCP}	0.050	0.035	0.026	0.040	0.043	0.045	0.040
H_{BCP}	-0.024	-0.015	-0.007	-0.010	-0.009	-0.009	-0.010
δ	0.663	0.575	0.460	0.503	0.458	0.406	0.475
$Q^{\text{QTAIM}}_{\text{An}}$	2.601	2.495	2.362	2.296	2.143	2.030	2.236
			An^{3+}-**4**, An={Th-Cm}				
E^3_{int}	-593.6	-618.3	-629.4	-709.8	-818.9	-935.9	-737.8
R	2.451	2.546	2.744	2.579	2.551	2.541	2.576
ρ_{BCP}	0.082	0.068	0.044	0.056	0.055	0.055	0.053
$\nabla^2\rho_{BCP}$	0.099	0.085	0.074	0.121	0.138	0.144	0.121
V_{BCP}	-0.075	-0.054	-0.031	-0.050	-0.051	-0.054	-0.047
G_{BCP}	0.050	0.038	0.025	0.040	0.043	0.045	0.039
H_{BCP}	-0.025	-0.016	-0.006	-0.010	-0.008	-0.009	-0.009
δ	0.639	0.542	0.407	0.461	0.426	0.387	0.430
$Q^{\text{QTAIM}}_{\text{An}}$	2.603	2.467	2.312	2.257	2.108	2.001	2.196

			An^{3+}-**5**, An={Th-Cm}				
E^3_{int}	-618.1	-630.9	-626.2	-705.7	-807.9	-911.8	-738.0
R	2.446	2.529	2.771	2.598	2.556	2.552	2.736
ρ_{BCP}	0.081	0.069	0.040	0.053	0.053	0.053	0.038
$\nabla^2\rho_{BCP}$	0.105	0.096	0.080	0.121	0.140	0.151	0.090
V_{BCP}	-0.076	-0.057	-0.028	-0.046	-0.050	-0.053	-0.029
G_{BCP}	0.051	0.041	0.024	0.038	0.042	0.045	0.026
H_{BCP}	-0.025	-0.017	-0.004	-0.008	-0.007	-0.008	-0.003
δ	0.617	0.563	0.415	0.468	0.440	0.381	0.369
$Q^{\text{QTAIM}}_{\text{An}}$	2.628	2.537	2.366	2.308	2.163	2.033	2.216
			An^{3+}-**6**, An={Th-Cm}				
E^3_{int}	-624.7	-643.7	-639.8	-715.9	-819.9	-933.1	-751.5
R	2.445	2.522	2.747	2.585	2.553	2.546	2.697
ρ_{BCP}	0.082	0.072	0.044	0.056	0.057	0.054	0.042
$\nabla^2\rho_{BCP}$	0.102	0.084	0.070	0.112	0.128	0.140	0.091
V_{BCP}	-0.077	-0.058	-0.030	-0.049	-0.053	-0.052	-0.032
G_{BCP}	0.051	0.040	0.024	0.038	0.042	0.043	0.028
H_{BCP}	-0.026	-0.019	-0.006	-0.010	-0.010	-0.008	-0.005
δ	0.623	0.575	0.430	0.478	0.434	0.381	0.389
$Q^{\text{QTAIM}}_{\text{An}}$	2.626	2.539	2.375	2.319	2.173	2.050	2.223
			An^{3+}-**7**, An={Th-Cm}				
E^3_{int}	-548.0	-552.5	-631.5	-629.5	-743.4	-853.2	-674.4
R	2.574	2.470	2.351	2.725	2.568	2.558	2.746
ρ_{BCP}	0.061	0.077	0.089	0.040	0.051	0.051	0.037
$\nabla^2\rho_{BCP}$	0.100	0.107	0.183	0.096	0.140	0.153	0.091
V_{BCP}	-0.050	-0.071	-0.100	-0.031	-0.048	-0.052	-0.028
G_{BCP}	0.038	0.049	0.073	0.028	0.041	0.045	0.026
H_{BCP}	-0.013	-0.022	-0.027	-0.004	-0.006	-0.007	-0.003
δ	0.539	0.637	0.674	0.399	0.430	0.384	0.360
$Q^{\text{QTAIM}}_{\text{An}}$	2.614	2.486	2.434	2.249	2.130	2.000	2.188

Table 6.2.1: The bond interaction energy E^3_{int} (kJ/mol), bond lengths R (Å), the electron density at the BCP ρ_{BCP} (a.u), the Laplacian at the BCP $\nabla^2\rho_{BCP}$ (a.u), the potential energy density V_{BCP} (a.u), the gradient kinetic energy density $G_{BCP}(a.u)$, the total energy of the BCP H_{BCP} (a.u), the delocalisation index δ (a.u), and the QTAIM partial charge on the actinide atom $Q^{\text{QTAIM}}_{\text{An}}$ (a.u) of actinide complexes with **1**-**7** in aqueous environment.

tion 5.3, most of the optimised geometries in those calculations already satisfied the constraint; the angle of deviation of the actinide-nitrogen bond to the vector from the centre of the azine to the coordinating nitrogen atom are all very small (less than 0.1 degree), except for PuTz (0.33 degree). Hence, the results in Section 5.3 except those from PuTz are used here. All other complexes with azines **2**, **3**, **5** ,**6**, and PuTz are then calculated with the same method as in the previous section of La-azine complexes.

The calculated E^3_{int}, bond length and selected QTAIM properties are summarised in Table 6.2.1. Although the complexes with azines **1**, **4** and **7** (except Pu-**7**) are already listed in Table 5.3.1, the results are also given here for convenience. The results are quite similar as the ligands vary; all ρ_{BCP} range from 0.037 to 0.089, and the delocalisation indices δ from 0.36 to 0.69, both indicating weak covalency for these complexes. The correlation between bond length and ρ_{BCP} is shown in Figure 6.7. All complexes with the 7 azines are correlated together with $R^2 = 0.826$ in exponential curve fitting. Figure 6.8 shows that there is almost no correlation between the bond interaction energy and ρ_{BCP}. H_{BCP} and δ are also not well correlated with E^3_{int} (R^2 is 0.141 and 0.246, respectively), but ∇^2_{BCP} shows some correlation with E^3_{int} with R^2=0.428.

Figure 6.9(a) shows the E^3_{int} in An-single azines. The staircase structure indicates that most of the complexes fall into one of the 3 groups defined in Section 6.1: **1** and **2** have strong affinity, **3**, **4**, **5** and **6** have medium affinity, and **7** has weak affinity. An exception occurs for U^{3+}-**7**, which has medium affinity, slightly higher than U^{3+}-**4** and U^{3+}-**5**.

The trend of QTAIM charge on the actinide atom, $Q^{\text{QTAIM}}_{\text{An}}$, is very similar to the previous results in Chapter 5, indicating that the trend of $Q^{\text{QTAIM}}_{\text{An}}$ is largely independent of ligand. As Figure 6.10(a) shows, $Q^{\text{QTAIM}}_{\text{An}}$ follows the same trend with different azines; the value decreases gradually across the actinide series, to the lowest value at the Am^{3+}-azines, then increases to the Cm^{3+}-azines. The lowest values occur for Am^{3+}-azines, ranging from 2.000 (Am^{3+}-**7**) to 2.090 (Am^{3+}-**2**), which again suggests the Am(II) state. Similar to

the results of complexes containing azines **1**, **4** and **7** in Section 5.3, Figure 6.11 shows good negative correlation between $\left|\Delta Q_{\mathrm{An}}^{\mathrm{QTAIM}}\right|$ and E_{int}^{3} for complexes containing azines **2**, **3**, **5** and **6**; all the R^2 values are larger than 0.834.

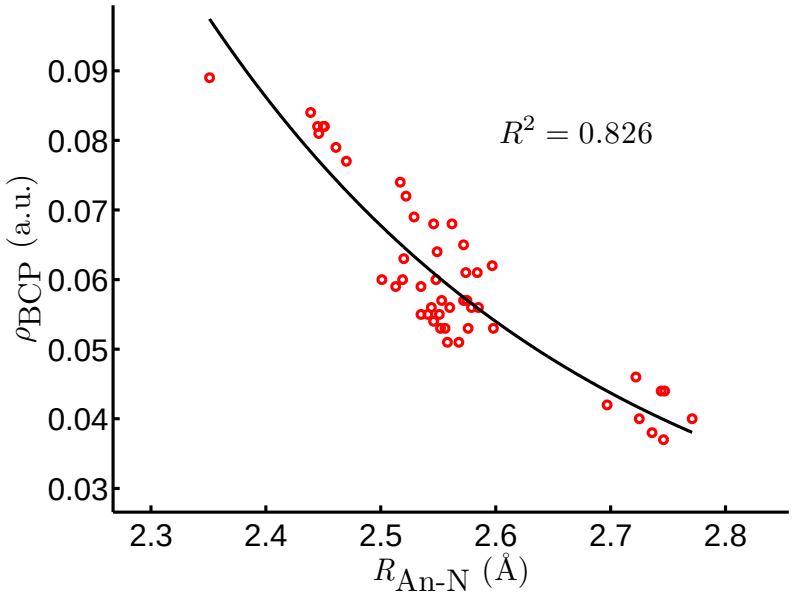

Figure 6.7: ρ_{BCP} against bond length in actinide complexes with single azine ligands. The R^2 value corresponds to exponential fitting: $\rho_{BCP} = 82.367\exp(-2.930R) + 0.0135$.

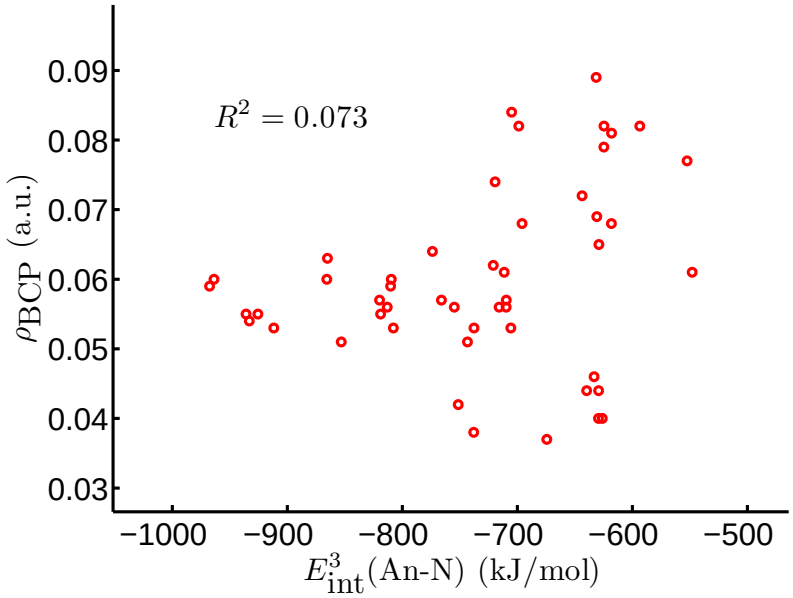

Figure 6.8: ρ_{BCP} against E_{int}^{3} in actinide complexes with single azine ligands. The R^2 value corresponds to linear fitting.

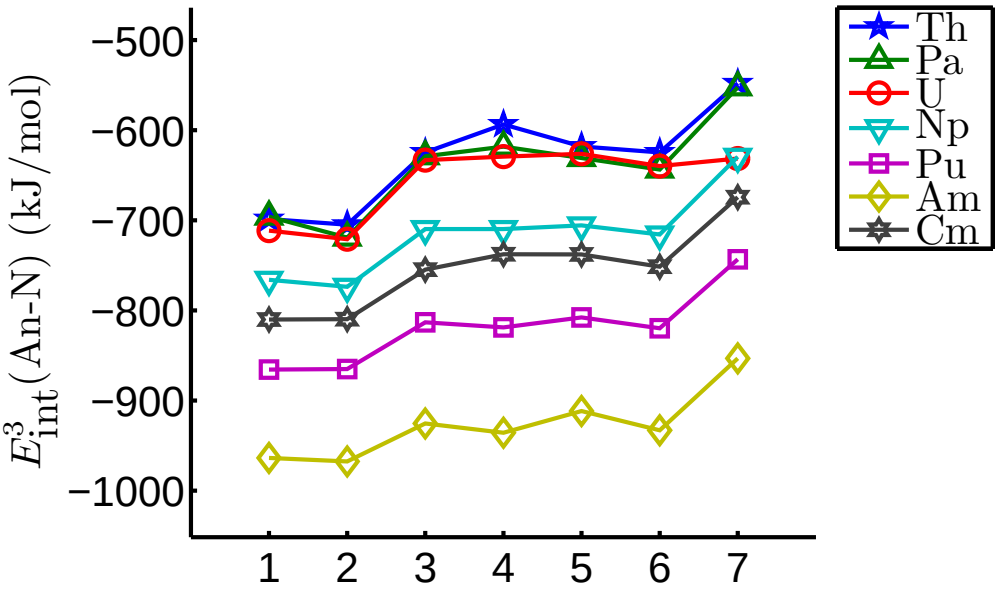

(a) An^{3+}-single azine

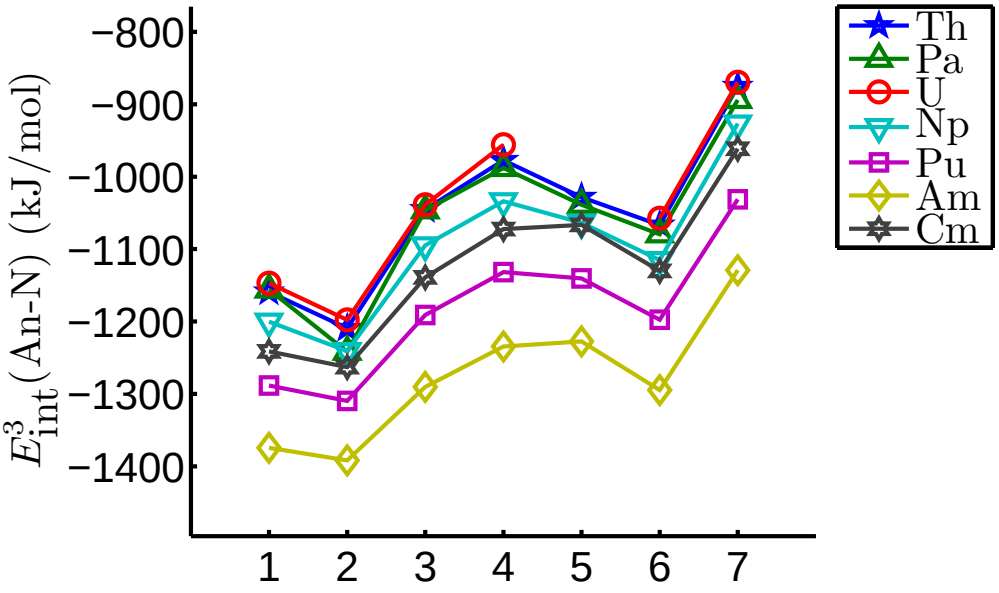

(b) An^{3+}-bisazine

Figure 6.9: E^3_{int} for An-azines, with azines **1-7** in Figure 6.2.

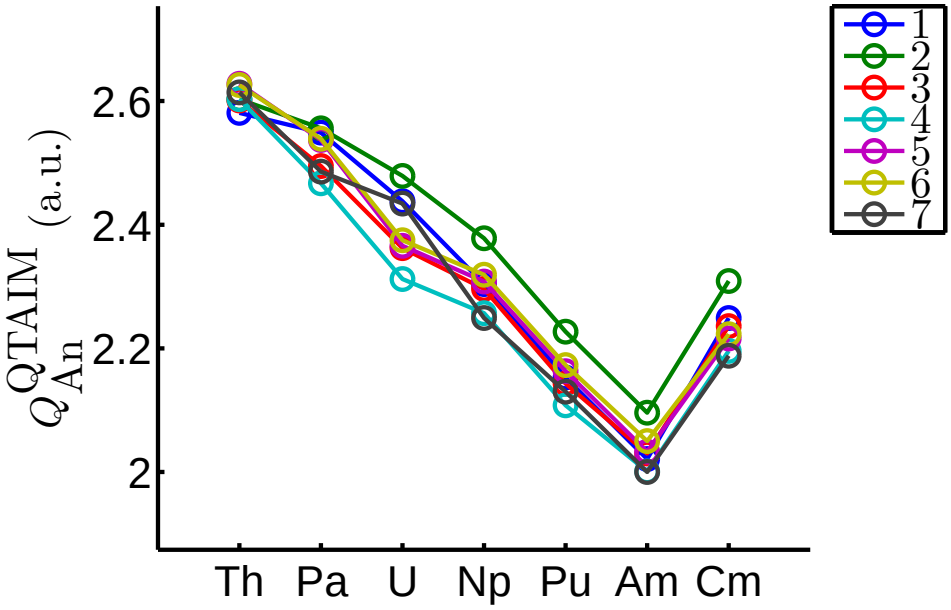

(a) An^{3+}-single azine

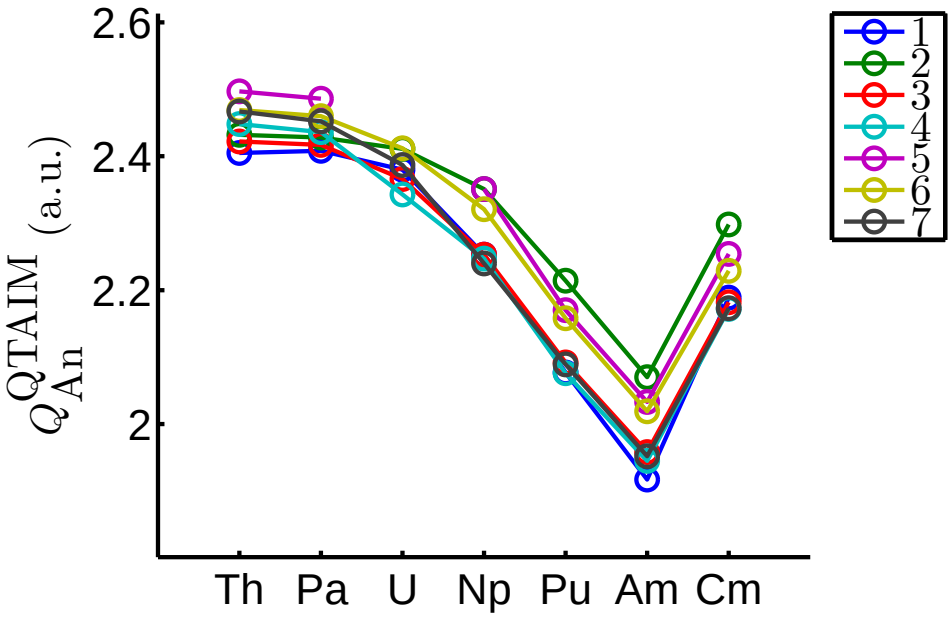

(b) An^{3+}-bisazine

Figure 6.10: Q_{An}^{QTAIM} for An-azines, with azines **1-7** in Figure 6.2.

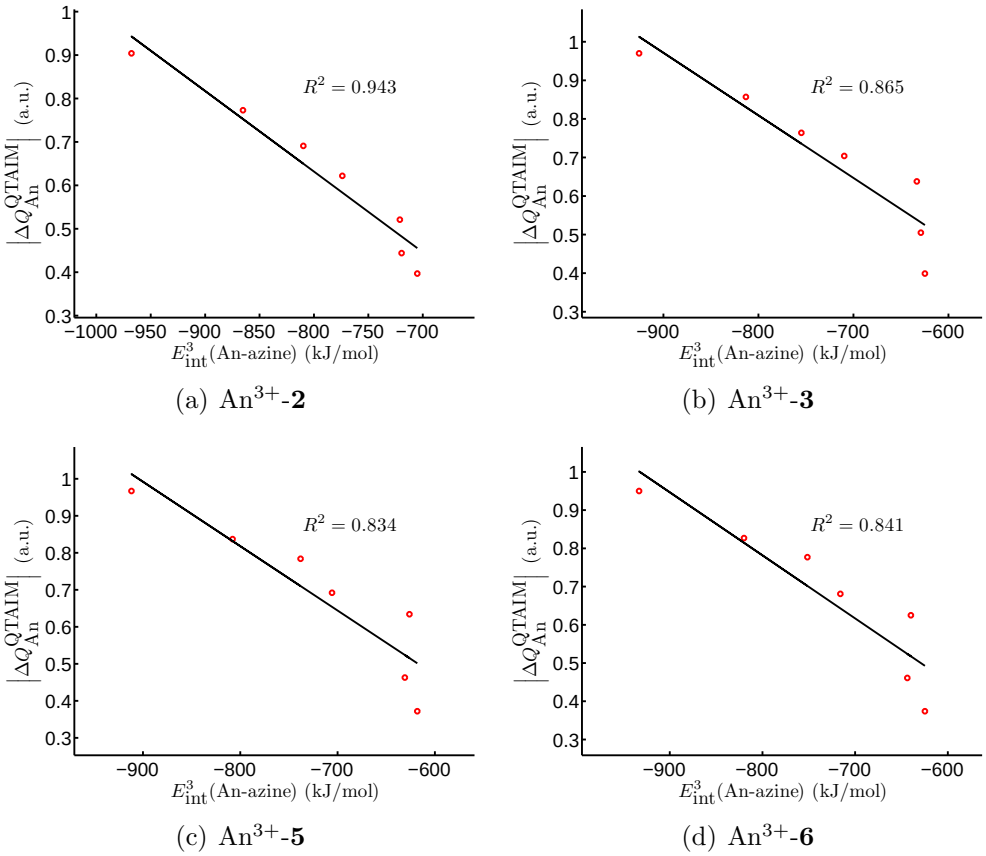

(a) An^{3+}-**2** (b) An^{3+}-**3**

(c) An^{3+}-**5** (d) An^{3+}-**6**

Figure 6.11: $\left|\Delta Q_{\mathrm{An}}^{\mathrm{QTAIM}}\right|$ against E^3_{int} in actinide-single azine complexes. The R^2 values correspond to linear fitting. Note that the results of complexes containing azines **1**, **4** and **7** are shown in Figure 5.18.

For the bisazine complexes, I chose the 7 actinides (Th-Cm) and 7 bisazines constructed with the same single azines since this determines the corresponding $\Delta E_1'$, which leads to 49 combinations of An^{3+}-(***x***-***x***). Geometry optimisations were performed without the constraints of the single azine complexes; however, U^{3+}-(**5**-**5**) did not fully optimise, hence only the other 48 complexes are used in the following analysis. The calculated E^3_{int} and the QTAIM partial charge on the actinide atom are summarised in Table 6.2.2. Note that the interaction energies of actinides to these bisazines correspond to the $\Delta E_1'$ defined in the previous section, which was shown to be a good indicator of the binding strength of La-bisazine complexes.

In comparison to the single azine complexes, the order of the binding strength of these bisazines is even more consistent while varying the metal, as

			An^{3+}-(**1**-**1**), An={Th-Cm}				
E^3_{int}	-1159.1	-1155.9	-1147.0	-1200.3	-1288.4	-1374.5	-1241.3
Q^{QTAIM}_{An}	2.405	2.408	2.380	2.253	2.077	1.917	2.189
			An^{3+}-(**2**-**2**), An={Th-Cm}				
E^3_{int}	-1209.4	-1241.7	-1197.8	-1240.8	-1309.8	-1391.9	-1263.0
Q^{QTAIM}_{An}	2.432	2.428	2.411	2.351	2.214	2.070	2.298
			An^{3+}-(**3**-**3**), An={Th-Cm}				
E^3_{int}	-1045.4	-1046.6	-1038.8	-1094.8	-1191.0	-1290.4	-1139.0
Q^{QTAIM}_{An}	2.422	2.417	2.366	2.253	2.092	1.958	2.182
			An^{3+}-(**4**-**4**), An={Th-Cm}				
E^3_{int}	-977.3	-987.9	-955.8	-1034.0	-1131.9	-1234.5	-1072.2
Q^{QTAIM}_{An}	2.448	2.436	2.343	2.247	2.076	1.945	2.172
			An^{3+}-(**5**-**5**), An={Th-Cm}				
E^3_{int}	-1028.2	-1038.7	N/A	-1063.5	-1140.6	-1227.4	-1066.5
Q^{QTAIM}_{An}	2.497	2.486	N/A	2.351	2.170	2.033	2.254
			An^{3+}-(**6**-**6**), An={Th-Cm}				
E^3_{int}	-1066.8	-1079.6	-1057.3	-1115.2	-1197.6	-1294.8	-1130.2
Q^{QTAIM}_{An}	2.469	2.460	2.412	2.321	2.158	2.019	2.229
			An^{3+}-(**7**-**7**), An={Th-Cm}				
E^3_{int}	-875.2	-894.1	-869.5	-926.7	-1031.2	-1129.2	-961.5
Q^{QTAIM}_{An}	2.467	2.452	2.387	2.240	2.089	1.952	2.173

Table 6.2.2: The bond interaction energy E^3_{int} (kJ/mol), bond lengths R (Å), the electron density at the BCP ρ_{BCP} (a.u), the Laplacian at the BCP $\nabla^2\rho_{BCP}$ (a.u), the potential energy density V_{BCP} (a.u), the gradient kinetic energy density $G_{BCP}(a.u)$, the total energy of the BCP H_{BCP} (a.u), the delocalisation index δ (a.u), and the QTAIM partial charge on the actinide atom Q^{QTAIM}_{An} (a.u) of actinide complexes with selected bisazines in aqueous environment.

shown in Figure 6.9(b). The staircase structure still exists, and shows the 3 groups defined in Section 6.1. However, for the group with medium affinity, **3** and **6** always have stronger affinity than **4** and **5**, which is not the case in the single azine complexes. The original idea from de Sahb et al. was to divide a multidentate polyazine ligand into contributions from individual azine groups; however, it is arguably more reasonable to use $\Delta E'_1$ instead of ΔE_1 to mimic the azine component's contribution to a bisazine's affinity since $\Delta E'_1$ takes the whole bisazine structure into consideration, and hence it is much closer to the situation in BTP-like ligands.

The QTAIM partial charge on the actinide atoms is very similar to the

single azine complexes; we can see from Figure 6.10(b) that $Q_{\mathrm{An}}^{\mathrm{QTAIM}}$ follows the same trend with different bisazines, which is the same as the trend of single azines in Figure 6.10(a). The value of $Q_{\mathrm{An}}^{\mathrm{QTAIM}}$ decreases gradually across the actinide series, to the lowest value at the Am^{3+}-bisazines, then increases at the Cm^{3+}-bisazines. $Q_{\mathrm{An}}^{\mathrm{QTAIM}}$ of the Am^{3+}-bisazines ranges from 1.917 (Am^{3+}-(**1**-**1**)) to 2.070 (Am^{3+}-(**2**-**2**)), which again suggests the Am(II) state. Note that $Q_{\mathrm{An}}^{\mathrm{QTAIM}}$ changes very little between corresponding single azine and bisazine complexes even though the bisazine complexes have two nitrogens coordinating to the actinide atom. Figure 6.12 shows good negative correlation between $\left|\Delta Q_{\mathrm{An}}^{\mathrm{QTAIM}}\right|$ and E_{int}^{3} for all actinide-bisazine complexes; all the R^2 values are larger than 0.881.

Fixing a specific azine						
An-**1**	An-**2**	An-**3**	An-**4**	An-**5**	An-**6**	An-**7**
0.991	0.946	0.994	0.972	0.946	0.980	0.907
Fixing a specific actinide						
Th-***x***	Pa-***x***	U-***x***	Np-***x***	Pu-***x***	Am-***x***	Cm-***x***
0.976	0.975	0.736	0.944	0.921	0.888	0.977

Table 6.2.3: The correlation coefficients R^2 from linear regression of ΔE_2 against $\sum \Delta E_1$ while either fixing a specific azine or a specific actinide.

Figure 6.13 shows the correlation between the actinide interaction energies of bisazines constructed with two of the same azines and their single azine components, which also corresponds to twice $\Delta E_1'$ and ΔE_1, respectively. The 7 colours stand for the 7 different actinides while the 7 shapes stand for the 7 different azines. Table 6.2.3 shows the R^2 values of the correlation between ΔE_2 and $\sum \Delta E_1$ while either fixing a specific azine or a specific actinide. By fixing a specific azine and varying the actinide, 7 sets of points with the same shapes are formed, and all of them show very good correlation (R^2 values range from 0.907 to 0.994). By fixing a specific actinide and varying the azines, 7 sets of points with same colours are formed, and 6 of them also show very good correlation (R^2 values range from 0.888 to 0.977). The only exception is the set corresponding to complexes containing U^{3+}, which has $R^2 = 0.736$. This may be due to the lack of data from U^{3+}-(**5**-**5**) and the unusual medium affinity of

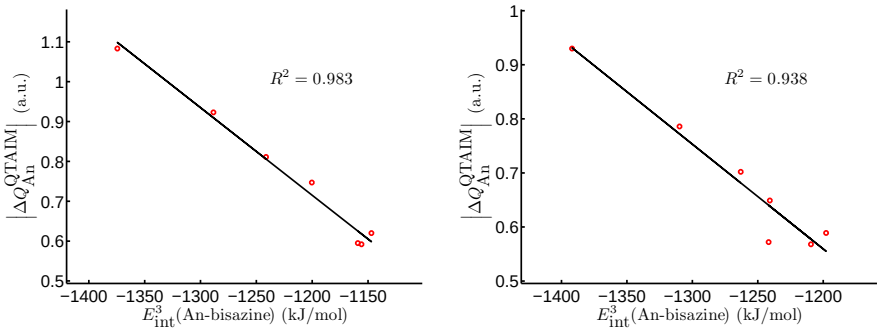

(a) An^{3+}-(**1-1**)

(b) An^{3+}-(**2-2**)

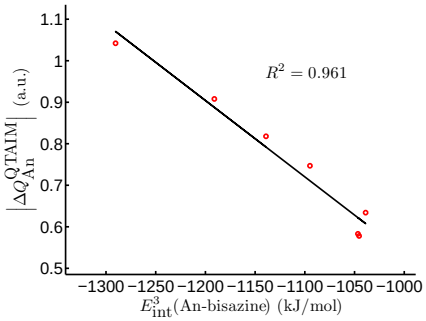

(c) An^{3+}-(**3-3**)

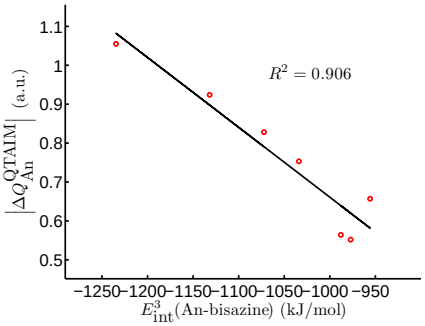

(d) An^{3+}-(**4-4**)

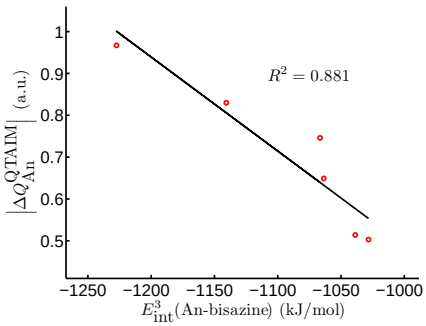

(e) An^{3+}-(**5-5**)

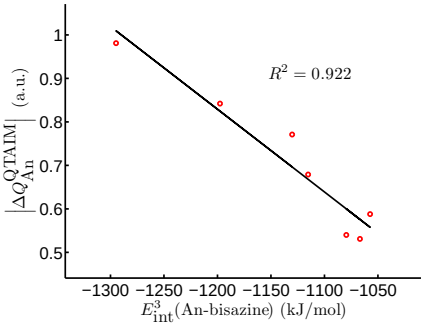

(f) An^{3+}-(**6-6**)

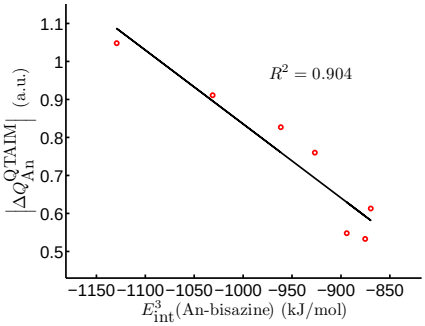

(g) An^{3+}-(**7-7**)

Figure 6.12: $\left|\Delta Q_{\mathrm{An}}^{\mathrm{QTAIM}}\right|$ against E^3_{int} in actinides-bisazine complexes. The R^2 values correspond to linear fitting.

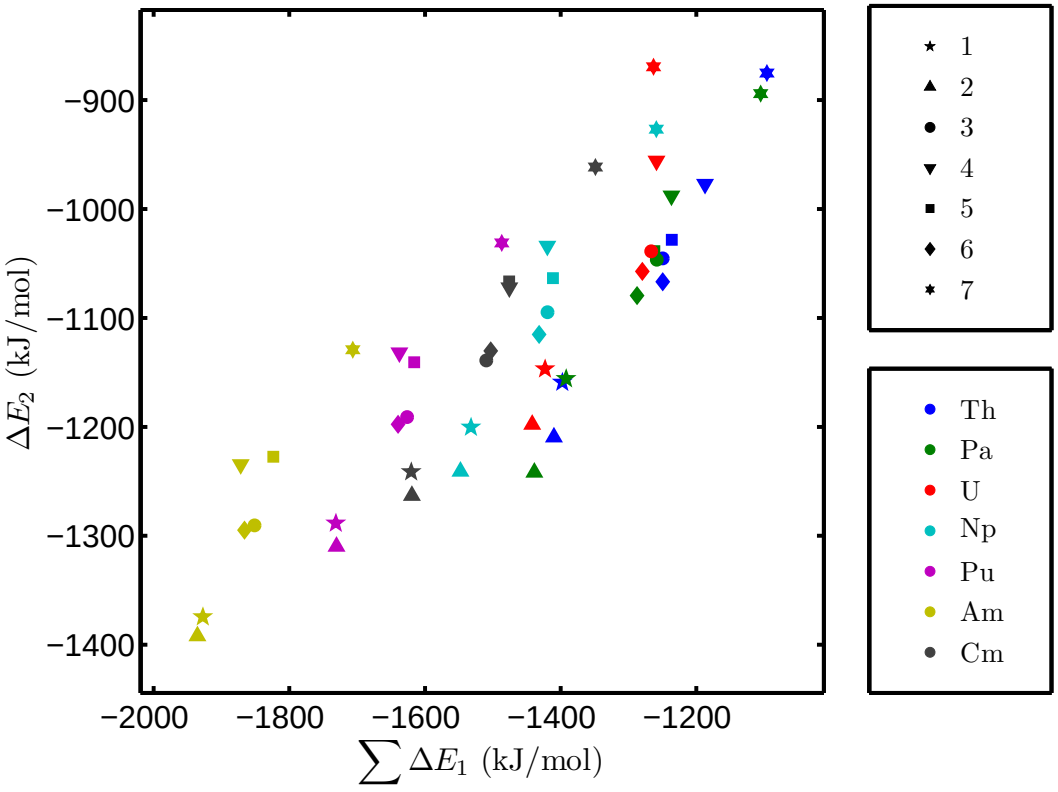

Figure 6.13: ΔE_2 against $\sum \Delta E_1$ in An^{3+}-bisazine complexes. The 7 colours stand for the 7 different actinides while the 7 shapes stand for the 7 different azines. Note that ΔE_2 corresponds to the bisazines' E^3_{int}, and ΔE_1 stands for the corresponding single azines' E^3_{int} (data from Tables 6.2.1 and 6.2.2).

U^{3+}-**7** observed in Figure 6.9(a). Both two ways give good correlations with different slopes, which again shows that the contributions of the individual single azines can predict the interaction energies between actinides and the bisazines; furthermore, this good correlation provides the connection between the two indicators, ΔE_1 and $\Delta E_1'$.

After investigation of the complexes with the selected 7 bisazines, it is natural to extend the analysis to actinide complexes with all 28 possible combinations of bisazines for comparison to the results from the La^{3+}-bisazines in previous section. This has been performed for Th^{3+}, Am^{3+} and Cm^{3+}, to compare an early actinide with La^{3+} and also because BTP-like ligands are aimed at the minor actinides. However, as calculations of Th^{3+}-(**2**-**5**) and Th^{3+}-(**4**-**7**) did not fully optimise, only the other Th complexes are used in the following

Bisazine	E^3_{int}	$Q^{\text{QTAIM}}_{\text{Th}}$	Bisazine	E^3_{int}	$Q^{\text{QTAIM}}_{\text{Th}}$
(**1**-**1**)	-1159.1	2.405	(**3**-**4**)	-1008.8	2.436
(**1**-**2**)	-1192.6	2.410	(**3**-**5**)	-1037.4	2.463
(**1**-**3**)	-1104.3	2.414	(**3**-**6**)	-1067.2	2.436
(**1**-**4**)	-1065.8	2.426	(**3**-**7**)	-963.6	2.442
(**1**-**5**)	-1105.9	2.444	(**4**-**4**)	-977.3	2.448
(**1**-**6**)	-1116.8	2.431	(**4**-**5**)	-1008.0	2.472
(**1**-**7**)	-1028.3	2.431	(**4**-**6**)	-1028.6	2.454
(**2**-**2**)	-1209.4	2.432	(**5**-**5**)	-1028.2	2.497
(**2**-**3**)	-1134.0	2.424	(**5**-**6**)	-1046.9	2.483
(**2**-**4**)	-1107.6	2.430	(**5**-**7**)	-955.5	2.485
(**2**-**6**)	-1135.7	2.451	(**6**-**6**)	-1066.8	2.469
(**2**-**7**)	-1059.9	2.440	(**6**-**7**)	-977.0	2.466
(**3**-**3**)	-1045.4	2.422	(**7**-**7**)	-875.2	2.467

Table 6.2.4: The bond interaction energy E^3_{int} (kJ/mol), and the QTAIM partial charge on the thorium atom $Q^{\text{QTAIM}}_{\text{Th}}$ (a.u) of Th^{3+}-bisazine complexes in aqueous environment.

Bisazine	E^3_{int}	$Q^{\text{QTAIM}}_{\text{Am}}$	Bisazine	E^3_{int}	$Q^{\text{QTAIM}}_{\text{Am}}$
(**1**-**1**)	-1374.5	1.917	(**3**-**4**)	-1263.0	1.953
(**1**-**2**)	-1374.9	2.030	(**3**-**5**)	-1248.0	2.018
(**1**-**3**)	-1318.3	1.963	(**3**-**6**)	-1293.8	1.997
(**1**-**4**)	-1301.1	1.948	(**3**-**7**)	-1209.0	1.960
(**1**-**5**)	-1294.6	2.029	(**4**-**4**)	-1234.5	1.945
(**1**-**6**)	-1327.3	2.029	(**4**-**5**)	-1245.6	1.979
(**1**-**7**)	-1236.0	1.989	(**4**-**6**)	-1279.6	1.974
(**2**-**2**)	-1391.9	2.070	(**4**-**7**)	-1191.6	1.942
(**2**-**3**)	-1323.9	2.043	(**5**-**5**)	-1227.4	2.033
(**2**-**4**)	-1323.0	2.006	(**5**-**6**)	-1256.1	2.031
(**2**-**5**)	-1306.1	2.062	(**5**-**7**)	-1178.0	1.999
(**2**-**6**)	-1336.6	2.050	(**6**-**6**)	-1294.8	2.019
(**2**-**7**)	-1255.2	2.028	(**6**-**7**)	-1211.9	2.000
(**3**-**3**)	-1290.4	1.958	(**7**-**7**)	-1129.2	1.952

Table 6.2.5: The bond interaction energy E^3_{int} (kJ/mol), and the QTAIM partial charge on the americium atom $Q^{\text{QTAIM}}_{\text{Am}}$ (a.u) of Am^{3+}-bisazine complexes in aqueous environment.

Bisazine	E^3_{int}	$Q^{\text{QTAIM}}_{\text{Cm}}$	Bisazine	E^3_{int}	$Q^{\text{QTAIM}}_{\text{Cm}}$
(**1**-**1**)	-1241.3	2.189	(**3**-**4**)	-1106.4	2.175
(**1**-**2**)	-1251.8	2.278	(**3**-**5**)	-1093.4	2.237
(**1**-**3**)	-1185.9	2.213	(**3**-**6**)	-1131.6	2.207
(**1**-**4**)	-1155.6	2.196	(**3**-**7**)	-1054.1	2.185
(**1**-**5**)	-1168.7	2.260	(**4**-**4**)	-1072.2	2.172
(**1**-**6**)	-1197.2	2.262	(**4**-**5**)	-1080.7	2.197
(**1**-**7**)	-1106.0	2.230	(**4**-**6**)	-1113.6	2.186
(**2**-**2**)	-1263.0	2.298	(**4**-**7**)	-1014.1	2.146
(**2**-**3**)	-1191.5	2.275	(**5**-**5**)	-1066.5	2.254
(**2**-**4**)	-1172.0	2.226	(**5**-**6**)	-1090.5	2.243
(**2**-**5**)	-1174.8	2.300	(**5**-**7**)	-1010.0	2.213
(**2**-**6**)	-1199.3	2.288	(**6**-**6**)	-1130.2	2.229
(**2**-**7**)	-1104.7	2.248	(**6**-**7**)	-1048.1	2.211
(**3**-**3**)	-1139.0	2.182	(**7**-**7**)	-961.5	2.173

Table 6.2.6: The bond interaction energy E^3_{int} (kJ/mol), and the QTAIM partial charge on the curium atom $Q^{\text{QTAIM}}_{\text{Cm}}$ (a.u) of Cm^{3+}-bisazine complexes in aqueous environment.

analysis.

The calculated E^3_{int} and the QTAIM partial charge on the actinide atom $Q^{\text{QTAIM}}_{\text{An}}$ are summarised in Table 6.2.4 (Th^{3+}-bisazine), Table 6.2.5 (Am^{3+}-bisazine), and Table 6.2.6 (Cm^{3+}-bisazine). For each actinide, the QTAIM partial charge on the actinide atoms in all complexes containing this actinide only varies slightly; for all Th^{3+}-bisazine complexes, $Q^{\text{QTAIM}}_{\text{Th}}$ ranges from 2.405 to 2.497; for all Am^{3+}-bisazine complexes, $Q^{\text{QTAIM}}_{\text{Am}}$ ranges from 1.917 to 2.070; for all Cm^{3+}-bisazine complexes, $Q^{\text{QTAIM}}_{\text{Cm}}$ ranges from 2.146 to 2.300.

The strong linear correlations between the bisazines' interaction energies (ΔE_2) with the three actinides (Th, Am and Cm) and either (a) $\sum \Delta E_1$, the sum of the corresponding single azines' interaction energies, or (b) $\sum \Delta E_1'$, the sum of the contribution of a single azine in a bisazine constructed from two of the same azines, are shown in Figure 6.14 (Th^{3+}-bisazine), Figure 6.15 (Am^{3+}-bisazine) and Figure 6.16 (Cm^{3+}-bisazine); the R^2 values in all six cases are larger than 0.915. This verifies the correlation between the interaction energies of these An^{3+}-bisazine complexes and their components, with both $\sum \Delta E_1$ or the new indicator $\sum \Delta E_1'$. In comparison with $\sum \Delta E_1$, it is obvious that

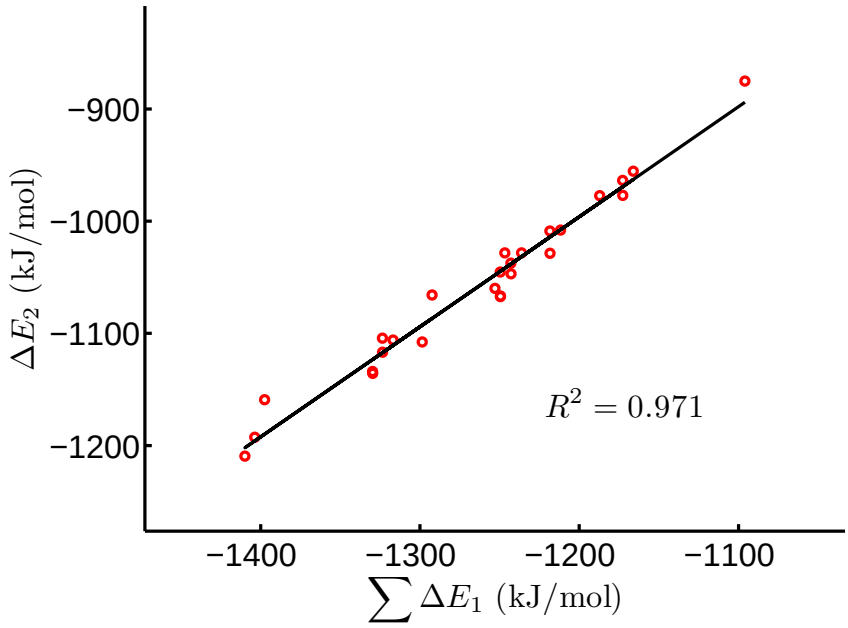

(a) ΔE_2 v.s. $\sum \Delta E_1$

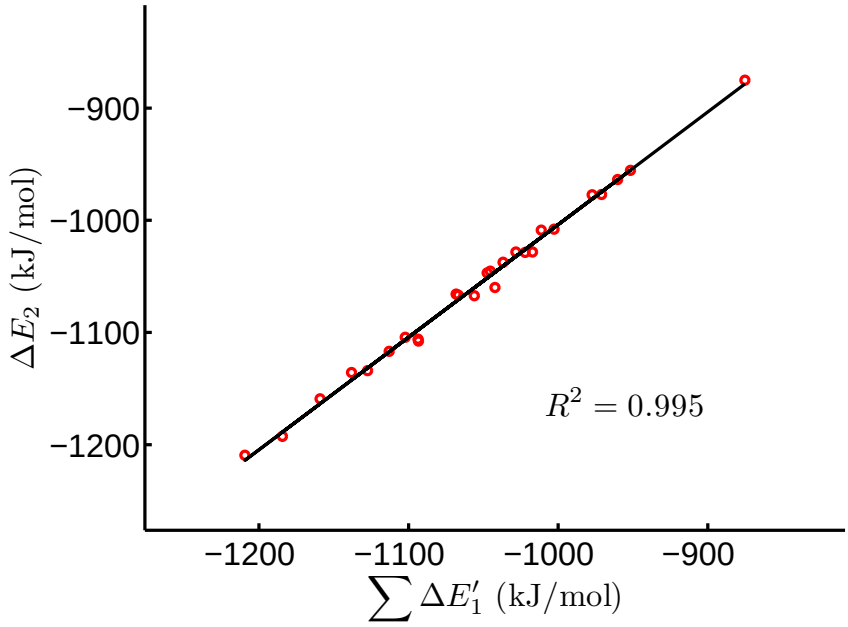

(b) ΔE_2 v.s. $\sum \Delta E_1'$

Figure 6.14: ΔE_2 against (a) $\sum \Delta E_1$ and (b) $\sum \Delta E_1'$ in Th^{3+}-bisazine complexes. The R^2 values correspond to linear fitting. Note that ΔE_2 corresponds to the bisazines' E_{int}^3, ΔE_1 stands for the corresponding single azines' E_{int}^3, and $\Delta E_1'$ stands for half the E_{int}^3 of the bisazine constructed from two of the same azines (data from Tables 6.2.1 and 6.2.4).

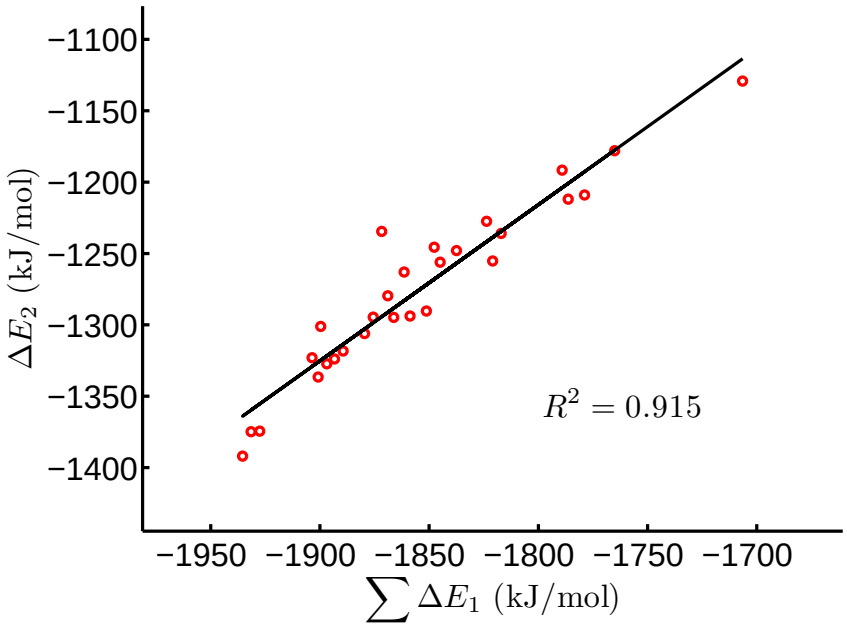

(a) ΔE_2 v.s. $\sum \Delta E_1$

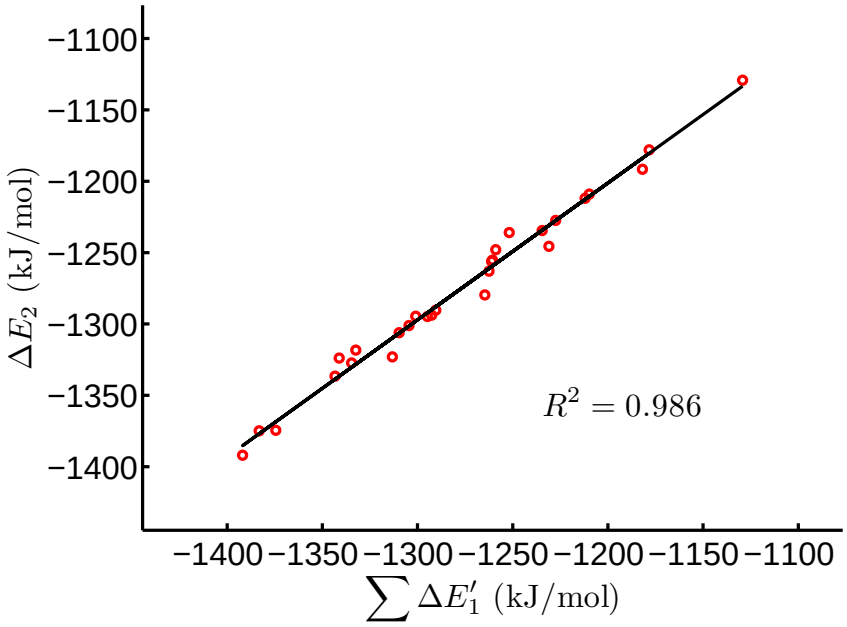

(b) ΔE_2 v.s. $\sum \Delta E_1'$

Figure 6.15: ΔE_2 against (a) $\sum \Delta E_1$ and (b) $\sum \Delta E_1'$ in Am^{3+}-bisazine complexes. The R^2 values correspond to linear fitting. Note that ΔE_2 corresponds to the bisazines' E^3_{int}, ΔE_1 stands for the corresponding single azines' E^3_{int}, and $\Delta E_1'$ stands for half the E^3_{int} of the bisazine constructed from two of the same azines (data from Tables 6.2.1 and 6.2.5).

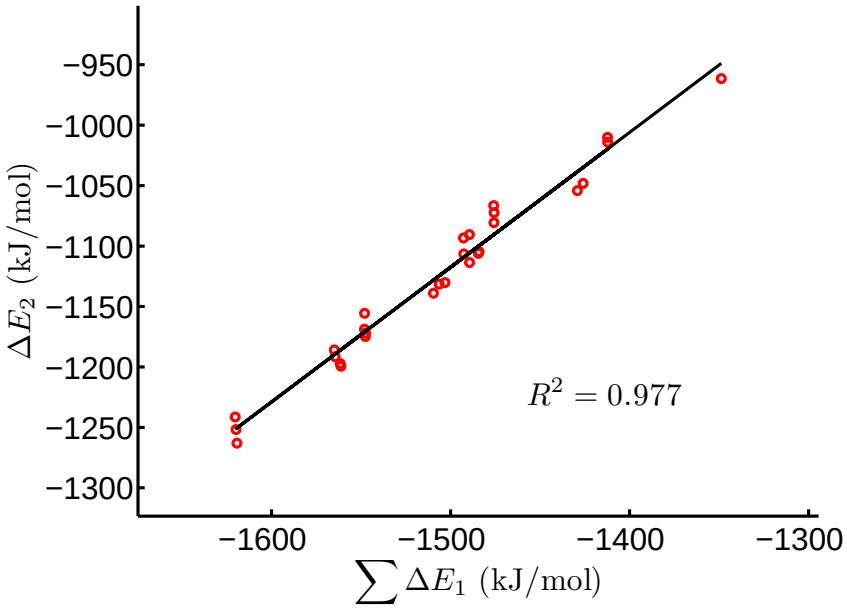

(a) ΔE_2 v.s. $\sum \Delta E_1$

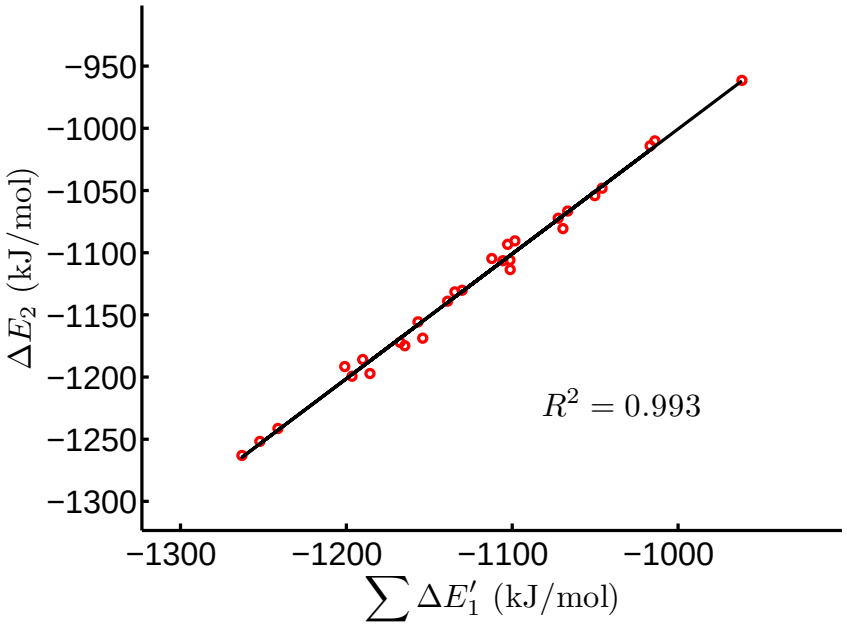

(b) ΔE_2 v.s. $\sum \Delta E_1'$

Figure 6.16: ΔE_2 against (a) $\sum \Delta E_1$ and (b) $\sum \Delta E_1'$ in Cm^{3+}-bisazine complexes. The R^2 values correspond to linear fitting. Note that ΔE_2 corresponds to the bisazines' E^3_{int}, ΔE_1 stands for the corresponding single azines' E^3_{int}, and $\Delta E_1'$ stands for half the E^3_{int} of the bisazine constructed from two of the same azines (data from Tables 6.2.1 and 6.2.6).

$\sum \Delta E_1'$ correlates better with ΔE_2; the R^2 in these three cases are all larger than 0.986, which is extremely high; thus, in comparison to ΔE_1, the new indicator $\Delta E_1'$ is an even better guide to an azine component's contribution to a bisazine's affinity for these 3 An^{3+} ions.

6.3 Lanthanide-bisazine complexes and the contribution from single azine components

In Section 6.2, I reported bond interaction energies and some QTAIM properties of actinide-azine and actinide-bisazine complexes, and established the correlation between the interaction energy of An^{3+}-bisazine complexes and their components. I introduced a new indicator $\sum \Delta E_1'$, which is better than $\sum \Delta E_1$ for estimating the binding energies of bisazines. Since the aim of the SANEX process is to separate the minor actinides from lanthanides, it is natural to investigate if this correlation is still valid for lanthanide complexes other than with La. In this section, I now calculate the 1:1 Ce^{3+}, Eu^{3+} and Gd^{3+} complexes with the same 7 single azine donors and chosen bisazine ligands, to compare an early lanthanide with actinides (Ce^{3+}), and also to compare the lanthanides with similar electronic configuration to the minor actinides and which are the most difficult from which to separate the minor actinides, i.e., Eu^{3+} and Gd^{3+}. All calculations are at same level as the lanthanum complexes and actinide complexes in the previous sections.

Firstly, I calculate the Ce^{3+}-, Eu^{3+}- and Gd^{3+}-single azine complexes. Note that the lanthanide ion is constrained on the vector from the centre of the azine to the coordinating nitrogen atom in geometry optimisation. However, since calculations of Eu^{3+}-**7** did not fully optimise, only the other complexes are used in the following analysis. The calculated E_{int}^3, bond length and selected QTAIM properties are summarised in Table 6.3.1. The results are quite similar as the ligands vary; all ρ_{BCP} range from 0.026 to 0.063. For Ce^{3+} complexes, the delocalisation indices δ ranges from 0.418 to 0.538; for Eu^{3+} complexes, δ ranges from 0.181 to 0.293; for Gd^{3+} complexes, δ ranges from 0.361 to 0.473.

CeL^{3+}, L={**1-7**}							
azine	**1**	**2**	**3**	**4**	**5**	**6**	**7**
E^3_{int}	-800.5	-811.1	-742.6	-743.1	-743.5	-756.0	-670.9
R	2.522	2.559	2.576	2.586	2.601	2.583	2.618
ρ_{BCP}	0.063	0.061	0.056	0.055	0.052	0.056	0.049
$\nabla^2\rho_{BCP}$	0.100	0.082	0.094	0.094	0.094	0.091	0.103
V_{BCP}	-0.052	-0.046	-0.044	-0.043	-0.040	-0.043	-0.039
G_{BCP}	0.038	0.033	0.034	0.033	0.032	0.033	0.032
H_{BCP}	-0.013	-0.013	-0.010	-0.010	-0.008	-0.010	-0.007
δ	0.538	0.522	0.468	0.422	0.433	0.444	0.418
$Q^{\text{QTAIM}}_{\text{Ln}}$	2.295	2.336	2.280	2.245	2.298	2.296	2.266
EuL^{3+}, L={**1-7**}							
azine	**1**	**2**	**3**	**4**	**5**	**6**	**7**
E^3_{int}	-1180.4	-1214.8	-1164.5	-1182.9	-1181.0	-1186.7	N/A
R	2.587	2.771	2.627	2.759	2.767	2.786	N/A
ρ_{BCP}	0.043	0.027	0.039	0.030	0.028	0.026	N/A
$\nabla^2\rho_{BCP}$	0.129	0.084	0.117	0.088	0.090	0.083	N/A
V_{BCP}	-0.039	-0.020	-0.033	-0.022	-0.021	-0.019	N/A
G_{BCP}	0.036	0.020	0.031	0.022	0.022	0.020	N/A
H_{BCP}	-0.003	0.001	-0.002	0.000	0.001	0.001	N/A
δ	0.293	0.190	0.260	0.219	0.199	0.181	N/A
$Q^{\text{QTAIM}}_{\text{Ln}}$	1.900	1.948	1.922	1.920	1.929	1.943	N/A
GdL^{3+}, L={**1-7**}							
azine	**1**	**2**	**3**	**4**	**5**	**6**	**7**
E^3_{int}	-1081.2	-1101.3	-1061.2	-1054.2	-1058.5	-1066.6	-962.5
R	2.534	2.587	2.557	2.571	2.636	2.684	2.574
ρ_{BCP}	0.054	0.047	0.049	0.048	0.042	0.038	0.048
$\nabla^2\rho_{BCP}$	0.107	0.096	0.108	0.106	0.092	0.082	0.106
V_{BCP}	-0.045	-0.037	-0.041	-0.039	-0.031	-0.026	-0.039
G_{BCP}	0.036	0.030	0.034	0.033	0.027	0.023	0.033
H_{BCP}	-0.009	-0.006	-0.007	-0.006	-0.004	-0.003	-0.006
δ	0.473	0.451	0.436	0.394	0.378	0.361	0.405
$Q^{\text{QTAIM}}_{\text{Ln}}$	2.103	2.171	2.098	2.047	2.115	2.107	2.086

Table 6.3.1: The bond interaction energy E^3_{int} (kJ/mol), bond lengths R (Å), the electron density at the BCP ρ_{BCP} (a.u), the Laplacian at the BCP $\nabla^2\rho_{BCP}$ (a.u), the potential energy density V_{BCP} (a.u), the gradient kinetic energy density $G_{BCP}(a.u)$, the total energy of the BCP H_{BCP} (a.u), the delocalisation index δ (a.u), and the QTAIM partial charge on the lanthanide atom $Q^{\text{QTAIM}}_{\text{Ln}}$ (a.u) of lanthanide complexes with azines **1-7** in aqueous environment (Ln=Ce,Eu,Gd). N/A = not available.

These values are lower than the results from the actinide complexes, which indicates less covalency in the lanthanide complexes. The correlation between bond length and ρ_{BCP} is shown in Figure 6.17. All complexes with the 7 azines are correlated together with $R^2 = 0.864$ in exponential curve fitting. The pattern of the QTAIM partial charge on the lanthanide atom $Q_{\mathrm{Ln}}^{\mathrm{QTAIM}}$ (Ce > Gd > Eu) is similar to the actinide calculations (Th > Cm > Am). Besides, $Q_{\mathrm{Ln}}^{\mathrm{QTAIM}}$ are smaller than the corresponding $Q_{\mathrm{An}}^{\mathrm{QTAIM}}$ in Table 6.2.1.

Figure 6.18(a) shows E_{int}^{3} in Ln^{3+}-single azines. The E_{int}^{3} of Ce^{3+}-bisazine complexes show the staircase structure similar to Figure 6.9, which indicates that the Ce^{3+}-bisazine complexes follow the 3 groups defined in Section 6.1: **1** and **2** have strong affinity, **3**, **4**, **5** and **6** have medium affinity, and **7** has weak affinity. For E_{int}^{3} of the Gd^{3+}-bisazine complexes, the staircase structure is less obvious as the energy gap between the strong affinity group and the medium affinity group is very small. The staircase structure disappears in the E_{int}^{3} of Eu-bisazine complexes, for which the E_{int}^{3} of Eu^{3+}-**1** is even lower than Eu^{3+}-**4**, Eu^{3+}-**5** and Eu^{3+}-**6**.

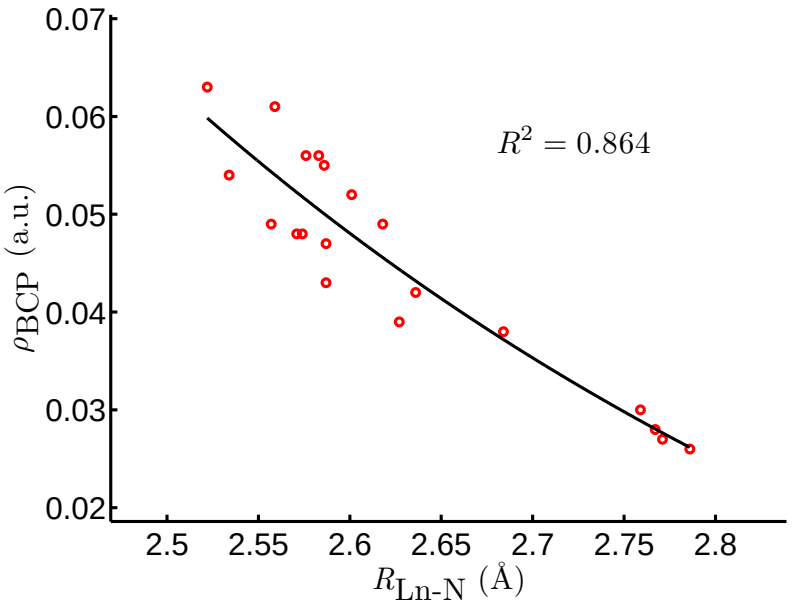

Figure 6.17: ρ_{BCP} against bond length in lanthanide complexes (Ln = Ce, Eu, Gd) with single azine ligands optimised with PCM. The R^2 value corresponds to exponential fitting: $\rho_{BCP} = 10.907\exp(-1.927R) - 0.0246$.

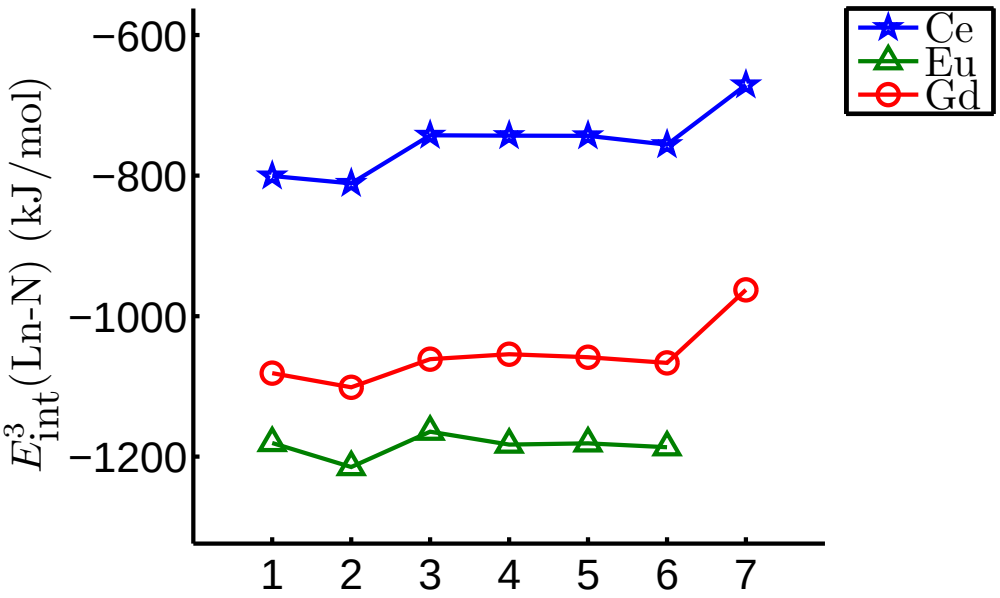

(a) Ln^{3+}-single azine

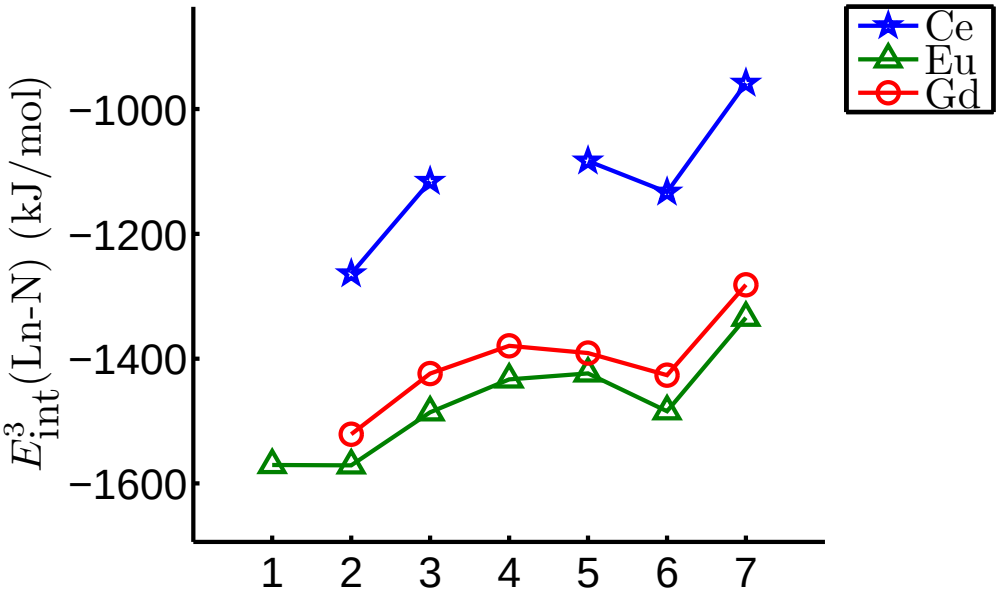

(b) Ln^{3+}-bisazine

Figure 6.18: E^3_{int} for Ln-azines, with azines **1-7** in Figure 6.2.

For the bisazines complexes, I have calculated Ce^{3+}, Eu^{3+} and Gd^{3+} complexes with all 28 possible combinations of bisazines for comparison to the results from the La^{3+}-bisazines and An^{3+}-bisazines in the previous sections. All computations are performed with the same protocol as the single azine complexes, except for releasing the constraints in the geometry optimisations. However, the geometries of 7 Ce^{3+}-bisazine complexes (Ce^{3+}-(**1**-**1**), Ce^{3+}-(**1**-**4**), Ce^{3+}-(**1**-**5**), Ce^{3+}-(**2**-**3**), Ce^{3+}-(**2**-**6**), Ce^{3+}-(**3**-**5**) and Ce^{3+}-(**4**-**4**)), 3 Eu^{3+}-bisazine complexes (Eu^{3+}-(**1**-**7**), Eu^{3+}-(**4**-**5**) and Eu^{3+}-(**5**-**6**)) and 7 Gd^{3+}-bisazine complexes (Gd^{3+}-(**1**-**1**), Gd^{3+}-(**1**-**4**), Gd^{3+}-(**2**-**4**), Gd^{3+}-(**2**-**6**), Gd^{3+}-(**3**-**5**), Gd^{3+}-(**3**-**7**) and Gd^{3+}-(**5**-**6**)) did not fully optimise; hence only the optimised ones are used in the following analysis.

The calculated E^3_{int} and the QTAIM partial charge on the lanthanide atom $Q^{\text{QTAIM}}_{\text{Ln}}$ are summarised in Table 6.3.2 (Ce^{3+}-bisazine), Table 6.3.3 (Eu^{3+}-bisazine), and Table 6.3.4 (Gd^{3+}-bisazine). Similar to the single azine complexes, for each lanthanide, the QTAIM partial charge on the lanthanide atoms in all complexes containing this lanthanide varies only slightly; for all Ce^{3+}-bisazine complexes, $Q^{\text{QTAIM}}_{\text{Ce}}$ ranges from 2.213 to 2.312; for all Eu^{3+}-bisazine complexes, $Q^{\text{QTAIM}}_{\text{Eu}}$ ranges from 1.808 to 1.930; for all Gd^{3+}-bisazine complexes, $Q^{\text{QTAIM}}_{\text{Gd}}$ ranges from 1.992 to 2.129. The pattern of $Q^{\text{QTAIM}}_{\text{Ln}}$ (Ce > Gd > Eu) is also similar to the actinide calculations (Th > Cm > Am).

The E^3_{int} of Ln^{3+}-(***x***-***x***), lanthanide-bisazine complexes containing two of the same single azines, corresponds to twice the $\Delta E'_1$ defined in Section 6.1; this has been shown to be a good indicator of the binding strength of La^{3+}-bisazine and An^{3+}-bisazine complexes. In comparison to the single azine complexes, Figure 6.18(b) shows the interaction energies of Ln^{3+}-(***x***-***x***). Although there are 3 Ln^{3+}-(***x***-***x***) which did not optimise, the staircase structures in Figure 6.18(b) are still more obvious than for E^3_{int} of the single azine complexes in Figure 6.18(a). The 3 groups defined in Section 6.1 are clear in Figure 6.18(b), and for the group with medium affinity, **3** and **6** always have stronger affinity than **4** and **5**, which is similar to the An^{3+}-(***x***-***x***).

Bisazine	E^3_{int}	$Q^{\text{QTAIM}}_{\text{Ce}}$	Bisazine	E^3_{int}	$Q^{\text{QTAIM}}_{\text{Ce}}$
(**1**-**2**)	-1244.3	2.294	(**3**-**7**)	-1034.1	2.223
(**1**-**3**)	-1159.4	2.236	(**4**-**5**)	-1072.2	2.245
(**1**-**6**)	-1173.0	2.274	(**4**-**6**)	-1101.3	2.233
(**1**-**7**)	-1086.2	2.255	(**4**-**7**)	-1009.9	2.213
(**2**-**2**)	-1264.1	2.312	(**5**-**5**)	-1083.4	2.306
(**2**-**4**)	-1156.6	2.251	(**5**-**6**)	-1095.5	2.290
(**2**-**5**)	-1163.7	2.305	(**5**-**7**)	-1017.2	2.270
(**2**-**7**)	-1103.3	2.283	(**6**-**6**)	-1133.2	2.282
(**3**-**3**)	-1115.8	2.222	(**6**-**7**)	-1049.7	2.273
(**3**-**4**)	-1086.9	2.217	(**7**-**7**)	-958.6	2.245
(**3**-**6**)	-1125.1	2.256			

Table 6.3.2: The bond interaction energy E^3_{int} (kJ/mol), and the QTAIM partial charge on the cerium atom $Q^{\text{QTAIM}}_{\text{Ce}}$ (a.u) of Ce^{3+}-bisazine complexes in aqueous environment.

Bisazine	E^3_{int}	$Q^{\text{QTAIM}}_{\text{Eu}}$	Bisazine	E^3_{int}	$Q^{\text{QTAIM}}_{\text{Eu}}$
(**1**-**1**)	-1570.5	1.808	(**3**-**4**)	-1463.6	1.850
(**1**-**2**)	-1554.8	1.892	(**3**-**5**)	-1445.9	1.889
(**1**-**3**)	-1504.7	1.851	(**3**-**6**)	-1487.1	1.881
(**1**-**4**)	-1500.6	1.829	(**3**-**7**)	-1407.7	1.855
(**1**-**5**)	-1491.8	1.896	(**4**-**4**)	-1433.4	1.851
(**1**-**6**)	-1519.8	1.898	(**4**-**6**)	-1477.2	1.865
(**2**-**2**)	-1571.1	1.930	(**4**-**7**)	-1398.0	1.841
(**2**-**3**)	-1504.2	1.905	(**5**-**5**)	-1423.6	1.909
(**2**-**4**)	-1509.7	1.881	(**5**-**7**)	-1385.1	1.872
(**2**-**5**)	-1491.6	1.919	(**6**-**6**)	-1484.3	1.896
(**2**-**6**)	-1520.4	1.909	(**6**-**7**)	-1407.5	1.880
(**2**-**7**)	-1439.8	1.888	(**7**-**7**)	-1334.4	1.850
(**3**-**3**)	-1486.0	1.858			

Table 6.3.3: The bond interaction energy E^3_{int} (kJ/mol), and the QTAIM partial charge on the europium atom $Q^{\text{QTAIM}}_{\text{Eu}}$ (a.u) of Eu^{3+}-bisazine complexes in aqueous environment.

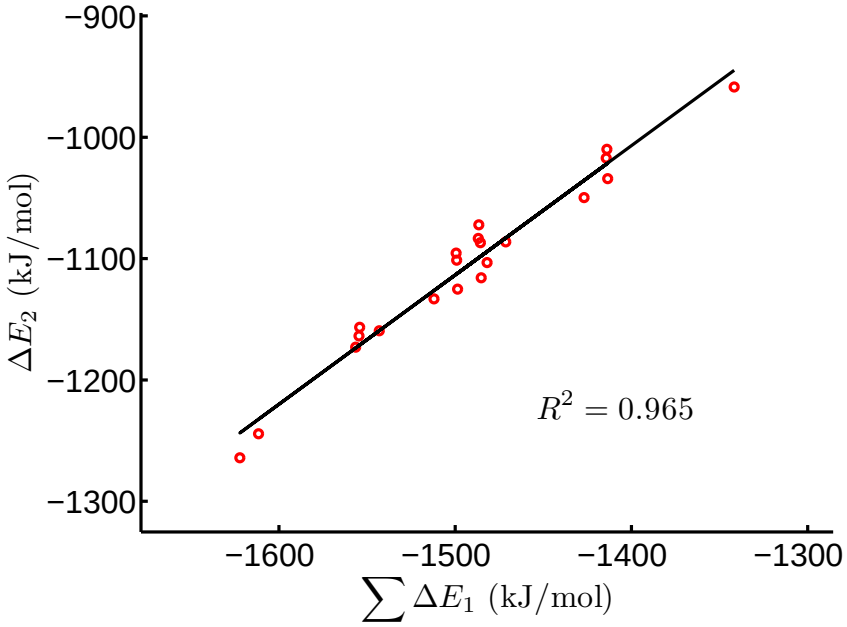

(a) ΔE_2 v.s. $\sum \Delta E_1$: 21 Ce^{3+}-bisazine complexes

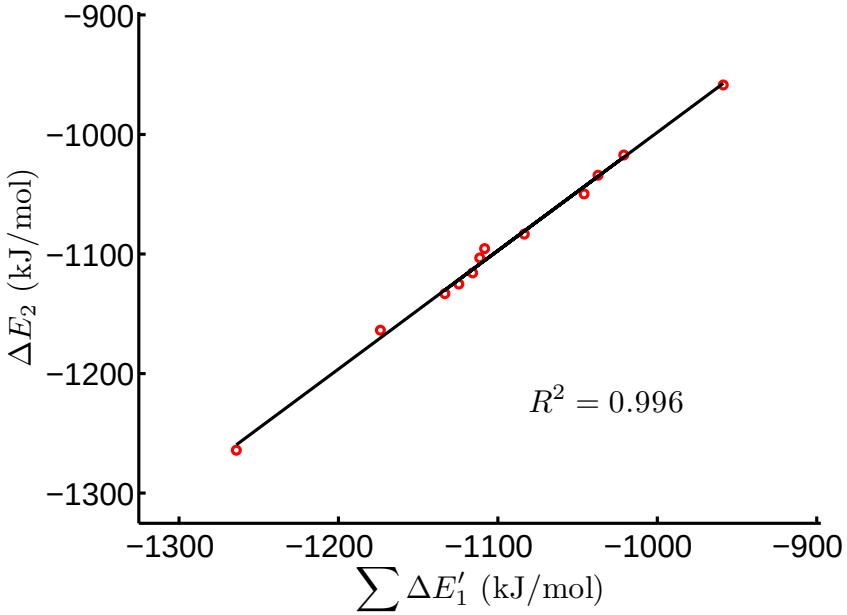

(b) ΔE_2 v.s. $\sum \Delta E_1'$: 12 Ce^{3+}-bisazine complexes

Figure 6.19: ΔE_2 against (a) $\sum \Delta E_1$ and (b) $\sum \Delta E_1'$ in Ce^{3+}-bisazine complexes. Only optimised Ce^{3+}-complexes with available $\sum \Delta E_1$ and $\sum \Delta E_1'$ are used. The R^2 values correspond to linear fitting. Note that ΔE_2 corresponds to the bisazines' E_{int}^3, ΔE_1 stands for the corresponding single azines' E_{int}^3, and $\Delta E_1'$ stands for half the E_{int}^3 of the bisazine constructed from two of the same azines (data from Tables 6.3.1 and 6.3.2).

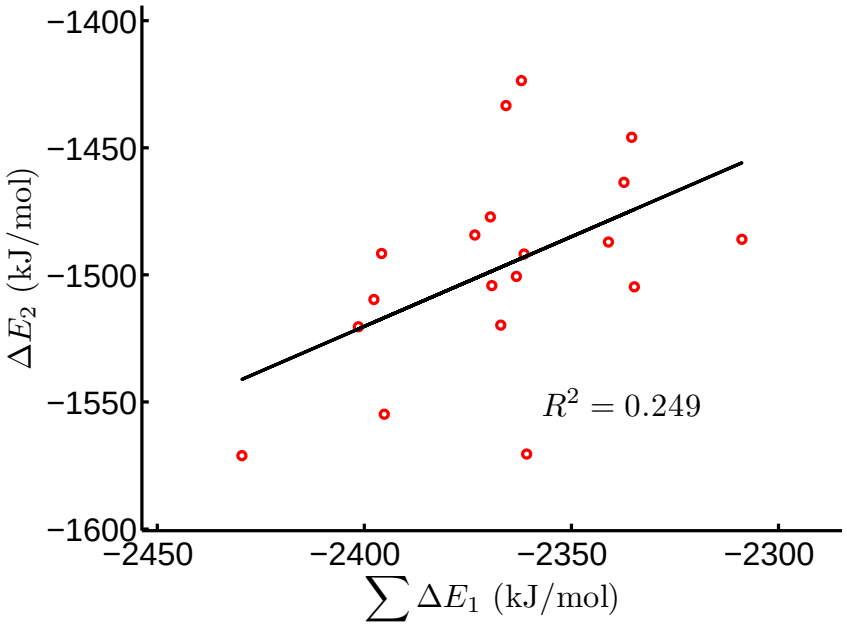

(a) ΔE_2 v.s. $\sum \Delta E_1$: 19 Eu^{3+}-bisazine complexes

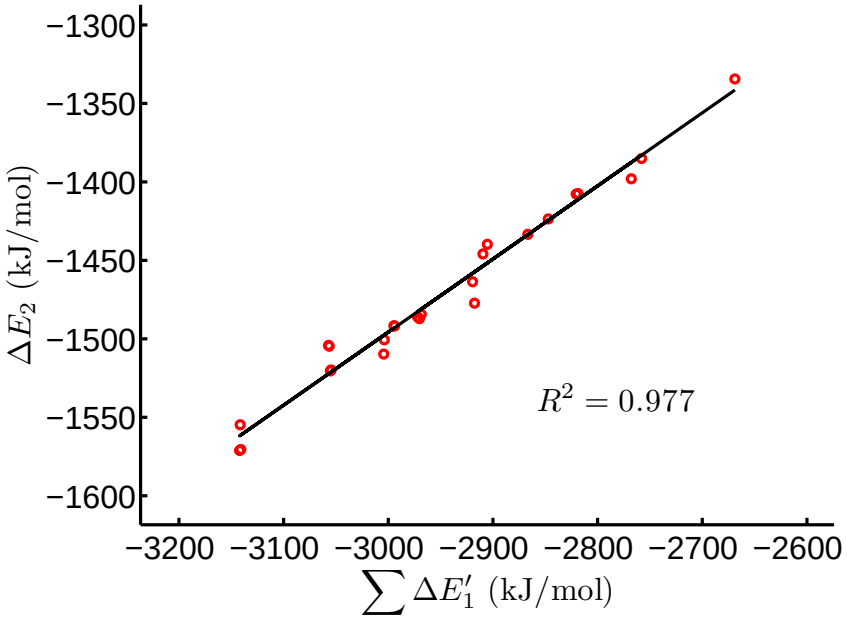

(b) ΔE_2 v.s. $\sum \Delta E_1'$: 25 Eu^{3+}-bisazine complexes

Figure 6.20: ΔE_2 against (a) $\sum \Delta E_1$ and (b) $\sum \Delta E_1'$ in Eu^{3+}-bisazine complexes. Only optimised Eu^{3+}-complexes with available $\sum \Delta E_1$ and $\sum \Delta E_1'$ are used. The R^2 values correspond to linear fitting. Note that ΔE_2 corresponds to the bisazines' E^3_{int}, ΔE_1 stands for the corresponding single azines' E^3_{int}, and $\Delta E_1'$ stands for half the E^3_{int} of the bisazine constructed from two of the same azines (data from Tables 6.3.1 and 6.3.3).

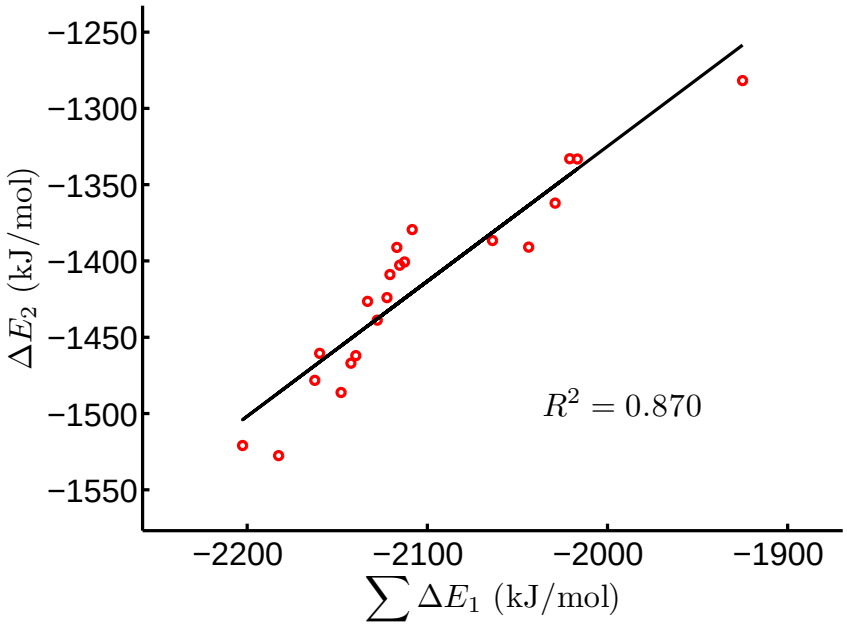

(a) ΔE_2 v.s. $\sum \Delta E_1$: 21 Gd^{3+}-bisazine complexes

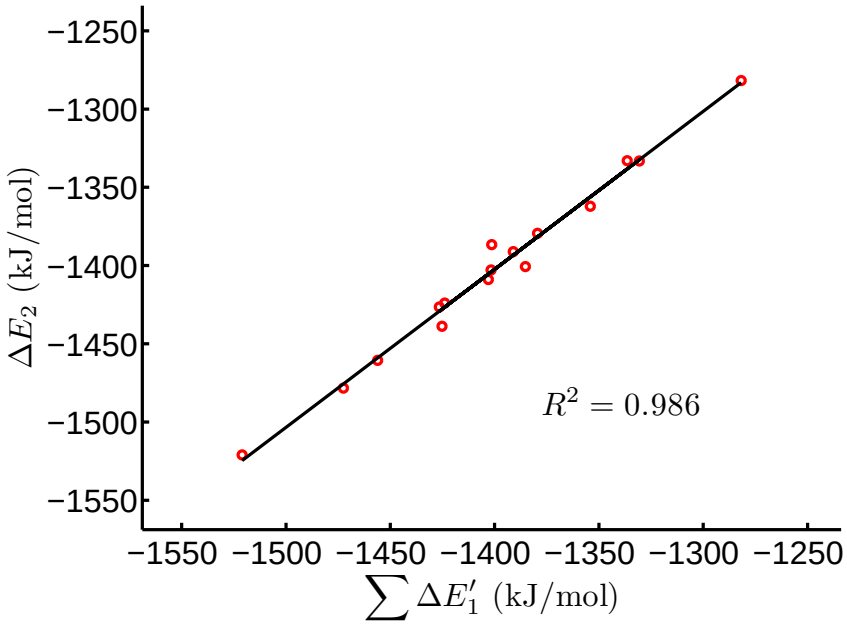

(b) ΔE_2 v.s. $\sum \Delta E_1'$: 16 Gd^{3+}-bisazine complexes

Figure 6.21: ΔE_2 against (a) $\sum \Delta E_1$ and (b) $\sum \Delta E_1'$ in Gd^{3+}-bisazine complexes. Only optimised Gd^{3+}-complexes with available $\sum \Delta E_1$ and $\sum \Delta E_1'$ are used. The R^2 values correspond to linear fitting. Note that ΔE_2 corresponds to the bisazines' E^3_{int}, ΔE_1 stands for the corresponding single azines' E^3_{int}, and $\Delta E_1'$ stands for half the E^3_{int} of the bisazine constructed from two of the same azines (data from Tables 6.3.1 and 6.3.4).

Bisazine	E^3_{int}	$Q^{\text{QTAIM}}_{\text{Gd}}$	Bisazine	E^3_{int}	$Q^{\text{QTAIM}}_{\text{Gd}}$
(**1**-**2**)	-1527.6	2.042	(**3**-**6**)	-1438.8	2.032
(**1**-**3**)	-1467.0	2.052	(**4**-**4**)	-1379.4	2.025
(**1**-**5**)	-1462.1	2.059	(**4**-**5**)	-1400.7	1.992
(**1**-**6**)	-1486.2	2.040	(**4**-**6**)	-1408.9	2.024
(**1**-**7**)	-1390.9	2.081	(**4**-**7**)	-1333.2	2.025
(**2**-**2**)	-1521.0	2.129	(**5**-**5**)	-1391.1	2.074
(**2**-**3**)	-1478.3	2.058	(**5**-**7**)	-1333.0	2.045
(**2**-**5**)	-1460.6	2.076	(**6**-**6**)	-1426.5	2.100
(**2**-**7**)	-1386.6	2.102	(**6**-**7**)	-1362.1	2.016
(**3**-**3**)	-1424.0	2.063	(**7**-**7**)	-1281.8	2.024
(**3**-**4**)	-1402.8	2.048			

Table 6.3.4: The bond interaction energy E^3_{int} (kJ/mol), and the QTAIM partial charge on the gadolinium atom $Q^{\text{QTAIM}}_{\text{Gd}}$ (a.u) of Gd^{3+}-bisazine complexes in aqueous environment.

The linear regressions of ΔE_2, the bisazines' interaction energies with the three lanthanides (Ce, Eu and Gd), with either (a) $\sum \Delta E_1$, the sum of the corresponding single azines' interaction energies, or (b) $\sum \Delta E'_1$, the sum of the contribution of a single azine in a bisazine constructed from two of the same azines, are shown in Figure 6.19, Figure 6.20 and Figure 6.21. Note that Eu-**7** and a few Ln^{3+}-bisazine did not optimise, thus only the data from the optimised bisazines with available $\sum \Delta E_1$ or $\sum \Delta E'_1$ are used in the linear regression.

For the correlation between ΔE_2 and $\sum \Delta E_1$, strong correlation is found for the Ce^{3+}-bisazine complexes (R^2=0.965), which almost forms a straight line; the Gd^{3+}-bisazine complexes show medium-strong correlation with $R^2 = 0.870$, which is obviously not linear; on the contrary, the Eu^{3+}-bisazine complexes show almost no correlation with $R^2 = 0.249$. This is consistent with Figure 6.18(a), in which the Eu^{3+}-single azine complexes do not show the staircase structure shown in all other complexes. Additionaly, the nonlinearity in the Gd^{3+}-bisazine data may be attributed to the small differences in E^3_{int} for the Gd^{3+}-single azine complexes, which is also reflected in the weak staircase structure in Figure 6.18(a). By contrast, the correlation between ΔE_2 and $\sum \Delta E'_1$ is extremely good in all cases; the R^2 are all larger than 0.977. This

is consistent with the significant staircase structure shown in Figure 6.18(b). The result from de Sahb *et al.* for La do not apply for other Ln, but the new indicator $\sum \Delta E_1'$ correlates with ΔE_2 much better for Ln-complexes; therefore, I believe $\sum \Delta E_1'$ is better for the estimation of a bisazine's affinity to these 3 Ln^{3+} ions. It is noteworthy that the major difference between $\sum \Delta E_1$ and $\sum \Delta E_1'$ is that $\Delta E_1'$ takes the whole bisazine structure into consideration to incorporate the effect of chelation, and hence it is much closer to the situation in BTP-like ligands.

6.4 Actinide-BTP and lanthanide-BTP compounds

Chapter 5 showed strong correlation between E_{int}^3 and $\left|\Delta Q_{\text{M}}^{\text{QTAIM}}\right|$ on formation of simple actinide-ligand compounds; this correlation has also been established for the An^{3+}-bisazine complexes in Section 6.2. In addition, I verified the correlation between the interaction energy of M^{3+}-bisazine complexes and the contribution of their components (M=La, Ce, Eu, Gd, Th-Cm); the strong correlation between the bisazines' interaction energies (ΔE_2) and the sum of corresponding single azines' interaction energies ($\sum \Delta E_1$) is found for most of the complexes. Furthermore, I introduced a new indicator $\sum \Delta E_1'$, which is better than $\sum \Delta E_1$ for estimating the binding energies of bisazines to selected actinides and lanthanides. As the overall aim of my research is to enhance the understanding of the bonding nature in BTP complexes, it is necessary to examine if the correlations found in previous sections are valid for BTP.

Firstly, I calculate 1:1 M^{3+}-BTP complexes with the same protocol as all M-bisazine calculations in this chapter. All molecules are optimised with the TPSSh functional and the Stuttgart small-core ECP and basis sets for the metal and cc-pVTZ basis sets for other elements, with the inclusion of aqueous environment via PCM. E_{int}^3-type interaction energies of the M-N bonds in these complexes are calculated as Eq. 5.1 where each term reflects a gas-phase single-point calculation at the geometry optimised with solvent effects;

the subsequent QTAIM charge analysis is also based on the same gas-phase wavefunction.

The calculated E^3_{int} and the QTAIM partial charge on the metal atom $Q^{\text{QTAIM}}_{\text{M}}$ are summarised in Table 6.4.1. E^3_{int} of the M-BTP complexes are rather higher than for the M-single azine and M-bisazine complexes, which can be attributed to the higher coordination number of BTP. In contrast, the range of $Q^{\text{QTAIM}}_{\text{M}}$ of the M-BTP complexes are similar to the M-bisazine complexes; more specifically, $Q^{\text{QTAIM}}_{\text{M}}$ of Th^{3+}-BTP, Pa^{3+}-BTP and U^{3+}-BTP are a bit lower than the corresponding Th-bisazine, Pa-bisazine and U-bisazine complexes, respectively, but $Q^{\text{QTAIM}}_{\text{M}}$ of the BTP complexes of the other 4 actinides are slightly higher than some corresponding bisazine complexes.

Molecule	E^3_{int}	$Q^{\text{QTAIM}}_{\text{M}}$
La^{3+}-BTP	-1439.5	2.321
Ce^{3+}-BTP	-1496.1	2.253
Eu^{3+}-BTP	-1790.2	1.884
Gd^{3+}-BTP	-1791.3	2.020
Th^{3+}-BTP	-1459.7	2.329
Pa^{3+}-BTP	-1459.3	2.368
U^{3+}-BTP	-1470.4	2.339
Np^{3+}-BTP	-1502.3	2.290
Pu^{3+}-BTP	-1559.6	2.172
Am^{3+}-BTP	-1631.2	2.022
Cm^{3+}-BTP	-1535.7	2.253

Table 6.4.1: The bond interaction energy E^3_{int} (kJ/mol), and the QTAIM partial charge on the metal atom $Q^{\text{QTAIM}}_{\text{M}}$ (a.u) of M^{3+}-BTP complexes in aqueous environment (M = La, Ce, Eu, Gd, Th-Cm).

Figure 6.22 shows $Q^{\text{QTAIM}}_{\text{M}}$ of the M-BTP complexes. For the actinides, the trend of $Q^{\text{QTAIM}}_{\text{M}}$ is similar to the previous results for actinide-simple ligand compounds and actinide-bisazine compounds, except for the decrease at Th^{3+}-BTP. This decrease for thorium also occured for the AnL_3 complexes in Section 5.4. $Q^{\text{QTAIM}}_{\text{Ln}}$ of the M-BTP complexes of lanthanum and 3 other lanthanides are also shown in Figure 6.22, and shows a similar trend (Th > Cm > Am) in comparison to actinide complexes (Ce > Gd > Eu), which is similar to the Ln-azine compounds in Section 6.3. Besides, $Q^{\text{QTAIM}}_{\text{Ln}}$ are smaller than the

corresponding $Q_{\mathrm{An}}^{\mathrm{QTAIM}}$. Figure 6.23 shows good negative correlation between $\left|\Delta Q_{\mathrm{M}}^{\mathrm{QTAIM}}\right|$ and E_{int}^{3} for M^{3+}-BTP complexes with $R^2 = 0.899$, showing that the lanthanides and actinides follow a similar trend.

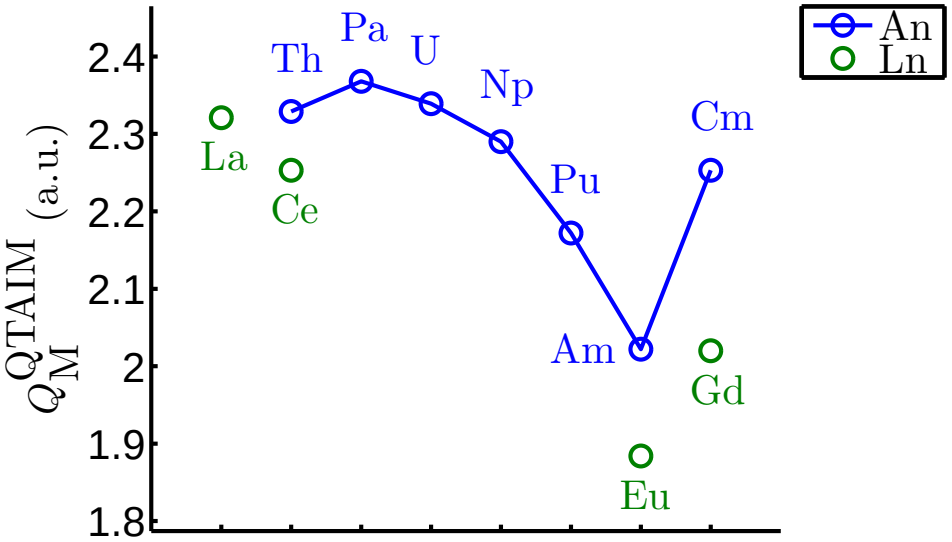

Figure 6.22: $Q_{\mathrm{M}}^{\mathrm{QTAIM}}$ in M-BTP (M = La, Ce, Eu, Gd, Th-Cm).

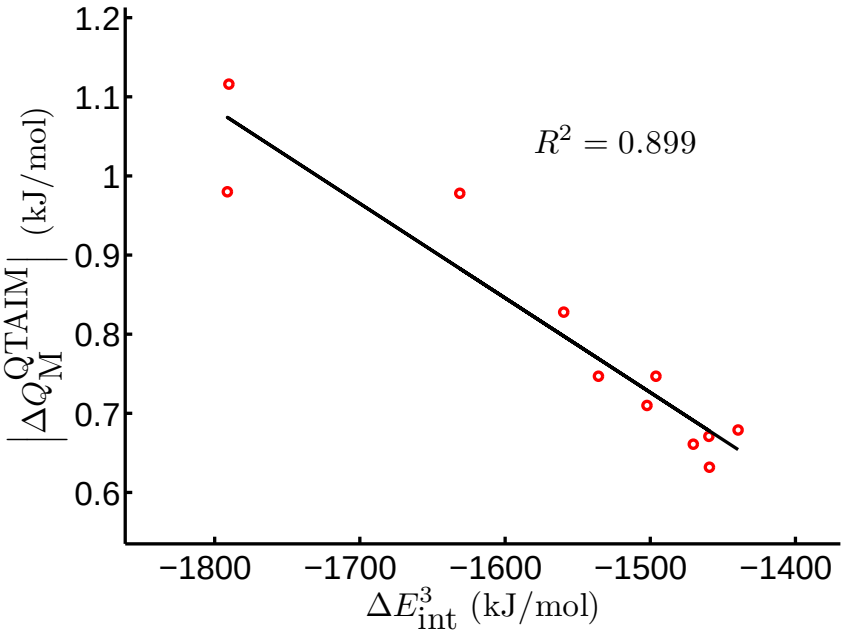

Figure 6.23: $\left|\Delta Q_{\mathrm{An}}^{\mathrm{QTAIM}}\right|$ against E_{int}^{3} in M^{3+}-BTP complexes. The R^2 value corresponds to linear fitting.

BTP consists of a pyridine at the centre and 2 terminal azines **6**; hence, it is natural to verify if $\Delta E_{\mathrm{int}}^{3}$(BTP), the interaction energy of M-BTP complexes,

can be viewed as the sum of the binding energies to individual single azines, that is, the sum of the contributions from 1 azine **1** and 2 azine **6**, which can be represented with either ΔE_1, the sum of the corresponding single azines' interaction energies, or $\Delta E_1'$, the sum of the contribution of a single azine in a bisazine constructed from two of the same azines. Note that Ce^{3+}-(**1**-**1**) and Gd^{3+}-(**1**-**1**) did not optimise, thus data from Ce^{3+}-BTP and Gd^{3+}-BTP are not used in the analysis of $\sum \Delta E_1'$.

Figure 6.24 shows the correlation between ΔE_{int}^3(BTP) and either (a) $\sum \Delta E_1$ or (b) $\sum \Delta E_1'$; clearly ΔE_2 is strongly correlated with both $\sum \Delta E_1$ ($R^2 = 0.962$) and $\sum \Delta E_1'$ ($R^2 = 0.991$). It should be noted that the point for Gd^{3+}-BTP obviously deviates slightly from the regression line in Figure 6.24(a), but it is not used in the regresson in Figure 6.24(b), which may result in the higher R^2 value. Note also that the regression now takes lanthanum and the selected lanthanides into consideration, which were not included in the previous sections, and the resulting correlations are still very strong.

In the previous sections, the regression analyses are performed by fixing a specific metal atom (La, Th, Am, Cm, Ce, Eu and Gd) and varying the bisazine; this is different from Figure 6.24, in which the metal varies and the ligand is fixed. However, in Section 6.2, I have already shown the correlation between the actinide interaction energies of bisazines constructed with two of the same azines and their single azine components (Figure 6.13) while fixing either a specific azine or a specific actinide, and both ways give good correlations. This shows that the contributions of the individual single azines, either $\sum \Delta E_1$ or $\sum \Delta E_1'$, are capable of predicting the interaction energies of these metal cations to BTP molecules.

In the reprocessing of nuclear waste, the extraction processes are performed between aqueous HNO_3 solution and organic phases, in which the nitrates anions act as counter ions that balance the charge of the triply-charged MA and lanthanide ions. To probe the effect of counter ions in my systems, I replace the nitrate anions to chloride anions for simplicity in geometry opti-

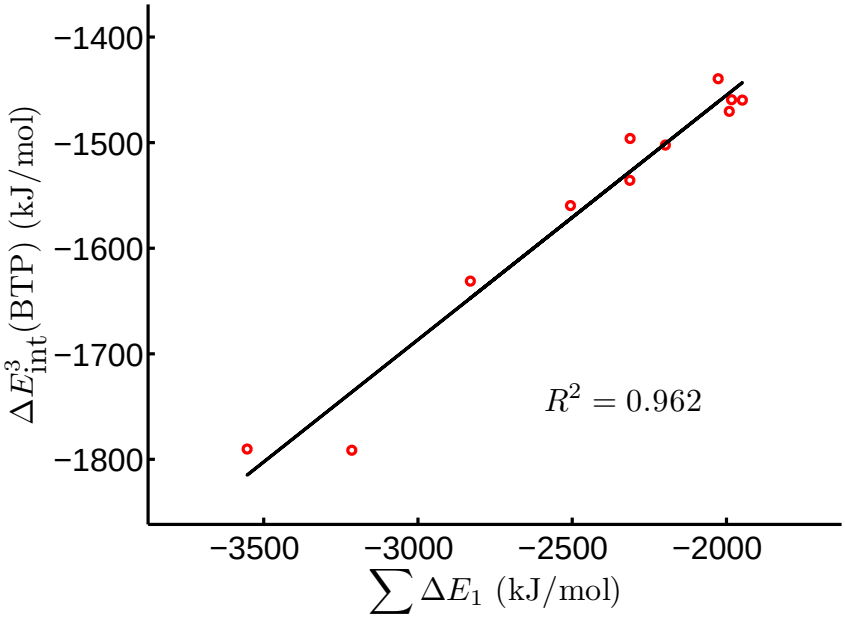

(a) ΔE^3_{int}(BTP) v.s. $\sum \Delta E_1$

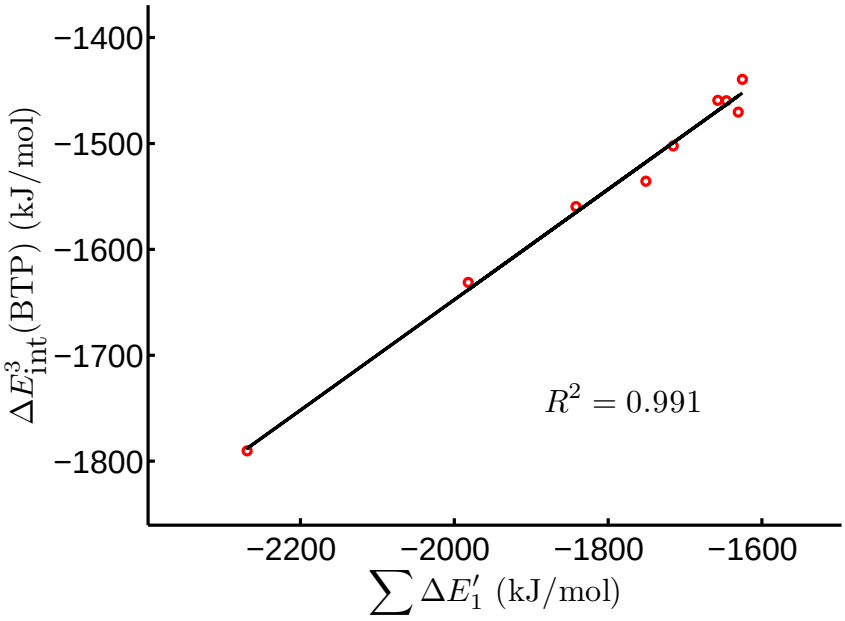

(b) ΔE^3_{int}(BTP) v.s. $\sum \Delta E'_1$

Figure 6.24: ΔE^3_{int}(BTP) against (a) $\sum \Delta E_1$ and (b) $\sum \Delta E'_1$ in M^{3+}-BTP complexes. Only M^{3+}-BTP complexes with available $\sum \Delta E_1$ and $\sum \Delta E'_1$ are used. The R^2 values correspond to linear fitting. Note that ΔE_1 stands for the corresponding single azines' E^3_{int}, and $\Delta E'_1$ stands for half the E^3_{int} of the bisazine constructed from two of the same azines (data from Tables 6.1.1, 6.1.2, 6.2.1, 6.2.2, 6.3.1, 6.3.2, 6.3.3 and 6.3.4).

misation, and then performed calculations with the same protocol on neutral Cl_3-M-BTP complexes, which contains 3 chloride anions to balance the charge of the compound. The interaction energy of a Cl_3-M-BTP is defined as the reaction energy between the neutral Cl_3-M fragment and the BTP ligand:

$$E_{\text{int}}[\text{Cl}_3\text{-M-BTP}] = E[\text{Cl}_3\text{-M-BTP}] - (E[\text{Cl}_3\text{-M}] + E[\text{BTP}]) \tag{6.1}$$

where M stands for the metal. Note that all terms in Equation 6.1 correspond to neutral chemical structures, thus the notation does not have the superscript representing the positive charge.

The calculated E_{int} and the QTAIM partial charge on the metal atom $Q_{\text{M}}^{\text{QTAIM}}$ are summarised in Table 6.4.2. E_{int} of the Cl_3-M-BTP complexes are much lower than the corresponding M^{3+}-BTP complexes since the two fragments of Cl_3-M-BTP are both neutral. The trend of E_{int} of Cl_3-M-BTP is totally different to E_{int}^3 of M^{3+}-BTP; the value of E_{int} decreases gradually across the actinide series, to the lowest value at Cl_3-Am-BTP, then increases at Cl_3-Cm-BTP. Nevertheless, this trend is consistent with the E_{int}^2 of AnX^{2+} complexes in Section 5.1, which is an interaction energy of a less positive-charged ion to a neutral ligand. Complexes containing lanthanum and other lanthanides have lower E_{int} than corresponding actinide complexes; this is necessary for a good extractant, i.e., we want it to bind more strongly to MA than Eu and Gd.

Figure 6.25 shows $Q_{\text{M}}^{\text{QTAIM}}$ of the Cl_3-M-BTP complexes. For the actinides, the $Q_{\text{M}}^{\text{QTAIM}}$ of Th and Pa complex are higher in comparison with M^{3+}-BTP complexes, but $Q_{\text{M}}^{\text{QTAIM}}$ of Np and Pu complex are lower than M^{3+}-BTP complexes, resulting in a trend which, although similar to the previous results for M-BTP complexes, has a larger range of charge decrease from Th to Am. To verify if the interaction energy is correlated with the absolute charge difference in this case, $Q_{\text{M}}^{\text{QTAIM}}(\text{Cl}_3\text{-M})$, the QTAIM partial charge on the metal atom of the fragment Cl_3-M, and the absolute value of charge difference $\left|\Delta Q_{\text{M}}^{\text{QTAIM}}\right|$ are also listed in Table 6.4.2. The linear regression of E_{int} on $\left|\Delta Q_{\text{M}}^{\text{QTAIM}}\right|$ is

Molecule	E_{int}	$Q_{\text{M}}^{\text{QTAIM}}$	$Q_{\text{M}}^{\text{QTAIM}}(\text{Cl}_3\text{-M})$	$\Delta Q_{\text{M}}^{\text{QTAIM}}$
Cl_3-La-BTP	-248.0	2.116	2.069	0.047
Cl_3-Ce-BTP	-245.9	2.091	2.026	0.065
Cl_3-Eu-BTP	-225.1	1.971	1.826	0.145
Cl_3-Gd-BTP	-227.4	1.911	1.846	0.064
Cl_3-Th-BTP	-497.9	2.617	1.977	0.640
Cl_3-Pa-BTP	-421.6	2.506	2.004	0.502
Cl_3-U-BTP	-338.0	2.317	2.048	0.269
Cl_3-Np-BTP	-286.2	2.141	1.979	0.161
Cl_3-Pu-BTP	-270.6	2.049	1.946	0.103
Cl_3-Am-BTP	-260.0	2.006	1.904	0.102
Cl_3-Cm-BTP	-268.4	2.037	1.970	0.067

Table 6.4.2: The bond interaction energy E_{int} (kJ/mol), the QTAIM partial charge on the metal atom $Q_{\text{M}}^{\text{QTAIM}}$ (a.u) of Cl_3-M-BTP complexes and the QTAIM partial charge on the metal atom in the neutral Cl_3-M fragment $Q_{\text{M}}^{\text{QTAIM}}(\text{Cl}_3\text{-M})$ (a.u) (M = La, Ce, Eu, Gd, Th-Cm). The absolute charge difference $\left|\Delta Q_{\text{M}}^{\text{QTAIM}}\right|$ is listed as well.

shown in Figure 6.26, which shows strong correlation even though the trend of E_{int} is different to complexes without counter ions.

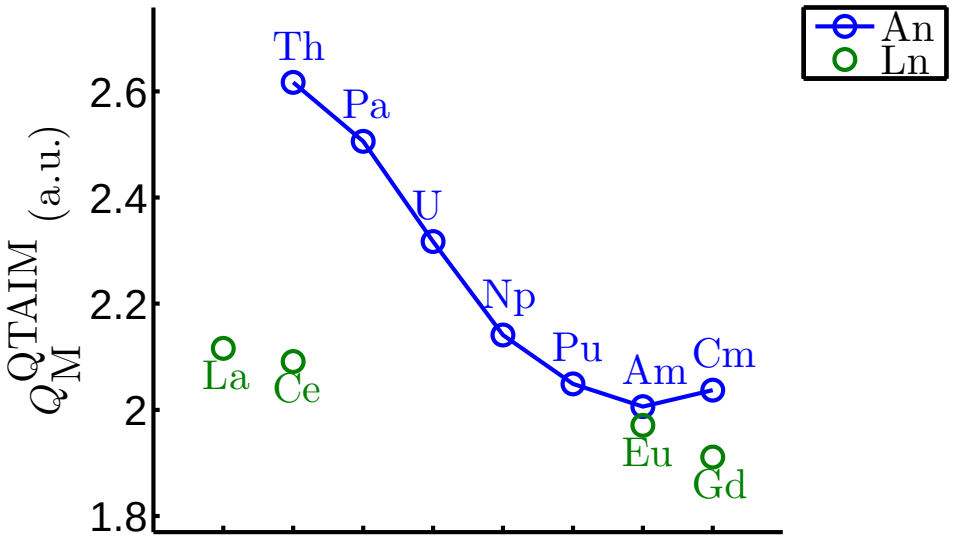

Figure 6.25: $Q_{\text{M}}^{\text{QTAIM}}$ in Cl_3-M-BTP (M = La, Ce, Eu, Gd, Th-Cm).

6.5 Summary

In summary, the correlation between the interaction energy of La^{3+}-bisazine complexes and their components, observed by de Sahb et al., has been repro-

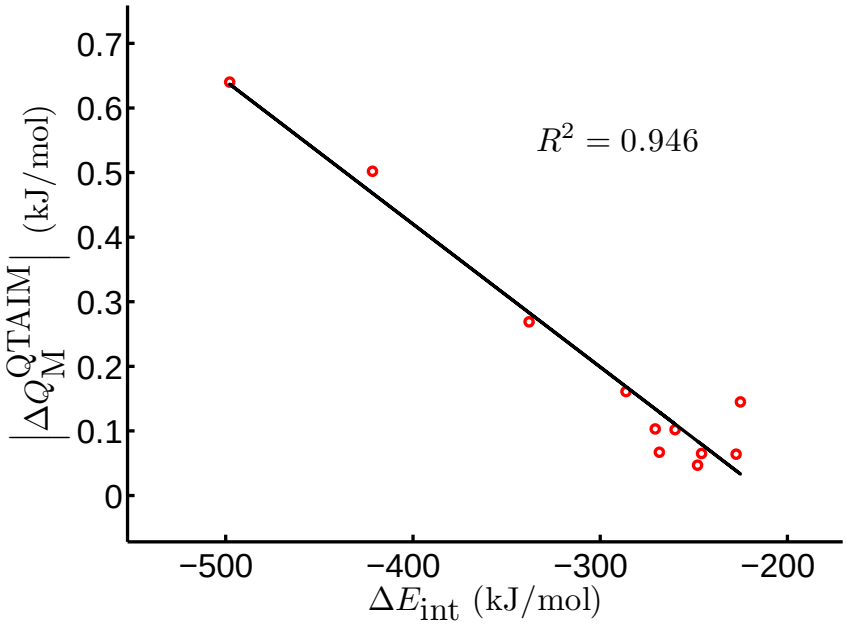

Figure 6.26: $\left|\Delta Q_{\mathrm{An}}^{\mathrm{QTAIM}}\right|$ against E_{int} in Cl_3-M-BTP complexes. The R^2 values correspond to linear fitting.

duced, and significantly extended to bisazine complexes with selected actinides (Th-Cm) and lanthanides (Ce, Eu, Gd), with almost all cases showing good correlation. However, the correlation between ΔE_2 and $\sum \Delta E_1$ for Eu-bisazine and Gd-bisazine complexes is not as good as in other cases. In contrast, this problem does not appear for the new indicator $\sum \Delta E_1'$, which incorporates the effect of chelation by taking the whole bisazine structure into consideration and shows very good correlation in all cases.

These correlations have been found by fixing the metal atom and varying the bisazine; however, for bisazines constructed with two of the same azines, strong correlation between its actinide interaction energies and the single azine components are valid while fixing either a specific azine or a specific actinide, and both ways give good correlations. This shows that the predictive capability of bisazine interaction energies from ΔE_1 is good for both ways, and provides the relationship between ΔE_1 and $\Delta E_1'$. E_{int} of M^{3+}-BTP complexes show strong correlations with both $\sum \Delta E_1$ and $\sum \Delta E_1'$ by fixing a ligand (BTP) and varying the metal from La, Ce, Eu, Gd and Th-Cm.

The correlation between the change of the QTAIM partial charge on

the actinide atom in the An-N bond formation process and bond interaction energy is valid for actinide-single azine complexes, actinide-bisazine complexes, M-BTP complexes and Cl_3-M-BTP complexes; the inclusion of selected lanthanide-BTP complexes does not break this correlation. The trend of E_{int} changes drastically in the presence of counter ions, but still correlates strongly with $\left|\Delta Q_{\mathrm{M}}^{\mathrm{QTAIM}}\right|$.

Chapter 7

General Conclusions

To provide enhanced understanding of the selectivity of BTP and related ligands for the MAs, this thesis utilises DFT and QTAIM to study the bonding in An/Ln-N bonds. Several types of An/Ln (An = Th-Cm, Ln = La, Ce, Eu and Gd) compounds are investigated in different chapters, the actinide oxides in Chapter 4, the simple An-N based ligand complexes in Chapter 5, and the An/Ln-bisazine compounds and An/Ln-BTP complexes in Chapter 6.

In Chapter 4, several computational methods are benchmarked by calculating ionisation energies and bond dissociation energies of actinide oxides in order to obtain a reliable electron density for subsequent QTAIM analysis. Among the benchmarked methods, the TPSSh functional usually gives slighter smaller MAEs than the other two functionals tested; for the inclusion of relativistic effects, employing ECPs mostly gives smaller MAEs than using the DKH/DKHSO Hamiltonian. Based on these wavefunctions, QTAIM analysis of these actinide oxides are performed to find possible relationships between bond strength and QTAIM properties. The bond dissociation energy is not well correlated with ρ_{BCP}, ∇^2_{BCP}, V_{BCP}, G_{BCP}, H_{BCP} or δ; however, strong correlation is found between the bond dissociation energy and $\left|\Delta Q_{\mathrm{An}}^{\mathrm{QTAIM}}\right|$, the absolute value of the change of the QTAIM partial charge on the actinide atom, in all cationic actinide oxides. In addition, this correlation still holds while separating the actinide monoxide to form the oxygen dianion.

In Chapter 5, a series of calculations is performed on some simple actinide

complexes with one or three nitrogen-based ligands to analyse the relationship between bond strength and QTAIM properties of the An-N bonds. Similar to the actinide oxides, ρ_{BCP}, H_{BCP} and δ do not correlate well with bond interaction energy in these actinide compounds, but the strong correlation between $\left|\Delta Q_{\mathrm{An}}^{\mathrm{QTAIM}}\right|$ in the An-N bond formation process and the bond interaction energy remains valid, with and without the inclusion of solvent effects. The value of $Q_{\mathrm{An}}^{\mathrm{QTAIM}}$ decreases gradually across the actinide series, to the lowest value at the americium complexes, then increases at curium. The alpha LUMOs of the americium compounds show significant contribution from an occupied orbital of the ligands, which implies strong LMCT and leads to an Am(II) oxidation state. This effect occurs in other actinide compounds to some extent, and the different extent of LMCT explains the trend in $Q_{\mathrm{An}}^{\mathrm{QTAIM}}$.

In Chapter 6, the correlation between the interaction energy of La^{3+}-bisazine complexes (ΔE_2) and their components ($\sum \Delta E_1$), observed by de Sahb et al., has been extended to An^{3+}-bisazine and other Ln^{3+}-bisazine complexes. A new indicator $\sum \Delta E_1'$, which includes the chelation effect, shows correlations stronger than $\sum \Delta E_1$ for all cases. Although these correlations are found by fixing the metal atom and varying the bisazines, strong correlation between interaction energies of An-($\boldsymbol{x}$-$\boldsymbol{x}$) (bisazines constructed with the same single azines) and their single azine components is also valid when the metal varies and the bisazine is fixed, and this correlation holds for An^{3+}-BTP and Ln^{3+}-BTP complexes. This provides the relationship between the two indicators, $\sum \Delta E_1'$ and $\sum \Delta E_1$. In addition, the correlation between $\left|\Delta Q_{\mathrm{An}}^{\mathrm{QTAIM}}\right|$ and bond interaction energy is also valid for M^{3+}-bisazine complexes, M^{3+}-BTP complexes and Cl_3-M-BTP complexes.

The results in this thesis provide a strong foundation for future work on the design of BTP-like SANEX ligands. A possible direction of future work is to establish the relationship between the interaction energies of multiple polyazine ligands and the contributions from their azine components when a specific metal is fixed, especially for the MA and the corresponding lanthanides.

In addition, recent researches have shown great An/Ln selectivity in ligands containing triazolyl groups,[92] which may be also analysed by decomposition into the contributions from individual heterocycles. Another direction to investigate is how the presence of counter ions affects this relationship by tuning the atomic partial charge of the molecular fragment. I hope some future researcher will find these correlations interesting, and continue research on the basis of these results.

Appendix A

Spin multiplicity for each actinide/lanthanide complex

In Chapter 4, I use the calculated spin multiplicity of actinide monoxides from Ref [88]; for the actinide dioxides, a few values of spin multiplicity are calculated for each molecule, and the most stable species are chosen. The results are listed in Table A.0.1.

An	AnO	AnO^+	AnO^{2+}	AnO_2	AnO_2^+	AnO_2^{2+}
Th	1	2	1	1	2	1
Pa	2	3	2	2	1	2
U	5	4	3	3	2	1
Np	6	5	4	4	3	2
Pu	7	6	5	5	4	3
Am	8	7	6	6	5	4
Cm	9	8	7	7	6	5

Table A.0.1: The spin multiplicity for actinide oxides.

For the actinide-simple ligand compounds in Section 5, I tested different values of spin multiplicity of all compounds, and I find that all the f-electrons are in the high-spin states. The results are listed in Table A.0.2. Therefore, I assume the actinide complexes with nitrogen-based ligands (azines, bisazines and BTPs) are also in their high-spin states, so the spin multiplicity are same as Table A.0.2.

An	
Th	2
Pa	3
U	4
Np	5
Pu	6
Am	7
Cm	8

Table A.0.2: The spin multiplicity for actinide-simple ligand compounds, AnX^{2+} and $(AnL)^{3+}$ (An=Th-Cm, X and L stands for different type ligands which is used in Section 5.1.)

Appendix B

Computational data for the benchmarking calculations

(This page is empty.)

Method	Th	Pa	U	Np	Pu	Am	Cm	MAE
First ionisation energies								
EXP[86]	608.502	568.224	597.632	604.542	581.418	576.382	578.081	
Literature(B3LYP)[88]	589.000	551.000	562.000	567.000	581.000	580.000	547.000	19.647
B3LYP+ECP	605.428	557.493	562.074	567.797	573.693	579.308	532.352	19.139
B3LYP+DKH2	653.288	566.374	536.701	558.901	569.942	574.785	567.858	23.146
B3LYP+DKHSO	654.631	481.990	545.856	560.155	571.286	576.201	571.104	31.989
TPSS+ECP	587.983	565.515	569.284	539.647	541.608	545.630	488.271	38.170
TPSS+DKH2	1039.295	551.582	557.326	532.365	542.801	540.397	562.406	85.325
TPSS+DKHSO	561.143	557.153	923.682	534.194	531.334	541.758	563.993	73.434
TPSSh+ECP	586.763	564.923	565.970	537.885	539.862	544.101	511.727	36.079
TPSSh+DKH2	575.196	566.730	558.956	525.784	535.223	538.703	529.875	39.038
TPSSh+DKHSO	576.496	564.650	566.387	526.979	536.521	540.094	520.384	39.096
Second ionisation energies								
EXP[86]	1124.054	1128.878	1128.878	1114.406	1138.527	1157.824	1196.418	
B3LYP+ECP	1154.999	1168.386	1125.591	1135.801	1155.658	1172.895	1197.299	16.199
B3LYP+DKH2	1090.683	1181.192	1145.335	1255.456	1151.795	1167.244	1196.053	33.541
B3LYP+DKHSO	1085.374	1183.627	1139.635	1258.159	1154.166	1169.717	1171.994	37.537
TPSS+ECP	1139.782	1102.417	1075.019	1114.048	1133.728	1150.439	1161.672	21.441
TPSS+DKH2	661.488	1145.848	1064.902	1111.545	1129.122	1143.963	1098.296	86.662
TPSS+DKHSO	1110.298	1148.219	704.493	1113.676	1144.080	1146.245	1089.487	75.675
TPSSh+ECP	1139.844	1105.928	1079.042	1106.645	1126.194	1142.893	1154.011	24.662
TPSSh+DKH2	1145.649	1113.036	1066.929	1126.771	1120.915	1135.861	1147.643	28.524
TPSSh+DKHSO	1140.714	1108.033	1054.957	1129.082	1123.218	1138.256	1150.069	29.124

Table B.0.1: Computational data for the ionisation energies of An with different method. (Unit: kJ/mol)

Method	ThO	PaO	UO	NpO	PuO	AmO	CmO	MAE
First ionisation energies								
EXP[86]	637.141	569.264	581.932	588.561	588.561	598.209	617.506	
Literature(B3LYP)[88]	630.000	623.000	598.000	604.000	612.000	630.000	643.000	24.730
B3LYP	630.239	625.066	593.174	602.127	611.689	626.153	640.033	23.016
B3LYP+ZP+BSSE	652.605	683.280	486.012	602.780	612.192	626.932	632.937	43.915
B3LYP+DKH	626.765	623.033	606.316	593.127	614.592	623.132	642.399	24.135
B3LYP+DKH+ZP+BSSE	649.131	681.248	499.154	593.780	615.095	623.911	635.303	40.286
B3LYP+DKHSO	627.060	647.606	555.834	599.008	615.028	624.200	642.625	28.935
B3LYP+DKHSO+ZP+BSSE	649.426	705.821	448.672	599.661	615.531	624.978	635.529	52.138
TPSS	609.002	584.527	572.916	578.639	586.857	610.640	611.789	11.742
TPSS+ZP+BSSE	620.721	573.541	604.476	566.525	587.849	611.441	614.938	11.684
TPSS+DKH	599.963	577.153	574.415	572.956	584.543	606.651	613.269	12.126
TPSS+DKH+ZP+BSSE	611.682	566.166	605.974	560.841	585.535	607.453	616.419	13.382
TPSS+DKHSO	599.833	575.961	578.479	572.612	584.653	608.368	613.166	11.688
TPSS+DKHSO+ZP+BSSE	611.552	564.974	610.039	560.497	585.645	609.170	616.315	14.445
TPSSh	608.089	586.119	568.381	575.006	582.616	604.563	610.881	13.134
TPSSh+ZP+BSSE	608.572	597.577	576.054	570.998	582.660	605.445	606.511	14.922
TPSSh+DKH	600.033	583.038	569.559	566.315	584.222	599.954	611.755	13.905
TPSSh+DKH+ZP+BSSE	600.516	594.496	577.232	562.307	584.265	600.837	607.385	15.694
TPSSh+DKHSO	599.978	618.898	569.440	570.911	587.271	601.666	611.805	18.198
TPSSh+DKHSO+ZP+BSSE	600.461	630.355	577.113	566.903	587.314	602.548	607.435	19.987

Table B.0.2: Computational data for the first ionisation energies of AnO with different method. (Unit: kJ/mol)

Method	ThO	PaO	UO	NpO	PuO	AmO	CmO	MAE
				Second ionisation energies				
Exp[86]	1152.035	1167.473	1261.063	1295.798	1385.529	1452.104	1536.047	
Literature(SO-CASPT2)[87]	1138.527	1138.527	1196.418	1350.795	1350.795	1350.795	1524.468	44.245
B3LYP	1176.968	1201.042	1252.293	1340.629	1408.028	1485.247	1488.292	30.786
B3LYP+ZP+BSSE	1173.998	1200.626	1204.283	1336.074	1407.691	1483.146	1485.473	36.564
B3LYP+DKH	1173.831	1193.975	1195.552	1319.586	1388.782	1469.860	1474.484	31.453
B3LYP+DKH+ZP+BSSE	1170.861	1193.560	1147.543	1315.031	1388.446	1467.759	1471.665	37.231
B3LYP+DKHSO	1175.169	1170.807	1282.118	1319.095	1395.414	1476.265	1479.374	23.077
B3LYP+DKHSO+ZP+BSSE	1172.199	1170.392	1234.108	1314.539	1395.078	1474.163	1476.554	22.840
TPSS	1146.261	1187.227	1240.570	1317.192	1381.874	1451.399	1474.714	19.016
TPSS+ZP+BSSE	1113.000	1207.990	1216.460	1323.797	1381.308	1449.495	1462.491	33.220
TPSS+DKH	1140.702	1175.818	1276.775	1298.291	1366.022	1437.874	1455.814	21.693
TPSS+DKH+ZP+BSSE	1107.441	1196.582	1252.666	1304.896	1365.456	1435.970	1443.590	31.409
TPSS+DKHSO	1142.233	1178.363	1277.546	1303.386	1372.584	1444.345	1461.150	20.052
TPSS+DKHSO+ZP+BSSE	1108.972	1199.127	1253.436	1309.991	1372.017	1442.441	1448.926	29.548
TPSSh	1143.651	1180.735	1244.222	1323.675	1392.751	1463.621	1475.829	20.760
TPSSh+ZP+BSSE	1153.532	1181.424	1313.407	1340.043	1397.435	1461.556	1473.027	28.059
TPSSh+DKH	1138.319	1169.089	1233.688	1306.530	1365.269	1449.493	1460.067	21.756
TPSSh+DKH+ZP+BSSE	1148.201	1169.778	1302.873	1322.898	1369.952	1447.428	1457.264	24.869
TPSSh+DKHSO	1139.867	1134.476	1238.783	1306.924	1368.600	1455.996	1465.218	24.317
TPSSh+DKHSO+ZP+BSSE	1149.748	1135.165	1307.968	1323.291	1373.283	1453.932	1462.415	28.100

Table B.0.3: Computational data for the second ionisation energies of AnO with different method. (Unit: kJ/mol)

Method	ThO_2	PaO_2	UO_2	NpO_2	PuO_2	AmO_2	CmO_2	MAE
First ionisation energies								
Exp[86]	858.720	569.264	591.262	610.752	678.292	697.589	820.125	
Literature(SO-CASPT2)[87]	820.125	549.966	599.174	604.963	598.209	652.241	797.934	31.316
B3LYP	821.929	608.142	598.479	666.782	604.881	673.480	797.435	37.018
B3LYP+ZP+BSSE	820.634	608.630	568.062	671.183	622.024	678.054	801.565	36.492
B3LYP+DKH	819.887	603.095	602.118	659.879	623.047	666.117	777.268	37.460
B3LYP+DKH+ZP+BSSE	818.592	603.582	571.701	664.280	640.190	670.691	781.397	35.895
B3LYP+DKHSO	820.904	602.894	601.705	663.431	628.135	667.858	779.392	36.456
B3LYP+DKHSO+ZP+BSSE	819.608	603.382	571.288	667.832	645.278	672.432	783.521	35.008
TPSS	786.698	575.726	575.931	587.083	625.236	635.141	748.955	43.451
TPSS+ZP+BSSE	781.552	574.002	575.176	590.940	635.263	639.785	752.646	40.874
TPSS+DKH	790.202	566.929	990.458	1039.455	615.418	636.229	745.818	156.756
TPSS+DKH+ZP+BSSE	785.057	565.204	989.704	1043.313	625.444	640.873	749.508	155.558
TPSS+DKHSO	791.386	566.809	965.880	1010.036	619.287	638.260	748.092	147.722
TPSS+DKHSO+ZP+BSSE	786.241	565.085	965.126	1013.894	629.313	642.905	751.782	146.524
TPSSh	793.134	570.821	567.699	580.657	621.712	644.093	765.333	40.810
TPSSh+ZP+BSSE	726.542	501.548	495.648	495.155	539.007	541.718	663.021	123.338
TPSSh+DKH	790.144	567.076	567.892	590.982	615.661	636.391	745.872	44.570
TPSSh+DKH+ZP+BSSE	789.021	569.607	570.043	595.532	629.313	641.743	752.577	39.836
TPSSh+DKHSO	791.452	567.238	567.618	595.316	619.412	638.634	748.307	42.575
TPSSh+DKHSO+ZP+BSSE	790.329	569.769	569.769	599.867	633.064	643.987	755.013	37.888

Table B.0.4: Computational data for the first ionisation energies of AnO_2 with different method. (Unit: kJ/mol)

Method	ThO_2	PaO_2	UO_2	NpO_2	PuO_2	AmO_2	CmO_2	MAE
				Second ionisation energies				
Exp[86]	1601.657	1601.657	1408.686	1456.929	1456.929	1514.820	1727.088	
Literature(SO-CASPT2)[87]	1456.929	1639.286	1385.529	1503.242	1482.980	1570.781	1558.238	71.813
B3LYP	1601.065	1634.044	1466.305	1514.573	1656.836	1627.409	1570.633	88.171
B3LYP+ZP+BSSE	1599.285	1628.650	1412.031	1515.194	1647.563	1627.946	1561.801	80.003
B3LYP+DKH	1599.566	1630.999	1452.031	1501.688	1635.101	1608.842	1540.622	82.599
B3LYP+DKH+ZP+BSSE	1597.785	1625.605	1397.757	1502.309	1625.828	1609.378	1531.791	77.555
B3LYP+DKHSO	1600.136	1633.357	1457.240	1507.262	1640.766	1614.265	1543.748	85.533
B3LYP+DKHSO+ZP+BSSE	1598.356	1627.964	1402.966	1507.883	1631.493	1614.801	1534.916	79.000
TPSS	1560.108	1590.672	1454.374	1520.032	1545.065	1593.780	1520.260	76.464
TPSS+ZP+BSSE	1541.167	1689.517	1448.727	1519.753	1537.945	1593.863	1510.597	89.681
TPSS+DKH	1577.099	1602.583	1440.973	1537.084	1625.348	1585.655	1510.816	84.779
TPSS+DKH+ZP+BSSE	1558.158	1701.428	1435.325	1536.805	1618.228	1585.739	1501.154	101.134
TPSS+DKHSO	1578.280	1605.093	1446.386	1543.007	1631.548	1591.248	1514.135	87.799
TPSS+DKHSO+ZP+BSSE	1559.338	1703.938	1440.738	1542.728	1624.428	1591.332	1504.472	104.154
TPSSh	1558.448	1604.388	1454.562	1529.642	1554.030	1602.180	1539.044	76.719
TPSSh+ZP+BSSE	1607.789	1656.718	1522.099	1619.104	1649.597	1709.554	1639.244	116.004
TPSSh+DKH	1579.562	1602.356	1440.611	1534.193	1622.108	1584.742	1509.392	83.540
TPSSh+DKH+ZP+BSSE	1563.433	1582.881	1433.945	1533.603	1621.318	1584.390	1500.574	88.486
TPSSh+DKHSO	1581.028	1604.498	1445.687	1539.742	1627.891	1589.889	1512.305	86.300
TPSSh+DKHSO+ZP+BSSE	1564.899	1585.024	1439.021	1539.153	1627.101	1589.537	1503.488	90.634

Table B.0.5: Computational data for the second ionisation energies of AnO_2 with different method. (Unit: kJ/mol)

Method	ThO	PaO	UO	NpO	PuO	AmO	CmO	MAE
Bond dissociation energies								
Exp[86]	801.000	758.000	744.000	658.000	582.000	709.000		
Literature(B3LYP)[88]	855.000	784.000	715.000	595.000	494.000	688.000	45.571	
B3LYP	856.905	780.166	714.493	597.824	495.417	687.453	45.564	
B3LYP+ZP+BSSE	898.907	701.252	704.572	592.773	485.612	678.351	62.669	
B3LYP+DKH	857.787	753.134	715.328	606.864	505.949	689.430	38.858	
B3LYP+DKH+ZP+BSSE	899.788	674.220	705.407	601.812	496.144	680.327	62.295	
B3LYP+DKHSO	937.995	745.059	706.357	597.799	497.856	689.239	55.577	
B3LYP+DKHSO+ZP+BSSE	979.997	666.146	696.436	592.748	488.052	680.137	79.015	
TPSS	874.604	827.688	764.023	658.433	566.197	751.099	39.173	
TPSS+ZP+BSSE	854.671	816.221	747.830	648.842	556.440	743.416	31.442	
TPSS+DKH	876.849	854.706	763.522	670.392	572.865	755.331	44.897	
TPSS+DKH+ZP+BSSE	856.917	843.239	747.328	660.801	563.108	747.649	34.549	
TPSS+DKHSO	868.583	843.798	754.778	663.158	566.847	756.130	44.909	
TPSS+DKHSO+ZP+BSSE	848.651	832.331	738.585	653.567	557.090	748.447	37.375	
TPSSh	852.206	807.207	745.651	633.635	534.544	716.839	30.651	
TPSSh+ZP+BSSE	843.858	800.216	731.521	628.543	525.332	710.213	29.299	
TPSSh+DKH	849.562	814.515	748.100	639.055	542.726	721.271	30.905	
TPSSh+DKH+ZP+BSSE	841.214	807.524	733.969	633.963	533.514	714.646	28.853	
TPSSh+DKHSO	847.884	813.899	739.606	630.631	536.154	721.599	33.167	
TPSSh+DKHSO+ZP+BSSE	839.536	806.908	725.475	625.539	526.942	714.974	32.286	

Table B.0.6: Computational data for the bond dissociation energies of AnO with different method. (Unit: kJ/mol)

Method	ThO^+	PaO^+	UO^+	NpO^+	PuO^+	AmO^+	CmO^+	MAE
				Bond dissociation energies				
Exp[86]	843.000	800.000	774.000	760.000	651.000	560.000	670.000	
Literature(B3LYP)[88]	870.000	783.000	750.000	677.000	564.000	444.000	593.000	61.571
B3LYP	890.253	789.332	749.066	680.163	559.829	448.571	579.772	65.074
B3LYP+ZP+BSSE	877.156	773.119	777.314	669.589	554.274	437.988	577.766	66.533
B3LYP+DKH	933.446	801.127	683.519	681.102	562.214	457.601	614.889	72.464
B3LYP+DKH+ZP+BSSE	920.349	784.914	711.768	670.528	556.660	447.018	612.883	72.654
B3LYP+DKHSO	936.927	772.379	735.081	667.504	554.057	449.857	617.718	73.190
B3LYP+DKHSO+ZP+BSSE	923.831	756.166	763.330	656.930	548.502	439.274	615.712	73.702
TPSS	903.543	855.591	824.056	725.031	613.185	501.187	627.581	48.601
TPSS+ZP+BSSE	874.499	846.645	781.030	720.953	602.602	490.628	616.749	42.177
TPSS+DKH	1365.674	851.279	837.617	722.931	628.650	506.610	704.468	112.121
TPSS+DKH+ZP+BSSE	1336.630	842.333	794.590	718.852	618.066	496.052	693.636	102.603
TPSS+DKHSO	916.071	849.775	1189.000	716.360	609.839	500.237	706.958	102.767
TPSS+DKHSO+ZP+BSSE	887.028	840.829	1145.974	712.282	599.256	489.678	696.125	93.249
TPSSh	883.510	831.011	804.795	708.530	590.881	474.082	617.685	50.305
TPSSh+ZP+BSSE	870.393	811.205	790.132	698.408	585.745	463.988	615.429	47.451
TPSSh+DKH	883.830	833.254	803.911	707.569	590.056	481.475	639.391	46.643
TPSSh+DKH+ZP+BSSE	870.713	813.448	789.248	697.447	584.920	471.381	637.136	43.789
TPSSh+DKHSO	887.693	793.636	810.846	695.673	579.882	474.582	630.178	49.798
TPSSh+DKHSO+ZP+BSSE	874.576	773.831	796.182	685.551	574.746	464.487	627.923	52.603

Table B.0.7: Computational data for the bond dissociation energies of AnO^+ with different method. (Unit: kJ/mol)

Method	ThO^{2+}	PaO^{2+}	UO^{2+}	NpO^{2+}	PuO^{2+}	AmO^{2+}	CmO^{2+}	MAE
Bond dissociation energies								
Exp[86]	829.000	781.000	706.000	524.000	439.000	439.000	342.000	
B3LYP	868.285	756.676	622.364	475.335	307.458	136.219	288.779	97.636
B3LYP+ZP+BSSE	858.158	740.878	698.622	469.316	302.241	127.737	289.592	90.253
B3LYP+DKH	850.298	788.344	633.302	616.973	325.226	154.984	336.458	85.378
B3LYP+DKH+ZP+BSSE	840.171	772.546	709.560	610.954	320.009	146.503	337.271	75.194
B3LYP+DKHSO	847.132	785.199	592.598	606.568	312.808	143.309	310.338	95.978
B3LYP+DKHSO+ZP+BSSE	837.006	769.401	668.856	600.549	307.591	134.828	311.151	85.675
TPSS	897.064	770.782	658.505	521.887	365.038	200.228	314.539	66.869
TPSS+ZP+BSSE	901.281	741.072	639.589	511.204	355.022	191.573	315.930	78.413
TPSS+DKH	886.460	821.308	625.743	536.184	391.749	212.699	346.950	66.959
TPSS+DKH+ZP+BSSE	890.677	791.598	606.827	525.501	381.732	204.045	348.342	67.359
TPSS+DKHSO	884.136	819.631	615.947	526.649	381.336	202.137	335.295	69.672
TPSS+DKHSO+ZP+BSSE	888.353	789.922	597.031	515.967	371.319	193.482	336.686	71.970
TPSSh	879.703	756.204	639.615	491.499	324.324	153.355	295.866	88.691
TPSSh+ZP+BSSE	856.704	735.709	555.767	465.010	314.505	145.325	296.413	106.568
TPSSh+DKH	891.160	777.201	637.152	527.810	345.702	167.843	326.968	74.015
TPSSh+DKH+ZP+BSSE	868.162	756.706	553.303	501.320	335.883	159.813	327.515	90.803
TPSSh+DKHSO	888.540	767.193	627.020	517.831	334.500	156.842	315.029	81.732
TPSSh+DKHSO+ZP+BSSE	865.542	746.698	543.171	491.342	324.681	148.812	315.577	99.609

Table B.0.8: Computational data for the bond dissociation energies of AnO^{2+} with different method. (Unit: kJ/mol)

Method	ThO_2	PaO_2	UO_2	NpO_2	PuO_2	AmO_2	CmO_2	MAE
				Bond dissociation energies				
Exp[86]	684.000	780.000	750.000	632.000	599.000	509.000	405.000	
B3LYP	662.927	794.151	726.462	653.421	552.752	478.229	423.843	25.149
B3LYP+ZP+BSSE	630.124	727.175	782.945	642.230	544.078	466.861	413.041	36.425
B3LYP+DKH	657.284	792.388	782.344	671.901	596.602	496.195	439.411	22.995
B3LYP+DKH+ZP+BSSE	624.481	725.411	838.826	660.710	587.928	484.827	428.609	41.500
B3LYP+DKHSO	658.381	789.874	774.987	669.933	596.447	491.667	437.168	21.495
B3LYP+DKHSO+ZP+BSSE	625.578	722.898	831.470	658.742	587.773	480.299	426.366	40.719
TPSS	720.731	835.342	759.113	715.031	660.658	535.097	492.615	51.369
TPSS+ZP+BSSE	712.564	828.563	747.532	710.388	654.794	524.017	480.196	43.427
TPSS+DKH	404.525	478.642	769.541	705.747	150.331	-18.961	-108.966	309.245
TPSS+DKH+ZP+BSSE	396.357	471.863	757.960	701.103	144.467	-30.040	-121.385	313.257
TPSS+DKHSO	426.791	498.547	765.133	699.686	180.706	12.223	-69.999	287.364
TPSS+DKHSO+ZP+BSSE	418.624	491.769	753.551	695.042	174.842	1.143	-82.418	291.376
TPSSh	698.483	814.349	725.325	678.890	623.532	501.418	453.327	28.691
TPSSh+ZP+BSSE	689.647	800.241	712.173	672.877	616.795	490.502	442.866	25.536
TPSSh+DKH	700.134	820.466	747.702	697.672	645.588	519.308	468.383	34.979
TPSSh+DKH+ZP+BSSE	691.298	806.359	734.549	691.659	638.850	508.392	457.922	28.878
TPSSh+DKHSO	701.770	818.510	741.715	696.681	644.274	514.602	466.809	34.561
TPSSh+DKHSO+ZP+BSSE	692.934	804.402	728.563	690.668	637.536	503.685	456.348	29.806

Table B.0.9: Computational data for the bond dissociation energies of AnO_2 with different method. (Unit: kJ/mol)

Method	ThO_2^+	PaO_2^+	UO_2^+	NpO_2^+	PuO_2^+	AmO_2^+	CmO_2^+	MAE
Bond dissociation energies								
Exp[86]	462.000	780.000	741.000	610.000	509.000	410.000	202.000	
B3LYP	471.236	811.074	721.157	588.766	559.560	430.902	266.441	31.041
B3LYP+ZP+BSSE	462.095	801.825	700.895	573.827	534.245	415.739	244.413	24.514
B3LYP+DKH	464.161	812.326	786.542	605.148	588.147	453.210	304.543	44.255
B3LYP+DKH+ZP+BSSE	455.020	803.077	766.280	590.210	562.833	438.047	282.515	33.932
B3LYP+DKHSO	464.537	834.586	729.116	605.510	583.340	448.009	300.401	40.607
B3LYP+DKHSO+ZP+BSSE	455.396	825.337	708.854	590.572	558.026	432.845	278.373	35.966
TPSS	543.035	844.143	756.099	706.588	622.279	510.595	355.448	89.169
TPSS+ZP+BSSE	551.733	828.102	776.831	685.972	607.380	495.673	342.488	82.026
TPSS+DKH	214.285	488.866	353.498	239.247	119.456	-48.538	-241.515	369.814
TPSS+DKH+ZP+BSSE	222.983	472.825	374.230	218.631	104.558	-63.460	-254.474	376.958
TPSS+DKHSO	235.238	507.699	377.732	262.262	146.073	-17.669	-204.925	343.942
TPSS+DKHSO+ZP+BSSE	243.935	491.658	398.464	241.646	131.174	-32.591	-217.885	351.085
TPSSh	513.438	829.647	726.007	673.239	584.436	461.888	298.875	57.645
TPSSh+ZP+BSSE	571.678	896.270	792.579	748.720	660.447	554.229	386.356	128.040
TPSSh+DKH	510.023	836.429	749.369	673.006	614.148	482.872	334.267	69.445
TPSSh+DKH+ZP+BSSE	502.794	831.248	741.739	658.434	593.803	467.485	312.730	56.319
TPSSh+DKHSO	510.295	870.170	743.537	672.276	612.132	477.633	330.307	71.764
TPSSh+DKHSO+ZP+BSSE	503.066	864.989	735.907	657.704	591.787	462.247	308.770	60.094

Table B.0.10: Computational data for the bond dissociation energies of AnO_2^+ with different method. (Unit: kJ/mol)

Method	ThO_2^{2+}	PaO_2^{2+}	UO_2^{2+}	NpO_2^{2+}	PuO_2^{2+}	AmO_2^{2+}	CmO_2^{2+}	MAE
				Bond dissociation energies				
Exp[86]	0.000	317.000	529.000	504.000	403.000	256.000	0.000	
B3LYP	47.139	378.072	507.145	414.822	310.752	288.740	184.100	59.419
B3LYP+ZP+BSSE	36.808	373.801	493.147	394.707	294.374	270.939	168.085	65.103
B3LYP+DKH	38.427	375.303	530.064	423.046	341.829	314.229	238.404	51.944
B3LYP+DKH+ZP+BSSE	28.096	371.032	516.066	402.931	325.451	296.428	222.389	57.202
B3LYP+DKHSO	39.570	372.035	553.994	417.343	337.989	310.009	236.028	57.141
B3LYP+DKHSO+ZP+BSSE	29.239	367.764	539.996	397.228	321.611	292.208	220.012	57.226
TPSS	129.188	440.698	542.294	503.748	459.088	368.214	309.902	61.109
TPSS+ZP+BSSE	123.566	346.576	544.565	490.015	450.744	351.304	294.382	40.435
TPSS+DKH	-222.112	62.101	189.300	0.455	-139.870	-196.319	-296.517	418.667
TPSS+DKH+ZP+BSSE	-227.734	-32.021	191.570	-13.278	-148.214	-213.229	-312.037	444.834
TPSS+DKHSO	-200.809	80.969	208.892	22.642	-112.892	-164.572	-257.910	394.792
TPSS+DKHSO+ZP+BSSE	-206.431	-13.154	211.163	8.909	-121.236	-181.482	-273.431	420.960
TPSSh	98.640	405.993	515.667	467.273	423.157	323.329	235.660	45.308
TPSSh+ZP+BSSE	117.421	420.976	583.887	469.658	408.284	306.231	220.139	49.744
TPSSh+DKH	68.781	403.161	542.446	445.344	357.309	347.622	284.941	59.115
TPSSh+DKH+ZP+BSSE	87.562	418.144	610.667	447.729	342.437	330.524	269.420	74.834
TPSSh+DKHSO	69.134	400.147	536.633	439.457	352.841	343.740	283.219	58.644
TPSSh+DKHSO+ZP+BSSE	87.915	415.130	604.854	441.842	337.969	326.642	267.698	74.363

Table B.0.11: Computational data for the bond dissociation energies of AnO_2^{2+} with different method. (Unit: kJ/mol) The MAE in this table only considered the PaO_2^{2+}, UO_2^{2+}, NpO_2^{2+}, PuO_2^{2+} and AmO_2^{2+} since the other three are not really measured in the experiment.[86]

Bibliography

[1] C. de Sahb, L. A. Watson, J. Nadas, and B. P. Hay. "Design Criteria for Polyazine Extractants To Separate AnIII from LnIII". In: *Inorganic chemistry* 52.18 (2013), pp. 10632–10642.

[2] M. Salvatores and G. Palmiotti. "Radioactive waste partitioning and transmutation within advanced fuel cycles: Achievements and challenges". In: *Progress in Particle and Nuclear Physics* 66.1 (2011), pp. 144 –166.

[3] P. Wilson. *The Nuclear Fuel Cycle: From Ore to Wastes*. Oxford science publications. Oxford University Press, 1996.

[4] E. Horwitz and W. Schulz. "The Truex Process: A Vital Tool for Disposal of U.S. Defense Nuclear Waste". In: *New Separation Chemistry Techniques for Radioactive Waste and Other Specific Applications*. Ed. by M. Cecille, M. Casarci, and L. Pietrelli. Springer Netherlands, 1991, pp. 21–29.

[5] O Courson, M Lebrun, R Malmbeck, G Pagliosa, K Romer, B Satmark, and J. Glatz. "Partitioning of minor actinides from HLLW using the DIAMEX process. Part 1 - Demonstration of extraction performances and hydraulic behaviour of the solvent in a continuous process". In: *RADIOCHIMICA ACTA* 88.12 (2000), 857–863.

[6] R Malmbeck, O Courson, G Pagliosa, K Romer, B Satmark, J. Glatz, and P Baron. "Partitioning of minor actinides from HLLW using the DI-

AMEX process. Part 2 - "Hot" continuous counter-current experiment". In: *RADIOCHIMICA ACTA* 88.12 (2000), 865–871.

[7] G. Benay, R. Schurhammer, J. Desaphy, and G. Wipff. "Substituent effects on BTP's basicity and complexation properties with LnIII lanthanide ions". In: *New J. Chem.* 35 (1 2011), pp. 184–189.

[8] G. Benay, R. Schurhammer, and G. Wipff. "BTP-based ligands and their complexes with Eu3+ at "oil"/water interfaces. A molecular dynamics study". In: *Phys. Chem. Chem. Phys.* 12 (36 2010), pp. 11089–11102.

[9] A. Bhattacharyya, T. K. Ghanty, P. K. Mohapatra, and V. K. Manchanda. "Selective Americium(III) Complexation by Dithiophosphinates: A Density Functional Theoretical Validation for Covalent Interactions Responsible for Unusual Separation Behavior from Trivalent Lanthanides". In: *Inorganic Chemistry* 50.9 (2011), pp. 3913–3921.

[10] M. A. Denecke, A. Rossberg, P. J. Panak, M. Weigl, B. Schimmelpfennig, and A. Geist. "Characterization and Comparison of Cm(III) and Eu(III) Complexed with 2,6-Di(5,6-dipropyl-1,2,4-triazin-3-yl)pyridine Using EXAFS, TRFLS, and Quantum-Chemical Methods". In: *Inorganic Chemistry* 44.23 (2005), pp. 8418–8425.

[11] M. G. Drew, D. Guillaneux, M. J. Hudson, P. B. Iveson, M. L. Russell, and C. Madic. "Lanthanide(III) complexes of a highly efficient actinide(III) extracting agent 2,6-bis(5,6-dipropyl-1,2,4-triazin-3-yl)pyridine". In: *Inorganic Chemistry Communications* 4.1 (2001), pp. 12 –15.

[12] M. R. S. Foreman, M. J. Hudson, M. G. B. Drew, C. Hill, and C. Madic. "Complexes formed between the quadridentate, heterocyclic molecules 6,6[prime or minute]-bis-(5,6-dialkyl-1,2,4-triazin-3-yl)-2,2[prime or minute]-bipyridine (BTBP) and lanthanides(iii): implications for the partitioning of actinides(iii) and lanthanides(iii)". In: *Dalton Trans.* (13 2006), pp. 1645–1653.

[13] A. J. Gaunt, S. D. Reilly, A. E. Enriquez, B. L. Scott, J. A. Ibers, P. Sekar, K. I. M. Ingram, N. Kaltsoyannis, and M. P. Neu. "Experimental and Theoretical Comparison of Actinide and Lanthanide Bonding in M[N(EPR2)2]3 Complexes (M = U, Pu, La, Ce; E = S, Se, Te; R = Ph, iPr, H)". In: *Inorganic Chemistry* 47.1 (2008), pp. 29–41.

[14] A. J. Gaunt, B. L. Scott, and M. P. Neu. "Homoleptic uranium(iii) imidodiphosphinochalcogenides including the first structurally characterised molecular trivalent actinide-Se bond". In: *Chem. Commun.* (25 2005), pp. 3215–3217.

[15] A. J. Gaunt, B. L. Scott, and M. P. Neu. "A Molecular ActinideTellurium Bond and Comparison of Bonding in [MIIIN(TePiPr2)23] (M=U, La)". In: *Angewandte Chemie International Edition* 45.10 (2006), pp. 1638–1641.

[16] D. Girnt, P. W. Roesky, A. Geist, C. M. Ruff, P. J. Panak, and M. A. Denecke. "6-(3,5-Dimethyl-1H-pyrazol-1-yl)-2,2-bipyridine as Ligand for Actinide(III)/Lanthanide(III) Separation". In: *Inorganic Chemistry* 49.20 (2010), pp. 9627–9635.

[17] K. I. M. Ingram, M. J. Tassell, A. J. Gaunt, and N. Kaltsoyannis. "Covalency in the f ElementChalcogen Bond. Computational Studies of M[N(EPR2)2]3 (M = La, Ce, Pr, Pm, Eu, U, Np, Pu, Am, Cm; E = O, S, Se, Te; R = H, iPr, Ph)". In: *Inorganic Chemistry* 47.17 (2008), pp. 7824–7833.

[18] F. W. Lewis, L. M. Harwood, M. J. Hudson, M. G. B. Drew, G. Modolo, M. Sypula, J. F. Desreux, N. Bouslimani, and G. Vidick. "Interaction of 6,6[prime or minute][prime or minute]-bis(5,5,8,8-tetramethyl-5,6,7,8-tetrahydro-1,2,4-benzotriazin-3-yl)-2,2[prime or minute]:6[prime or minute],2[prime or minute][prime or minute]-terpyridine (CyMe4-BTTP) with some trivalent ions such as lanthanide(iii) ions and americium(iii)". In: *Dalton Trans.* 39 (21 2010), pp. 5172–5182.

[19] D. Magnusson, B. Christiansen, J.-P. Glatz, R. Malmbeck, G Modolo, D. Serrano-Purroy, and C Sorel. "Towards an optimized flow-sheet for a SANEX demonstration process using centrifugal contactors". In: *Radiochimica Acta International journal for chemical aspects of nuclear science and technology* 97.3 (2009), pp. 155–159.

[20] T. W. Hayton. "Recent developments in actinide-ligand multiple bonding". In: *Chem. Commun.* 49 (29 2013), pp. 2956–2973.

[21] Z. Kolarik, U. Müllich, and F. Gassner. "Selective extraction of Am (III) over Eu (III) by 2, 6-ditriazolyl-and 2, 6-ditriazinylpyridines 1". In: *Solvent extraction and ion exchange* 17.1 (1999), pp. 23–32.

[22] Z. Kolarik, U. Mullich, and F. Gassner. "Extraction of Am (lll) and Eu (lll) nitrates by 2-6-di-(5, 6-dipropyl-1, 2, 4-triazin-3-yl) pyridines 1". In: *Solvent Extraction and Ion Exchange* 17.5 (1999), pp. 1155–1170.

[23] M. J. Hudson, C. E. Boucher, D. Braekers, J. F. Desreux, M. G. B. Drew, M. R. S. J. Foreman, L. M. Harwood, C. Hill, C. Madic, F. Marken, and T. G. A. Youngs. "New bis(triazinyl) pyridines for selective extraction of americium(iii)". In: *New J. Chem.* 30 (8 2006), pp. 1171–1183.

[24] A. Geist, C. Hill, G. Modolo, M. R. S. J. Foreman, M. Weigl, K. Gompper, and M. J. Hudson. "6, 6-Bis (5, 5, 8, 8-tetramethyl-5, 6, 7, 8-tetrahydro-benzo [1, 2, 4] triazin-3-yl)[2, 2] bipyridine, an Effective Extracting Agent for the Separation of Americium (III) and Curium (III) from the Lanthanides". In: *Solvent extraction and ion exchange* 24.4 (2006), pp. 463–483.

[25] T. Retegan, C. Ekberg, S. Englund, A. Fermvik, M. Foreman, and G. Skarnemark. "The behaviour of organic solvents containing C5-BTBP and CyMe4-BTBP at low irradiation doses". In: *Radiochimica Acta* 95.11 (2007), pp. 637–642.

[26] S. Trumm, A. Geist, P. J. Panak, and T. Fanghänel. "An improved hydrolytically-stable bis-triazinyl-pyridine (BTP) for selective actinide extraction". In: *Solvent Extraction and Ion Exchange* 29.2 (2011), pp. 213–229.

[27] F. W. Lewis, L. M. Harwood, M. J. Hudson, M. G. B. Drew, J. F. Desreux, G. Vidick, N. Bouslimani, G. Modolo, A. Wilden, M. Sypula, T.-H. Vu, and J.-P. Simonin. "Highly Efficient Separation of Actinides from Lanthanides by a Phenanthroline-Derived Bis-triazine Ligand". In: *Journal of the American Chemical Society* 133.33 (2011), pp. 13093–13102.

[28] I. Kirker and N. Kaltsoyannis. "Does covalency really increase across the 5f series? A comparison of molecular orbital, natural population, spin and electron density analyses of AnCp3 (An = Th-Cm; Cp = [small eta]5-C5H5)". In: *Dalton Trans.* 40.1 (2011), pp. 124–131.

[29] M. J. Tassell and N. Kaltsoyannis. "Covalency in AnCp4 (An = Th-Cm): a comparison of molecular orbital, natural population and atoms-in-molecules analyses". In: *Dalton Trans.* 39.29 (2010), pp. 6719–6725.

[30] H. Li, H. Feng, W. Sun, R. B. King, and H. F. Schaefer III. "Extreme Metal Carbonyl Back Bonding in Cyclopentadienylthorium Carbonyls Generates Bridging C2O2 Ligands by Carbonyl Coupling". In: *Inorganic chemistry* 52.12 (2013), pp. 6893–6904.

[31] V. Vallet, U. Wahlgren, and I. Grenthe. "Probing the nature of chemical bonding in uranyl (VI) complexes with quantum chemical methods". In: *The Journal of Physical Chemistry A* 116.50 (2012), pp. 12373–12380.

[32] D. D. Schnaars, A. J. Gaunt, T. W. Hayton, M. B. Jones, I. Kirker, N. Kaltsoyannis, I. May, S. D. Reilly, B. L. Scott, and G. Wu. "Bonding Trends Traversing the Tetravalent Actinide Series: Synthesis, Structural, and Computational Analysis of AnIV (Aracnac) 4 Complexes (An= Th,

U, Np, Pu; Aracnac= Ar NC (Ph) CHC (Ph) O; Ar= 3, 5-t Bu2C6H3)". In: *Inorganic chemistry* 51.15 (2012), pp. 8557–8566.

[33] A. C. Behrle, C. L. Barnes, N. Kaltsoyannis, and J. R. Walensky. "Systematic Investigation of Thorium (IV)–and Uranium (IV)–Ligand Bonding in Dithiophosphonate, Thioselenophosphinate, and Diselenophosphonate Complexes". In: *Inorganic chemistry* 52.18 (2013), pp. 10623–10631.

[34] M. B. Jones, A. J. Gaunt, J. C. Gordon, N. Kaltsoyannis, M. P. Neu, and B. L. Scott. "Uncovering f-element bonding differences and electronic structure in a series of 1: 3 and 1: 4 complexes with a diselenophosphinate ligand". In: *Chemical Science* 4.3 (2013), pp. 1189–1203.

[35] J. L. Brown, S. Fortier, G. Wu, N. Kaltsoyannis, and T. W. Hayton. "Synthesis and spectroscopic and computational characterization of the chalcogenido-substituted analogues of the uranyl ion,[OUE] 2+(E= S, Se)". In: *Journal of the American Chemical Society* 135.14 (2013), pp. 5352–5355.

[36] P. L. Arnold, J. H. Farnaby, R. C. White, N. Kaltsoyannis, M. G. Gardiner, and J. B. Love. "Switchable π-coordination and C–H metallation in small-cavity macrocyclic uranium and thorium complexes". In: *Chemical Science* 5.2 (2014), pp. 756–765.

[37] A. R. Mountain and N. Kaltsoyannis. "Do QTAIM metrics correlate with the strength of heavy element–ligand bonds?" In: *Dalton Transactions* 42.37 (2013), pp. 13477–13486.

[38] D. E. Smiles, G. Wu, N. Kaltsoyannis, and T. W. Hayton. "Thorium–ligand multiple bonds via reductive deprotection of a trityl group". In: *Chemical Science* 6.7 (2015), pp. 3891–3899.

[39] V. V. Zhurov, E. A. Zhurova, and A. A. Pinkerton. "Chemical Bonding in Cesium Uranyl Chloride Based on the Experimental Electron Density Distribution". In: *Inorganic chemistry* 50.13 (2011), pp. 6330–6333.

[40] V. V. Zhurov, E. A. Zhurova, A. I. Stash, and A. A. Pinkerton. "Characterization of bonding in cesium uranyl chloride: Topological analysis of the experimental charge density". In: *The Journal of Physical Chemistry A* 115.45 (2011), pp. 13016–13023.

[41] Q.-R. Huang, J. R. Kingham, and N. Kaltsoyannis. "The strength of actinide–element bonds from the quantum theory of atoms-in-molecules". In: *Dalton Transactions* 44.6 (2015), pp. 2554–2566.

[42] L. H. Thomas. "The calculation of atomic fields". In: *Mathematical Proceedings of the Cambridge Philosophical Society* 23 (05 Jan. 1927), pp. 542–548.

[43] E. Fermi. "Un metodo statistico per la determinazione di alcune priorieta dellatome". In: *Rend. Accad. Naz. Lincei* 6.602-607 (1927), p. 32.

[44] P. Hohenberg and W. Kohn. "Inhomogeneous Electron Gas". In: *Physical Review* 136 (1964), pp. 864–871.

[45] V. N. Staroverov, G. E. Scuseria, J. Tao, and J. P. Perdew. "Comparative assessment of a new nonempirical density functional: Molecules and hydrogen-bonded complexes". In: *The Journal of Chemical Physics* 119.23 (2003), pp. 12129–12137.

[46] G. I. Csonka, A. Ruzsinszky, J. Tao, and J. P. Perdew. "Energies of organic molecules and atoms in density functional theory". In: *International Journal of Quantum Chemistry* 101.5 (2005), pp. 506–511.

[47] J. P. Perdew, K. Burke, and M. Ernzerhof. "Generalized gradient approximation made simple". In: *Physical review letters* 77.18 (1996), p. 3865.

[48] J. Tao, J. P. Perdew, V. N. Staroverov, and G. E. Scuseria. "Climbing the Density Functional Ladder: Nonempirical Meta˘Generalized Gradient Approximation Designed for Molecules and Solids". In: *Phys. Rev. Lett.* 91 (14 2003), p. 146401.

[49] P. Stephens, F. Devlin, C. Chabalowski, and M. J. Frisch. "Ab initio calculation of vibrational absorption and circular dichroism spectra using density functional force fields". In: *The Journal of Physical Chemistry* 98.45 (1994), pp. 11623–11627.

[50] P. Pulay. "Convergence acceleration of iterative sequences. The case of SCF iteration". In: *Chemical Physics Letters* 73.2 (1980), pp. 393–398.

[51] G. B. Bacskay. "A quadratically convergent HartreeFock (QC-SCF) method. Application to closed shell systems". In: *Chemical Physics* 61.3 (1981), pp. 385–404.

[52] R. Seeger and J. A. Pople. "Self-consistent molecular orbital methods. XVIII. Constraints and stability in Hartree–Fock theory". In: *J. Chem. Phys.* 66.7 (Apr. 1977), pp. 3045–3050.

[53] R. Bauernschmitt and R. Ahlrichs. "Stability analysis for solutions of the closed shell Kohn–Sham equation". In: *J. Chem. Phys.* 104.22 (June 1996), pp. 9047–9052.

[54] H. Schlegel and J. McDouall. "Do You Have SCF Stability and Convergence Problems?" In: *Computational Advances in Organic Chemistry: Molecular Structure and Reactivity*. Ed. by C. gretir and I. Csizmadia. Vol. 330. NATO ASI Series. Springer Netherlands, 1991, pp. 167–185.

[55] M. J. Frisch, G. W. Trucks, H. B. Schlegel, G. E. Scuseria, M. A. Robb, J. R. Cheeseman, G. Scalmani, V. Barone, B. Mennucci, G. A. Petersson, H. Nakatsuji, M. Caricato, X. Li, H. P. Hratchian, A. F. Izmaylov, J. Bloino, G. Zheng, J. L. Sonnenberg, M. Hada, M. Ehara, K. Toyota, R. Fukuda, J. Hasegawa, M. Ishida, T. Nakajima, Y. Honda, O. Kitao, H. Nakai, T. Vreven, J. A. Montgomery Jr., J. E. Peralta, F. Ogliaro, M. Bearpark, J. J. Heyd, E. Brothers, K. N. Kudin, V. N. Staroverov, R. Kobayashi, J. Normand, K. Raghavachari, A. Rendell, J. C. Burant, S. S. Iyengar, J. Tomasi, M. Cossi, N. Rega, J. M. Millam, M. Klene, J. E. Knox, J. B. Cross, V. Bakken, C. Adamo, J. Jaramillo, R. Gomperts,

R. E. Stratmann, O. Yazyev, A. J. Austin, R. Cammi, C. Pomelli, J. W. Ochterski, R. L. Martin, K. Morokuma, V. G. Zakrzewski, G. A. Voth, P. Salvador, J. J. Dannenberg, S. Dapprich, A. D. Daniels, O. Farkas, J. B. Foresman, J. V. Ortiz, J. Cioslowski, and D. J. Fox. *Gaussian 09 Revision C.01*. Gaussian Inc., Wallingford CT 2009.

[56] *TURBOMOLE V6.2 2010, a development of University of Karlsruhe and Forschungszentrum Karlsruhe GmbH, 1989-2007, TURBOMOLE GmbH, since 2007; available from* `http://www.turbomole.com`.

[57] P. Császár and P. Pulay. "Geometry optimization by direct inversion in the iterative subspace". In: *Journal of Molecular Structure* 114 (1984), pp. 31–34.

[58] P. A. Dirac. "The quantum theory of the electron". In: *Proceedings of the Royal Society of London A: Mathematical, Physical and Engineering Sciences*. Vol. 117. 778. The Royal Society. 1928, pp. 610–624.

[59] P. A. Dirac. "The quantum theory of the electron. Part II". In: *Proceedings of the Royal Society of London A: Mathematical, Physical and Engineering Sciences*. Vol. 118. 779. The Royal Society. 1928, pp. 351–361.

[60] C. Chang, M Pelissier, and P. Durand. "Regular two-component Pauli-like effective Hamiltonians in Dirac theory". In: *Physica Scripta* 34.5 (1986), p. 394.

[61] E. van Lenthe, E.-J. Baerends, and J. G. Snijders. "Relativistic regular two-component Hamiltonians". In: *The Journal of chemical physics* 99.6 (1993), pp. 4597–4610.

[62] E. van Lenthe, E.-J. Baerends, and J. G. Snijders. "Relativistic total energy using regular approximations". In: *The Journal of chemical physics* 101.11 (1994), pp. 9783–9792.

[63] E Van Lenthe, J. Snijders, and E. Baerends. "The zero-order regular approximation for relativistic effects: The effect of spin–orbit coupling in closed shell molecules". In: *The Journal of chemical physics* 105.15 (1996), pp. 6505–6516.

[64] M. Douglas and N. M. Kroll. "Quantum electrodynamical corrections to the fine structure of helium". In: *Annals of Physics* 82.1 (1974), pp. 89–155.

[65] B. A. Hess. "Applicability of the no-pair equation with free-particle projection operators to atomic and molecular structure calculations". In: *Phys. Rev. A* 32.2 (Aug. 1985), pp. 756–763.

[66] B. A. Hess. "Relativistic electronic-structure calculations employing a two-component no-pair formalism with external-field projection operators". In: *Phys. Rev. A* 33.6 (June 1986), pp. 3742–3748.

[67] G. Jansen and B. A. Hess. "Revision of the Douglas-Kroll transformation". In: *Phys. Rev. A* 39.11 (June 1989), pp. 6016–6017.

[68] X. Cao, M. Dolg, and H. Stoll. "Valence basis sets for relativistic energy-consistent small-core actinide pseudopotentials". In: *J. Chem. Phys.* 118.2 (Jan. 2003), pp. 487–496.

[69] X. Cao and M. Dolg. "Segmented contraction scheme for small-core actinide pseudopotential basis sets". In: *Journal of Molecular Structure: THEOCHEM* 673.19 (Mar. 2004), pp. 203–209.

[70] T. H. Dunning. "Gaussian basis sets for use in correlated molecular calculations. I. The atoms boron through neon and hydrogen". In: *The Journal of Chemical Physics* 90.2 (1989), pp. 1007–1023.

[71] R. A. Kendall, T. H. Dunning, and R. J. Harrison. "Electron affinities of the firstrow atoms revisited. Systematic basis sets and wave functions". In: *The Journal of Chemical Physics* 96.9 (1992), pp. 6796–6806.

[72] D. E. Woon and T. H. Dunning. "Gaussian basis sets for use in correlated molecular calculations. III. The atoms aluminum through argon". In: *The Journal of Chemical Physics* 98.2 (1993), pp. 1358–1371.

[73] R. Bader. *Atoms in Molecules: A Quantum Theory (International Series of Monographs on Chemistry)*. Oxford University Press, USA, June 1994.

[74] C. F. Matta and R. J. Boyd. "An Introduction to the Quantum Theory of Atoms in Molecules". In: *The Quantum Theory of Atoms in Molecules*. John Wiley & Sons, Inc., 2007, pp. 1–34.

[75] D. Cremer and E. Kraka. "Chemical Bonds without Bonding Electron DensityDoes the Difference Electron-Density Analysis Suffice for a Description of the Chemical Bond?" In: *Angewandte Chemie International Edition in English* 23.8 (1984), pp. 627–628.

[76] G. te Velde, F. M. Bickelhaupt, E. J. Baerends, C. Fonseca Guerra, S. J. A. van Gisbergen, J. G. Snijders, and T. Ziegler. "Chemistry with ADF". In: *J. Comput. Chem.* 22.9 (July 2001), pp. 931–967.

[77] C. Fonseca Guerra, J. G. Snijders, G. te Velde, and E. J. Baerends. "Towards an order-N DFT method". In: *Theoretical Chemistry Accounts* 99.6 (1998), pp. 391–403–.

[78] *ADF2012*. SCM, Theoretical Chemistry, Vrije Universiteit, Amsterdam, The Netherlands. http://www.scm.com.

[79] D. A. Pantazis and F. Neese. "All-Electron Scalar Relativistic Basis Sets for the Lanthanides". In: *J. Chem. Theory Comput.* 5.9 (Aug. 2009), pp. 2229–2238.

[80] S. F. Boys and F. d. Bernardi. "The calculation of small molecular interactions by the differences of separate total energies. Some procedures with reduced errors". In: *Molecular Physics* 19.4 (1970), pp. 553–566.

[81] S. Simon, M. Duran, and J. Dannenberg. "How does basis set superposition error change the potential surfaces for hydrogen-bonded dimers?" In: *The Journal of chemical physics* 105.24 (1996), pp. 11024–11031.

[82] E Cances, B Mennucci, and J Tomasi. "A new integral equation formalism for the polarizable continuum model: Theoretical background and applications to isotropic and anisotropic dielectrics". In: *The Journal of chemical physics* 107.8 (1997), pp. 3032–3041.

[83] B. Mennucci, E Cances, and J Tomasi. "Evaluation of solvent effects in isotropic and anisotropic dielectrics and in ionic solutions with a unified integral equation method: theoretical bases, computational implementation, and numerical applications". In: *The Journal of Physical Chemistry B* 101.49 (1997), pp. 10506–10517.

[84] A. K. Rappé, C. J. Casewit, K. Colwell, W. Goddard Iii, and W. Skiff. "UFF, a full periodic table force field for molecular mechanics and molecular dynamics simulations". In: *Journal of the American chemical society* 114.25 (1992), pp. 10024–10035.

[85] T. A. Keith. *AIMAll (Version 13.05.06)*. TK Gristmill Software, Overland Park KS, USA. (aim.tkgristmill.com). 2013.

[86] J. Marcçalo and J. K. Gibson. "Gas-Phase Energetics of Actinide Oxides: An Assessment of Neutral and Cationic Monoxides and Dioxides from Thorium to Curium". In: *J. Phys. Chem. A* 113.45 (Sept. 2009), pp. 12599–12606.

[87] I. Infante, A. Kovacs, G. L. Macchia, A. R. M. Shahi, J. K. Gibson, and L. Gagliardi. "Ionization Energies for the Actinide Mono- and Dioxides Series, from Th to Cm: Theory versus Experiment". In: *J. Phys. Chem. A* 114.19 (Mar. 2010), pp. 6007–6015.

[88] C. C. L. Pereira, C. J. Marsden, J. Marcalo, and J. K. Gibson. "Actinide sulfides in the gas phase: experimental and theoretical studies of the thermochemistry of AnS (An = Ac, Th, Pa, U, Np, Pu, Am and Cm)". In: *Phys. Chem. Chem. Phys.* 13 (28 2011), pp. 12940–12958.

[89] Y. Takano, and K. N. Houk*. "Benchmarking the Conductor-like Polarizable Continuum Model (CPCM) for Aqueous Solvation Free Energies of Neutral and Ionic Organic Molecules". In: *Journal of Chemical Theory and Computation* 1.1 (2005). PMID: 26641117, pp. 70–77.

[90] K. H. Birjkumar, N. D. Bryan, and N. Kaltsoyannis. "Computational investigation of the speciation of uranyl gluconate complexes in aqueous solution". In: *Dalton Trans.* 40 (42 2011), pp. 11248–11257.

[91] K. H. Birjkumar, N. D. Bryan, and N. Kaltsoyannis. "Is gluconate a good model for isosaccharinate in uranyl(vi) chemistry? A DFT study". In: *Dalton Trans.* 41 (18 2012), pp. 5542–5552.

[92] E. Macerata, E. Mossini, S. Scaravaggi, M. Mariani, A. Mele, W. Panzeri, N. Boubals, L. Berthon, M.-C. Charbonnel, F. Sansone, A. Arduini, and A. Casnati. "Hydrophilic Clicked 2,6-Bis-triazolyl-pyridines Endowed with High Actinide Selectivity and Radiochemical Stability: Toward a Closed Nuclear Fuel Cycle". In: *Journal of the American Chemical Society* 138.23 (2016), pp. 7232–7235.